LATVIAN JOURNAL of PHYSICS and TECHNICAL SCIENCES

ISSN 0868 - 8257

2

(Vol. 61)

2024

CONTENTS

LATVIAN
JOURNAL
of
PHYSICS
and TECHNICAL
SCIENCES

LATVIJAS
FIZIKAS
un TEHNISKO
ZINĀTŅU
ŽURNĀLS

Published six times a year since February 1964
Iznāk sešas reizes gadā kopš 1964. gada februāra

2 (Vol. 61) • 2024

RĪGA

Language Editor: O. Ivanova
Computer Designer: I. Begicevs

INDEXED (PUBLISHED) IN

www.scopus.com
www.sciendo.com
EBSCO (Academic Search Complete, www.epnet.com), INSPEC (www.iee.org.com).
VINITI (www.viniti.ru), Begell House Inc/ (EDC, www.edata-center.com).

Issuers: Institute of Physical Energetics,
Institute of Solid State Physics, University of Latvia
Registration Certificate Number: 000700221

Editorial Contacts:
14 Dzerbenes Street, Riga, LV-1006
LATVIA
tel: +371 26245896
M: +371 29363105
leo@lza.lv

LATVIAN JOURNAL OF PHYSICS
AND TECHNICAL SCIENCES
2024, N 2

DOI: 10.2478/lpts-2024-0008

RED PERSISTENT LUMINESCENCE AND TRAP PROPERTIES OF Mg_2SiO_4: Mn^{2+}, M^{3+} ($M^{3+} = B^{3+}$; Al^{3+}; Ga^{3+}; In^{3+}) MATERIAL

G. Doke

Institute of Solid State Physics, University of Latvia,
8 Kengaraga Str., Riga, LV-1063, LATVIA
E-mail: guna.doke@cfi.lu.lv

Persistent luminescence (PersL), also called long-lasting phosphorescence or simply afterglow, is a luminescence characterised by the emission of radiation from a few seconds to several days after the excitation source has been switched off. Over the past two decades, research on PersL materials, both in fundamental and applied physics, has developed rapidly; however, the explanation for the physical processes that cause afterglow still needs to be clarified. Today, PersL materials are used mainly for luminescent paints, safety signs and decorations. At the same time, research into using such materials in medicine, information storage, anti-counterfeiting technology, etc., is underway.

Currently, information on the long persistent luminescence materials with emission in the blue and green spectral range is widely available. In contrast, the number of publications on the afterglow in the red and near-infrared spectral range is considerably lower.

Within the framework of this research, Mg_2SiO_4: Mn^{2+}; M^{3+} ($M^{3+} = B^{3+}$; Al^{3+}; Ga^{3+}; In^{3+}) materials were synthesised using solid state reaction synthesis. When excited with X-rays, the materials exhibited a broad Mn^{2+} PersL band with two maxima at approximately 625 nm and 730 nm. After cessation of irradiation, an afterglow of at least 6 hours could be observed.

The research focuses on the trap properties of the materials. It was concluded that at least three discrete trap levels with activation energies approximately between 0.4–1.6 eV were present in the samples. Additionally, co-doping with Al^{3+}; Ga^{3+}; In^{3+} ions improved PersL longevity of the Mg_2SiO_4: Mn^{2+} material.

Keywords: *Activation energy, Mn^{2+}, persistent luminescence, thermally stimulated luminescence, traps.*

1. INTRODUCTION

Persistent luminescence (PersL) is a type of luminescence that involves the emission of radiation even after the irradiation source has been turned off. This delayed emission occurs due to the trapping of charge carriers by point defects in crystals, which function as trapping sites. The charge carriers are gradually released and then recombine at luminescence centres. However, the mechanism behind PersL is still not fully comprehended [1]–[3].

PersL materials are generally utilised for low-tech purposes like luminescent paints, safety signs, and decorative items. However, there are ongoing research and development efforts to explore their potential in fields like medicine, military technology, and anti-counterfeiting [4]–[6]. While most well-developed PersL materials emit light in the visible part of the spectrum, particularly green, there is relatively less research on materials with emission bands in the red region. The most prominent red light-emitting PersL materials are Y_2O_2S: Eu^{3+}, Mg^{2+}, Ti^{4+} [7], $Ca_{1-x}Sr_xS$: Eu^{2+} [8] and others [9]–[11]. However, using rare-earth ions significantly increases the cost of material production. As an alternative, Mn^{2+} is commonly suggested. As a transition metal, Mn^{2+} is strongly affected by the crystal field surrounding it and, when introduced into a properly chosen matrix, can provide red luminescence.

Mg_2SiO_4 phosphors have garnered considerable scientific interest since the 1990s; however, most publications have focused on photoluminescence instead of PersL. The afterglow properties of Mn^{2+} doped Mg_2SiO_4 have been discussed in the context of optical properties of Mg_2SiO_4: Mn^{2+}, Dy^{3+} [12] and Mn-doped Mg_2SiO_4-Mg_2GeO_4 solid solution [13].

Co-doping is a commonly used method for developing exceptional PersL phosphors, where co-doped ions can function as electron "pumps" for enhanced trapping efficiency [14] or as trapping centres [15]. Commonly an aliovalent substitution is used since if ions with different charges substitute the cations or anions in the host, additional defects will be produced to ensure charge compensation [16]–[18]. Therefore, in this publication, samples of Mg_2SiO_4: 0.1 mol% Mn^{2+}; 0.5 mol% M^{3+} ($M^{3+} = B^{3+}$; Al^{3+}; Ga^{3+}; In^{3+}) were synthesised, and their PersL and trap properties were analysed.

2. EXPERIMENTAL

2.1. Synthesis

Mg_2SiO_4: 0.1 mol% Mn^{2+}; 0.5 mol% M^{3+} ($M^{3+} = B^{3+}$; Al^{3+}; Ga^{3+}; In^{3+}) samples were synthesised by a conventional solid-state synthesis method. During the synthesis, stoichiometric amounts of the following chemical compounds: $MgCO_3{\cdot}Mg(OH)_2{\cdot}xH_2O$ (99.996%, Alfa Aesar), where $x \approx 3$, SiO_2 (99.9999%, Alfa Aesar), MnO_2 (99.997%, Alfa Aesar), B_2O_3 (99.999%, Alfa Aesar), Al_2O_3 (99.999%, Alfa Aesar), Ga_2O_3 (99.999%, Alfa Aesar) and In_2O_3 (99.999%, Alfa Aesar) were weighted. The mixture was ground in a marble mortar, transferred into a corundum crucible, and annealed at 1450 °C for 2 h in an ambient atmosphere to obtain polycrystalline Mg_2SiO_4: Mn^{2+}, M^{3+} (M^{3+} =

B^{3+}; Al^{3+}; Ga^{3+}; In^{3+}) samples. A heating and cooling rate of 5 °C/min was applied. For heat treatment, a high-temperature furnace Carbolite HTF18 was used. In this paper, Mg_2SiO_4 materials will be denominated as MSO.

2.2. Characterisation

X-ray diffraction (XRD) patterns were measured by MiniFlex 600 RIGAKU X-ray diffractometer. The International Centre for Diffraction Data card for Mg_2SiO_4 (PDF 01-084-1402) was used as a reference.

PersL spectra, PersL decay profiles, and thermally stimulated luminescence (TSL) curves were measured using a Lexsyg research – Fully Automated TL/OSL Reader from Freiberg Instruments GmbH coupled with photomultiplier Hamamatsu R13456. X-ray tube VF-50 J/S (40 kV, 0.5 mA, W-anode) was used as an irradiation source. The system operated at a linear heating rate in the temperature range between room temperature and 400 °C. Isothermal PersL decay curves were recorded at 25 °C.

3. RESULTS AND DISCUSSION

3.1. Structure Analysis

The structure of MSO samples was characterised by XRD measurements. The obtained XRD patterns and standard cards PDF 01-084-1402 corresponding to orthorhombic Mg_2SiO_4 are shown in Fig. 1. The peak positions of the samples matched well with the PDF patterns, and no additional phases could be identified, confirming the formation of single phase Mg_2SiO_4 material and complete incorporation of dopants into host matrix.

The crystal structure of the Mg_2SiO_4 compound is shown in Fig. 2. There are three types of polyhedrons present in the structure: [SiO_4] tetrahedron and two slightly dissimilar [MgO_6] octahedrons, one of which is more distorted. The two different cation octahedra form alternating chains parallel to the c-axis [19].

The ionic radii of the present cations at four-fold and six-fold coordination are given in Table 1. According to the ionic radii and the valence, Mn^{2+} ions most likely occupy both Mg^{2+} sites. As for co-dopants, B^{3+}, Al^{3+}, Ga^{3+}, and In^{3+}, it is difficult to draw a firm conclusion since not only radii difference has to be considered but also varied valence. Nevertheless, it can be speculated that Ga^{3+} and In^{3+} ions substitute Mg^{2+}, while the positions of B^{3+} and Al^{3+} cannot be clearly determined.

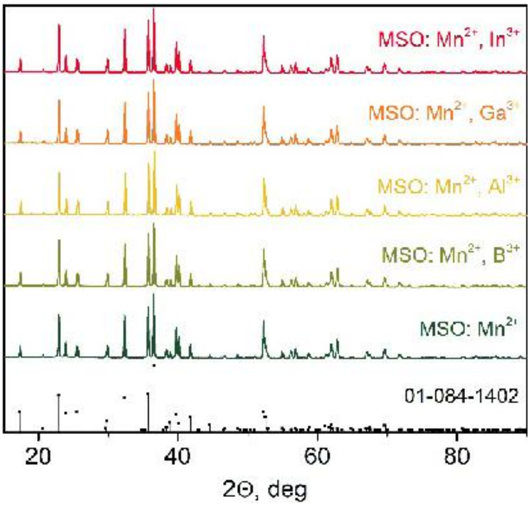

Fig. 1. XRD patterns of MSO samples and theoretical position of Mg_2SiO_4 (PDF 01-084-1402).

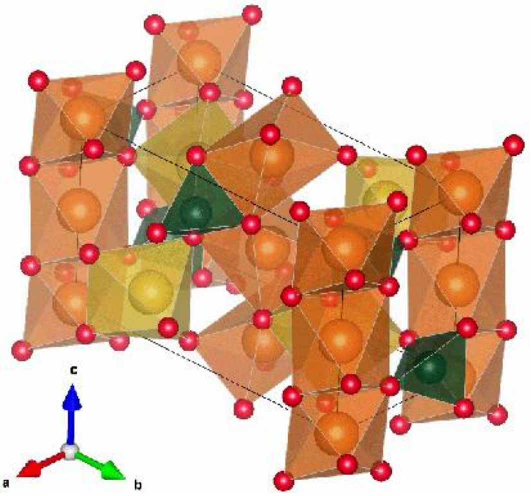

Fig. 2. Crystal structure of Mg_2SiO_4 material. Green tetrahedrons: $[SiO_4]$; orange and yellow octahedrons: $[MgO_6]$ [13].

Table 1. Ionic Radii of Mg^{2+}, Si^{4+}, Mn^{2+}, B^{3+}, Al^{3+}, Ga^{3+} and In^{3+} at Four-Fold and Six-Fold Coordination Given in Angstroms [20]

CN	Mg^{2+}	Si^{4+}	Mn^{2+}	B^{3+}	Al^{3+}	Ga^{3+}	In^{3+}
4	0.57		0.66	0.11	0.30	0.47	0.62
6		0.40	0.83	0.27	0.535	0.62	0.80

3.2. Persistent Luminescence Properties

If MGO samples are excited with X-rays, a broad luminescence band between 550–850 nm with two maximums at approximately 625 nm and 730 nm appears. When the excitation source is switched off, the afterglow with the same band characteristics continues for several hours. Figure 3a shows PersL spectra of MGO samples immediately after the cessation of irradiation. The luminescence signal is ascribed to the sum of two bands emerging from the Mn^{2+} optical transition from the excited state $^4T_1(^4G)$ to the ground state $^6A_1(^6S)$ when Mn^{2+} ions are in two non-equivalent Mg^{2+} positions in the host. Comparable results have been previously reported [12], [13].

Figure 3b shows the PersL decay curves of the MSO samples after irradiation with X-rays for 2 min depicted in a double-logarithmic plot. A strong afterglow signal can be detected for at least 6 h for all samples. It was concluded that, at least during measuring time, co-doping with B^{3+} did not improve the PersL properties of MSO: Mn^{2+} material. On the other hand, co-doping with Al^{3+}, Ga^{3+}, and In^{3+} increases the decay time of the PersL. Interestingly, a singly Mn^{2+} doped sample can be characterised by the highest initial intensity; however, out of all samples, it has the steepest decline in intensity, and after the first few minutes of removal of X-rays, PersL intensity of Al^{3+}, Ga^{3+}, and In^{3+} co-doped samples surpassed that of the MSO: Mn^{2+}.

PersL decay generally follows a power law: $I \sim t^{-n}$ which, in a double-logarithmic scale, appears as a straight line with a slope of $-n$. It has been shown that if the n value is close to 1, the mechanism of PersL can be dominated by athermal tunnelling from the trapping site to a random distribution of recombination centres [21], [22]. A dashed line in Fig. 3b represents a slope of -1. All decay profiles fall close to that, especially in the later stages of the PersL decay ($t > 1\,h$); thus, it is reasonable to assume that tunnelling plays a significant role in the mechanism of PersL in MSO samples.

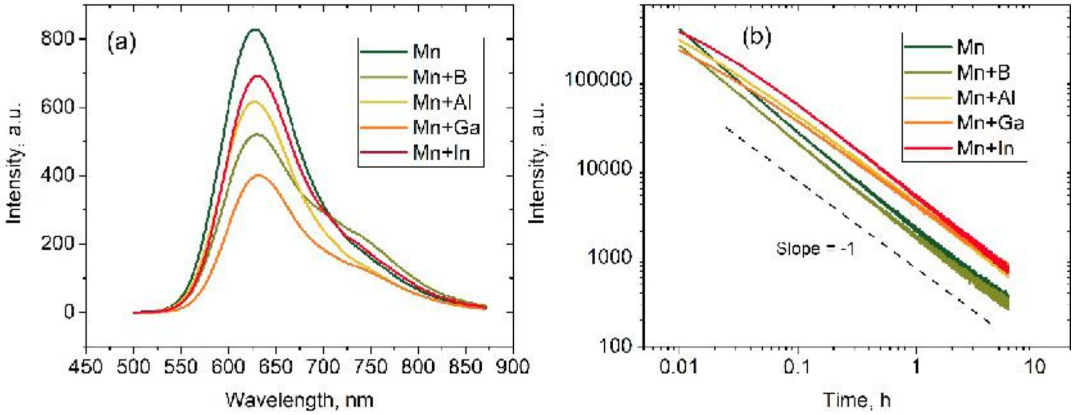

Fig. 3. (a) PersL spectra immediately after the cessation of excitation and (b) the afterglow decay curves of the MSO samples after irradiation with X-rays for 2 min, double-logarithmic plot.

3.3. Thermally Stimulated Luminescence and Trap Analysis

To analyse the trap properties of the MSO materials, thermally stimulated luminescence (TSL) glow curves after irradiation with X-rays were measured. The measurements were carried out by increasing temperature from room temperature up to 400 ºC with a heating rate of 1 ºC/s. The obtained TSL glow curves are presented in Fig. 4.

TSL is commonly acknowledged as one of the most efficient techniques for studying trap properties of PersL materials. The fundamental principles of the production of TSL are the same as those of PersL. Namely, some charge carriers are trapped by traps after irradiation but can be released via thermal detrapping if sufficient energy is accumulated. In the case of room temperature PersL, a signal with decaying intensity is observed. At the case of TSL, the material is typically heated with a constant heating rate. The emission signal usually increases and decreases throughout all measuring processes, with increases corresponding to the traps with a specific trap depth E_a, also called activation energy. In the end, a glow curve consisting of one or more glow peaks as $I = f(T)$ is obtained. A basic TSL glow curve may be used for the primary analysis of the trap properties. The position and intensity of each peak correspond to the trap depth and filled trap density, respectively. On the other hand, the number of glow peaks represents the number of different traps in the material [23].

In the case of the MSO samples, multiple glow peaks appear throughout all measured temperature region. For all samples, three principal glow peaks P1, P2, and P3 were noted with the only exception for Ga^{3+}

co-doped sample where P3 could not be ascribed to a specific peak since the TSL signal appears as a plateau throughout a broad temperature region; thus, P3 was divided into P3.1 (T_{max} = 240 ºC) and P3.2 (T_{max} = 340 ºC). For all samples, the most prominent peak is P2 with T_{max} around 130–180 ºC; precise values of T_{max} for all peaks are given in Table 2. This temperature range can be perceived as relatively high, and room temperature thermal detrapping probably is more dependent on P1 corresponding traps.

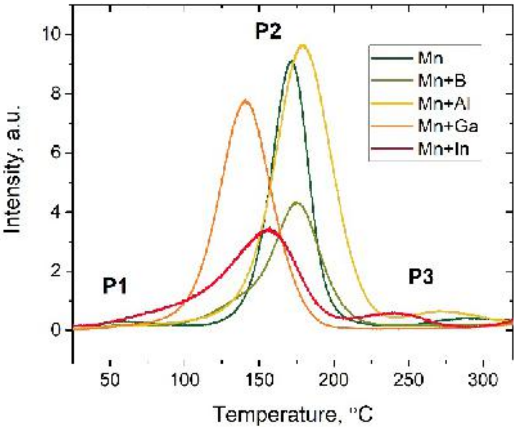

Fig. 4. TSL curves of MSO samples after irradiation with X-rays for 2 min. The heating rate applied: 1 °C/s.

For an in-depth trap analysis, a heating rate method, called Hoogenstraaten's method [24], [25], was applied. This technique evaluates the shift of the glow peak position depending on the heating rate. It is widely used to estimate the trap depth values. This method is based on analysing the set of TSL measurements for the same sample. For each measurement, the sample is irradiated with the same source for the same time, then TSL is measured using varied hating rates. Corresponding TSL glow curves of MSO samples are depicted in Fig. 5a–e, applied heating rates β = 0.25; 0.5; 1.0; 2.0; 4.0 *°C/s*. From each glow curve T_{max} – the temperature at the peak maximum intensity is noted. The relationship between heating rate β, glow peak position represented by T_{max} and trap depth E_a can be expressed by Eq. (1). Here, k_B is the Boltzmann constant and s is frequency factor – a temperature independent constant with a value in the order of the lattice vibration frequency, $10^{12} – 10^{14}$ s^{-1}.

$$\frac{\beta E_a}{k_B T_{max}^2} = s \cdot exp\left(\frac{E_a}{k_B T_{max}}\right). \qquad (1)$$

From Eq. (1), if $ln\left(\frac{T_{max}^2}{\beta}\right)$ is plotted as a function of $\left(\frac{1}{k_B T_{max}}\right)$, a straight line with slope E_a should be obtained. Accordingly, the heating rate plots for all samples were obtained (Fig. 5f–j). Evaluated E_a values are given in Table 2. From here, several observations can be made. Firstly, there is a strong correlation between the initial intensity of PersL and the depth of the P1, an expected result since trap depths around 0.4–0.6 eV can be considered shallow and will effectively empty via thermal detrapping at the initial stages of PersL. On the other hand, P2 values fluctuate around 0.9 eV, this value can be perceived as somewhat deep, and effective thermal detrapping at room temperature would not be expected. P3 falls into the category of deep traps with an average trap depth around 1.1–1.6 eV and should not take part in the room temperature PersL process.

Figure 5k–o shows the results of the TSL fading experiment where TSL glow curves were measured after different delay time cessation of irradiation with the X-rays. For all MSO samples, shallow traps are emptied after the first hour, and the relative intensity of the P2 has also slightly decreased. At this point, the most likely origin of the PersL is athermal tunnelling, a conclusion is supported by PersL decay curves shown in Fig. 3b.

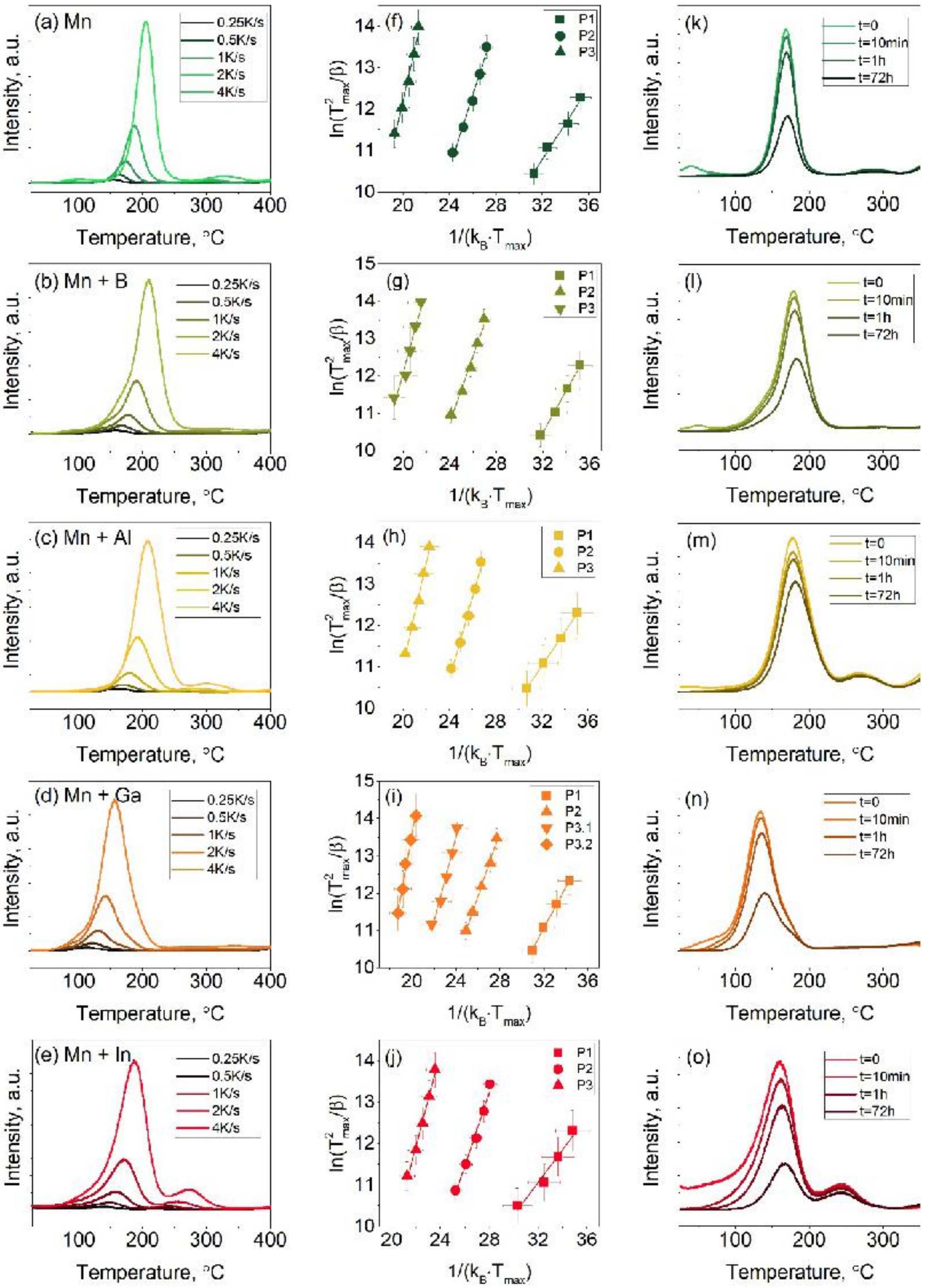

Fig. 5. TSL glow curves of MSO samples heated at different rates after irradiation with X-rays (a–e) and heating rate plots of the same samples (f–j). The glow peaks have been labelled as P1 to P3 from the lowest to the highest values. Fading of TSL glow curves of the same samples was measured after different delay times (k; l; m; n; o).

Table 2. Estimated Trap Depths E_a Derived from the Heating Rate Plots of the Corresponding TSL Peak and their T_{max} Value with Heating Rate 1 ºC/s.

Sample	Glow peak	T_{max}, °C	E_a, eV
MSO: Mn^{2+}	P1	40	0.44 ± 0.04
	P2	170	0.87 ± 0.06
	P3	284	1.24 ± 0.09
MSO: Mn^{2+}; B^{3+}	P1	48	0.56 ± 0.02
	P2	178	0.89 ± 0.07
	P3	290	1.14 ± 0.14
MSO: Mn^{2+}; Al^{3+}	P1	41	0.41 ± 0.03
	P2	178	0.99 ± 0.06
	P3	269	1.24 ± 0.06
MSO: Mn^{2+}; Ga^{3+}	P1	60	0.55 ± 0.01
	P2	133	0.92 ± 0.09
	P3.1	240	1.12 ± 0.09
	P3.2	340	1.60 ± 0.12
MSO: Mn^{2+}; In^{3+}	P1	55	0.39 ± 0.06
	P2	160	0.89 ± 0.07
	P3	243	1.13 ± 0.06

4. CONCLUSIONS

In conclusion, Mg_2SiO_4 material doped with 0.1 mol% Mn^{2+} and co-doped with 0.5 mol% B^{3+} or Al^{3+} or Ga^{3+} or In^{3+} was successfully synthesized by a solid-state reaction method.

A strong red Mn^{2+} luminescence and afterglow with two maximums at around 625 nm and 730 nm can be observed when excited with X-rays for at least six hours. Furthermore, adding Al^{3+}, Ga^{3+}, or In^{3+} improves PersL intensity at later stages of the PersL process.

TSL analysis revealed that there were at least three different charge carrier traps in each sample with average activation energies varying from 0.4 eV to 1.2 eV, and the first two of these traps played a role in the room temperature PersL mechanism, which likely included not only thermal detrapping but also athermal tunnelling of charge carriers.

ACKNOWLEDGEMENTS

The Institute of Solid State Physics, University of Latvia, as the Center of Excellence has received funding from the European Union’s Horizon 2020 Framework Programme H2020-WIDESPREAD-01-2016-2017-TeamingPhase2 under grant agreement No. 739508, project CAMART².

REFERENCES

1. Vitola, V., Millers, D., Bite, I., Smits, K., & Spustaka, A. (2019). Recent Progress in Understanding the Persistent Luminescence in $SrAl_2O_4$: Eu,Dy. *Materials Science and Technology (United Kingdom)*, *35* (14), 1661–1677. DOI:10.1080/02670836.2019.1649802
2. Richard, C., & Viana, B. (2022). Persistent X-Ray-Activated Phosphors: Mechanisms and Applications. *Light: Science & Applications*, *11* (1), 123. DOI:10.1038/s41377-022-00808-6
3. Jain, A., Kumar, A., Dhoble, S. J., & Peshwe, D. R. (2016). Persistent Luminescence: An Insight. *Renewable and Sustainable Energy Reviews*, *65*, 135–153. DOI:10.1016/j.rser.2016.06.081
4. Li, Y., Gecevicius, M., & Qiu, J. (2016). Long Persistent Phosphors – From Fundamentals to Applications. *Chemical Society Reviews*, *45* (8), 2090–2136. DOI:10.1039/C5CS00582E
5. Poelman, D., Van der Heggen, D., Du, J., Cosaert, E., & Smet, P. F. (2020). Persistent Phosphors for the Future: Fit for the Right Application. *Journal of Applied Physics*, 128 (24), 240903. DOI:10.1063/5.0032972
6. Liang, Y., Liu, F., Chen, Y., Wang, X., Sun, K., & Pan, Z. (2017). Extending the Applications for Lanthanide Ions: Efficient Emitters in Short-Wave Infrared Persistent Luminescence. *Journal of Materials Chemistry C*, *5* (26), 6488–6492. DOI:10.1039/C7TC01436H
7. Wang, X., Zhang, Z., Tang, Z., & Lin, Y. (2003). Characterization and Properties of a Red and Orange Y2O2S-Based Long Afterglow Phosphor. *Materials Chemistry and Physics*, *80* (1), 1–5. DOI:10.1016/S0254-0584(02)00097-4
8. Gartia, R. K., & Chandrasekhar, N. (2016). Physical Basis of Persistent Luminescence: The Case of Europium Doped $Ca_{1-x}Sr_xS$. *Journal of Alloys and Compounds*, *683*, 157–163. DOI:10.1016/j.jallcom.2016.05.087
9. Zhuang, Y., Ueda, J., & Tanabe, S. (2014). Multi-Color Persistent Luminescence in Transparent Glass Ceramics Containing Spinel Nano-Crystals with Mn^{2+} Ions. *Applied Physics Letters*, *105* (19), 3–7. DOI:10.1063/1.4901749
10. Kong, J., Zheng, W., Liu, Y., Li, R., Ma, E., Zhu, H., & Chen, X. (2015). Persistent Luminescence from Eu^{3+} in SnO_2 Nanoparticles. *Nanoscale*, *7* (25), 11048–11054. DOI:10.1039/c5nr01961c
11. Pihlgren, L., Laihinen, T., Rodrigues, L. C. V., Carlson, S., Eskola, K. O., Kotlov, A. ... & Hölsä, J. (2014). On the Mechanism of Persistent Up-conversion Luminescence in the ZrO_2: Yb^{3+},Er^{3+} Nanomaterials. *Optical Materials*, *36* (10), 1698–1704. DOI:10.1016/j.optmat.2014.01.027
12. Lin, L., Yin, M., Shi, C., & Zhang, W. (2008). Luminescence Properties of a New Red Long-lasting Phosphor: Mg_2SiO_4: Dy^{3+}, Mn^{2+}. *Journal of Alloys and Compounds*, *455* (1–2), 327–330. DOI:10.1016/j.jallcom.2007.01.059
13. Doke, G., Krieke, G., Antuzevics, A., Sarakovskis, A., & Berzina, B. (2023). Optical Properties of Red-Emitting Long Afterglow Phosphor $Mg_2Si_{1-x}Ge_xO_4$: Mn^{2+}/Mn^{4+}. *Optical Materials*, *137*, 113500. DOI:10.1016/j.optmat.2023.113500
14. Jia, D., & Yen, W. M. (2003). Enhanced V_K^{3+} Center Afterglow in $MgAl_2O_4$ by Doping with Ce^{3+}. *Journal of Luminescence*, *101* (1–2), 115–121. DOI:10.1016/S0022-2313(02)00394-0
15. Vitola, V., Lahti, V., Bite, I., Spustaka, A., Millers, D., Lastusaari, M., ... & Smits, K. (2021). Low Temperature Afterglow from $SrAl_2O_4$: Eu, Dy, B Containing Glass. *Scripta Materialia*, *190*, 86–90. DOI:10.1016/j.scriptamat.2020.08.023
16. Zhou, D., Song, Z., Zhou, H., & Liu, Q. (2020). Enhanced Persistent Luminescence via Si^{4+} Co-doping in $Y_3Al_2Ga_3O_{12}$: Ce^{3+}, Yb^{3+}, B^{3+}. *Journal of Luminescence*, *222*, 117190. DOI:10.1016/j.jlumin.2020.117190

17. Noto, L. L., Pitale, S. S., Gusowki, M. A., Terblans, J. J., Ntwaeaborwa, O. M., & Swart, H. C. (2013). Afterglow Enhancement with In3+ Codoping in $CaTiO_3$: Pr^{3+} Red Phosphor. *Powder Technology*, *237* (3), 141–146. DOI:10.1016/j.powtec.2013.01.029
18. Doke, G., Kalnina, A., Cipa, J., Springis, M., & Sarakovskis, A. (2022). Optical Properties of Near Infrared Persistent Phosphor $CaZnGe_2O_6$: Cr^{3+}, M^{3+} (M^{3+} = B^{3+}; Al^{3+}; Ga^{3+}). *Solid State Communications*, *354*, 114894. DOI:10.1016/j.ssc.2022.114894
19. Awad, A., Koster Van Groos, A. F., & Guggenheim, S. (2000). Forsteritic Olivine: Effect of Crystallographic Direction on Dissolution Kinetics. *Geochimica et Cosmochimica Acta*, *64* (10), 1765–1772. DOI:10.1016/S0016-7037(99)00442-1
20. Shannon, R. D. (1976). Revised Effective Ionic Radii and Systematic Studies of Interatomic Distances in Halides and Chalcogenides. *Acta Crystallographica Section A*, *32* (5), 751–767. DOI:10.1107/S0567739476001551
21. Avouris, P., & Morgan, T. N. (1981). A Tunneling Model for the Decay of Luminescence in Inorganic Phosphors: The Case of Zn_2SiO_4: Mn. *The Journal of Chemical Physics*, *74* (8), 4347–4355. DOI:10.1063/1.441677
22. Doke, G., Antuzevics, A., Krieke, G., Kalnina, A., & Sarakovskis, A. (2022). Novel Broadband Near-Infrared Emitting Long Afterglow Phosphor $MgGeO_3$: Cr^{3+}. *Journal of Alloys and Compounds*, *918*, 165768. DOI:10.1016/j.jallcom.2022.165768
23. Bos, A. J. J. (2006). Theory of Thermoluminescence, *Radiation Measurements*, *41*, S45–S56. DOI:10.1016/j.radmeas.2007.01.003
24. Rasheedy, M. S. (2005). Method of Hoogenstraaten as a Tool for Obtaining the Trap Parameters of General-Order Thermoluminescence Glow Peaks. *Radiation Effects and Defects in Solids*, *160* (9), 383–390. DOI:10.1080/10420150500459999
25. Doke, G., Antuzevics, A., Krieke, G., Kalnina, A., Springis, M., & Sarakovskis, A. (2021). UV and X-Ray Excited Red Persistent Luminescence in Mn^{2+} Doped $MgGeO_3$ Material Synthesized in Air and Reducing Atmosphere. *Journal of Luminescence*, *234*, 117995. DOI:10.1016/j.jlumin.2021.117995

LATVIAN JOURNAL OF PHYSICS
AND TECHNICAL SCIENCES
2024, N 2

DOI: 10.2478/lpts-2024-0009

TOWARDS SCALABLE SYNTHESIS OF $TiSe_2$ AND VSe_2 THIN FILMS

K. Kadiwala*, E. Dipans, L. Dipane, E. Butanovs, B. Polyakov

Institute of Solid State Physics, University of Latvia,
8 Kengaraga Str., Riga LV-1063, LATVIA
*e-mail: kevon.kadiwala@cfi.lu.lv

Transition metal dichalcogenides (TMDs), specifically those involving V and Ti, possess fascinating material properties, making them interesting candidates for scientific studies. The existing growth methods of these materials are typically limited by scalability – either low yield or high cost. Here, we propose an alternative 2-step method valid for scalable production. In the first step, precursor films of Ti / V are deposited using magnetron sputtering, followed by the second step of selenization of these samples using elemental Se in a vacuum-sealed quartz ampoule for conversion to their respective diselenide material. Synthesized films are characterised using scanning electron microscope (SEM), energy dispersive X-ray spectroscopy (EDX), X-ray diffraction (XRD) and X-ray photoelectron (XPS). The method demonstrated here can be used to increase the active surface area of $TiSe_2$ and VSe_2 for their potential catalytic and HER applications using nanostructured substrates, while also providing an opportunity for scalable synthesis of films that can be extended to synthesize other TMDs as well.

Keywords: *Magnetron sputtering, thin films, titanium diselenide, transition metal dichalcogenides, vanadium diselenide.*

1. INTRODUCTION

Transition metal dichalcogenides (TMDs) exhibit many scientifically and technologically important properties; therefore, since the 20th century they are being studied with a lot more focus and interest [1]–[5]. Their adaptability and unique properties due to their anisotropy and compatibility with emerging technologies have positioned them at the forefront of research and innovation in the fields ranging from electronics and energy to quantum computing and biomedicine [1]–[6]. Among these TMD materials, titanium diselenide ($TiSe_2$) [7], [8] and vanadium diselenide (VSe_2) [9], [10] have attracted significant attention. Many recent studies [11], [13]–[19] have shown that $TiSe_2$ and VSe_2 materials have a charge density wave property. They are remarkable materials with a wide range of potential applications in areas such as thermoelectricity, energy storage, and nanoelectronics [4], [20]–[26]. VSe_2 and $TiSe_2$ materials are highly promising for catalysts and HER applications, as it has been reported before in multiple studies [27]–[32]. Overall, for these two TMDs, their charge density wave transition, outstanding thermoelectric properties, and catalytic potential make them versatile materials, which hold promises for various cutting-edge technologies [33], [34], [2], [15], [26], [35].

One of the main challenges in terms of application when it comes to TMD materials such as $TiSe_2$ or VSe_2 is their production on a larger scale than a few microns in controllable geometry. In general, when studies related to these materials are performed, these materials are obtained using mechanical or chemical exfoliation of bulk crystals [3], [5], [9]. When such an approach is used, it results in small flakes with inconsistent thickness, no repeatability, poor control over size and shape [3], [5], [21]. The other alternative to create large-area films of these materials is through molecular beam epitaxy (MBE) in an ultrahigh vacuum (UHV) environment [12], [18], [23], [36]. Although this method provides the best quality of the material, it is not a feasible approach for any application-oriented growth of these materials because it is an extremely slow and costly technique. It is advantageous to develop a more straightforward method for growth of such materials. In recent years, ambient-pressure chemical vapour deposition (CVD) has been successfully employed to produce thin layers of semiconducting transition metal dichalcogenides (TMDs), like MoS_2 and WSe_2 [37], [38]. However, the experimental synthesis of $TiSe_2$ through conventional CVD methods has proven to be challenging [17], where for VSe_2 the synthesis process has been shown with success in the synthesis of the material but with random growth of a few micron scale crystals with no continuity over a large area [39].

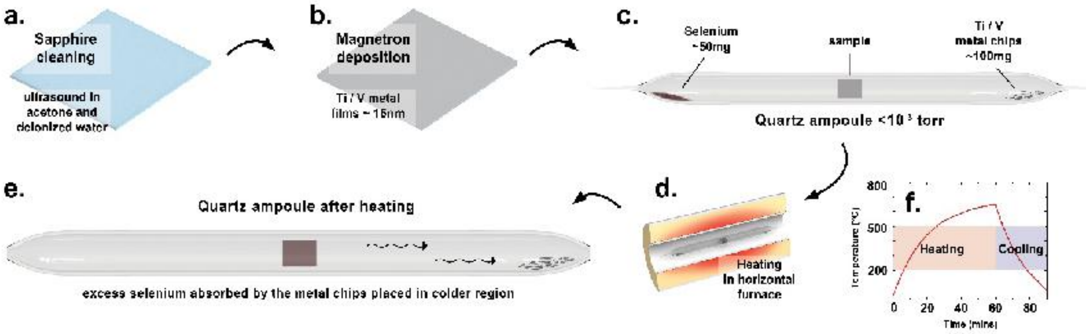

Fig. 1. Graphical illustration of the methodology used here to synthesize $TiSe_2$ and VSe_2 thin films starting from (a) substrate cleaning in acetone and DIW using ultrasound for 5 min each, followed by (b) deposition of Ti / V metal film using magnetron sputtering; (c) sample was placed in a quartz ampoule with Se powder and respective metal chips in the shown configuration; (d) ampoules were heated up using a horizontal furnace; (e) after heating the ampoule, no excess selenium vapour was found near edges of any ampoules; (f) heating cycle of an ampoule, shown with ramp rate of heating and cooling.

In this study, we present an alternative approach to growth of such materials but on a larger scale that has never been demonstrated before. The present study demonstrates a 2-step process for the synthesis of $TiSe_2$ and VSe_2. To start, deposition of metal precursor films is done using magnetron sputtering followed by annealing them in Se vapour atmosphere in a sealed quartz ampoule. Using magnetron sputtering for the deposition of precursor films allows us to deposit them on large surface areas, and we have used it to cover our centimetre scale substrates used here in this study. The same approach could also be used for non-flat surfaces (e.g., nanostructures) to increase their surface area and enhance their properties for their potential applications in catalysis, sensors etc.

2. EXPERIMENTAL DETAILS

To synthesize $TiSe_2$ and VSe_2 thin films, the methodology used was analogous. We approached the goal of synthesizing these materials in two steps: first, we deposited the precursor metal films using magnetron sputtering and then converted these films to their respective diselenide using sealed quartz ampoules with below atmospheric pressure (Fig. 1). Sacrificial precursor films of ~15nm Ti / V metal were deposited on 10x10 mm cut and cleaned sapphire (r-plane, Biotain Crystal Co.) by DC magnetron sputtering of metallic Ti / V targets in Ar atmosphere ($3 \cdot 10^{-3}$ torr, 30 sccm Ar, at 100 W DC power), which was followed by the process of making ampoules for these samples. For our experiments, the ampules were made from quartz tubes of 13 mm OD with wall thickness of 1 mm and length of 120 ± 10 mm, which were loaded with Ti / V metal covered sapphire substrates, Se powder (~50mg) and grinded Ti / V metal chips (~100mg) to absorb any residue of selenium near the edges of an ampoule with inside vacuum pressure being $<10^{-3}$ torr. Using a horizontal open-end tube reactor, these ampoules were heated up to 650 °C, 700 °C and 750 °C in an hour followed by rapid cooling of these ampoules to ambient temperature (Fig. 1f).

The synthesized films were studied using an optical microscope as well as under a scanning electron microscope (SEM-FIB Lyra, Tescan, 12kV) for their surface morphology. Using the same tool, elemental mapping was done by energy dispersive X-ray spectroscopy (EDX) at 10 keV, frame dwell time 1048 s (X-Max detector, SATW window) to study the distribution of elements across the films. The phase compositions of these samples were studied using X-ray diffraction (XRD, powder diffractometer Rigaku Miniflex 600) with monochromatic Cu Kα irradiation ($\lambda = 1.5406$ Å), and the spectra were analysed using PDXL2 software. The chemical composition of synthesized material was confirmed with X-ray photoelectron spectroscopy (XPS) measurements performed using an X-ray photoelectron spectrometer ESCALAB Xi (ThermoFisher). Al Kα X-ray tube with the energy of 1486 eV was used as an excitation source, the size of the analysed sample area was 650 μm x 100 μm and the angle between the analyser and the sample surface was 90°. Sample area of interest (2x2 mm) was sputter-cleaned for 30 seconds prior to the measurements with argon ion gun (monoatomic Ar^+ ions with 1000 eV energy). An electron gun was used to perform charge compensation. The base pressure during spectra acquisition was better than 10^{-5} Pa.

3. RESULTS AND DISCUSSION

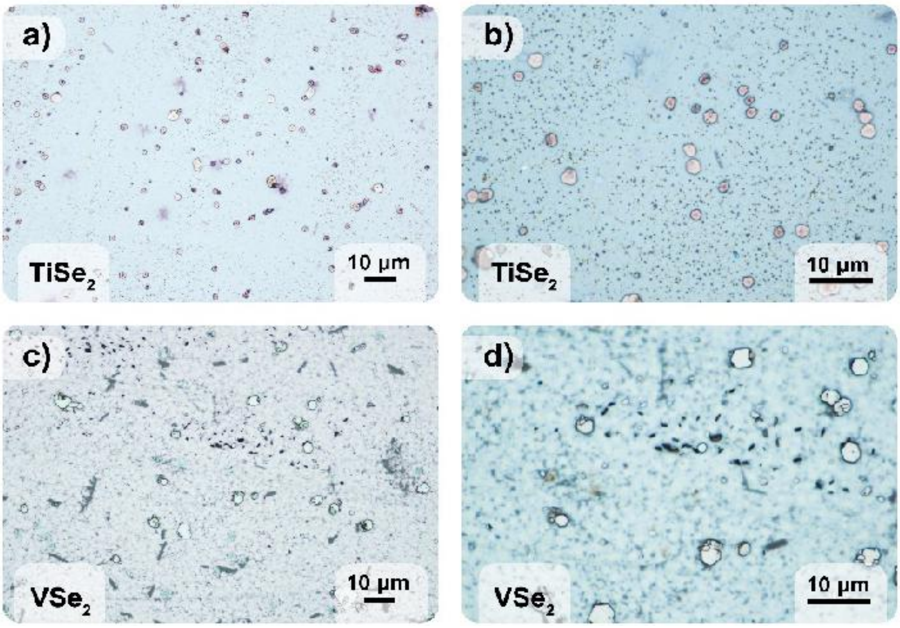

Fig. 2. Optical images of $TiSe_2$ (a, b) and VSe_2 (c, d) thin films converted at 700 °C with different magnifications, used to confirm the presence of surface crystals indicating a successful conversion of metal precursor films to their respective diselenide material.

From our experiments, 15 nm thickness of metal precursor showed continuous films of diselenide material after the selenization process, so the thickness was kept constant for all the samples involved in this study. During our experiments, initially when ampoules were made without their respective metal chips (Ti / V), some of the excess selenium vapour was noticed to have condensed near the edges of the samples where substrate touched ampoule walls, or in some cases, droplets of condensed Se were noticed on top of the synthesized material. To avoid any issues related to excess Se, extra metal chips were introduced after a few trials, which solved our issues and gave the best results. It is worth mentioning here that Ti / V film selenization attempt using elemental Se in quartz tube in gas flow at atmospheric pressure did not initiate the desired chemical reaction between Ti / V and Se in the same range of temperatures. After the process of selenization in ampoules, optical images were taken to observe the general surface area of the films (Fig. 2), which were also complimented by SEM images with a closer look at them. Figure 3 shows the SEM and XRD data obtained from TiSe2 films, and there is a visible difference in surface morphology between the samples synthesized at different temperatures. Comparing images (Fig. 3a, b, c), the sample converted at 650 °C shows coarse looking surface with quite many random comparatively big crystals of TiSe2 dispersed across the film. As we move to higher temperatures, 700 °C and 750 °C, we can see the films getting comparatively smoother. It becomes clearer when we observe images (Fig. 3d, e, f) with closer look of these films, the difference is strong in terms of average crystal sizes and the films underneath. TiSe2 converted at 650 °C seems to have big crystals growing >2µm in size measured from edge to edge, and as we go for higher temperature of 700 °C, this size becomes <2µm and it decreases even further down to <1µm for 750 °C film. Furthermore, when we look at the overall film under these surface crystals, it seems that the film converted at 650 °C has uneven thickness of the material making islands and growing big crystals on top, but as we increase the temperature towards 750 °C, these big crystals seem to have sublimated, and the film underneath has grown to have better consistency in thickness. To assess if any of these visible differences mentioned earlier from SEM images give any variations when measured with XRD, the retrieved patterns have been also put together for comparison in Fig. 3g. The obtained data were checked with ICDD #01-083-0980 PDF card to confirm the material composition which supported our findings, and then samples prepared at different variations were compared. No drastic variations in the peak positions or width of those peaks were found. Only minor changes in peak intensity were observed, which gave weak correlation to material sublimation at higher temperature leaving thinner films producing reduced intensity of the TiSe2 peaks. Similarly, SEM and XRD data were also obtained for our synthesized films of VSe2 as shown in Fig. 4. When comparing the film morphology for VSe2 films through SEM images, films look rather similar from a larger scale (Fig. 4 a, b, c) across all temperatures, but when observed on a smaller scale (Fig. 4 d, e, f), film synthesized at 650 °C stands out with many out-of-plane crystals with protruding nanocrystals to give the film a rough profile. At 700 °C and 750 °C, the films still have ~5 µm size surface crystals but the film itself no longer has these nanocrystals, giving the film a smoother profile comparatively. To confirm the material phase, measured XRD data were compared with ICDD #04-007-5442 PDF card, which supported successful synthesis of VSe2 thin films, while showing significant difference in XRD peak intensity for VSe2 thin films synthesized at 650 °C and 700 °C, where small peak intensity was measured for 650 °C indicating smaller crystallite size (Fig. 4g). No significant difference was found between 700 °C and 750 °C.

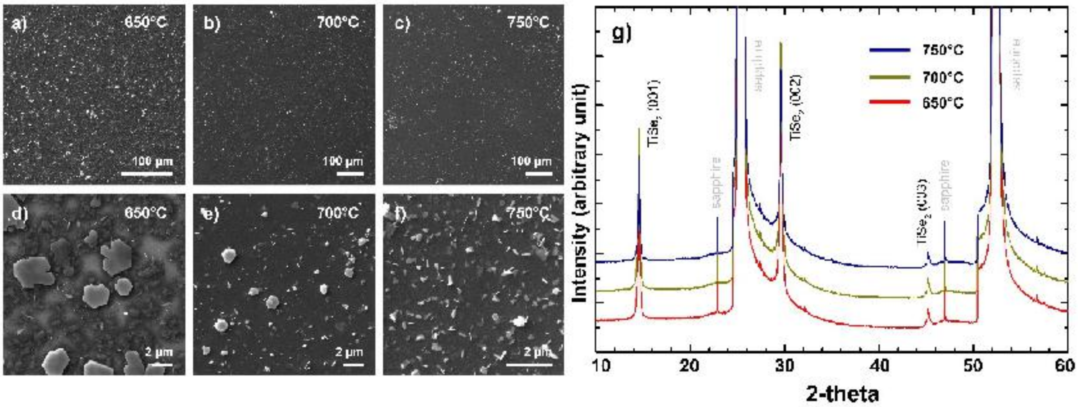

Fig. 3. SEM images of TiSe$_2$ thin films (a, d) converted at 650 °C (b, e), at 700 °C and (c, f) at 750 °C; (g) XRD spectra of TiSe$_2$ thin films synthesized using different temperatures.

To understand the distribution of elements across the films, EDX measurements were performed (Fig. 5) for films synthesized at 650 °C of both materials. As for $TiSe_2$ film, it seems to have higher intensity for both elements (Ti, Se) in the places of surface crystals, indicating concentrated material, which is to be expected from such top view analysis method as we observed these crystals to grow on top of the films making the material concentration higher in that place compared to rest of the film area where there were no crystals on top. Similar trend can be observed for the VSe_2 film as well, which has many surface crystals with comparatively smaller size. The atomic ratio of the elements was found to be roughly 1:2 for Ti / V and Se respectfully, which indicates proper stoichiometry among the crystalline planes.

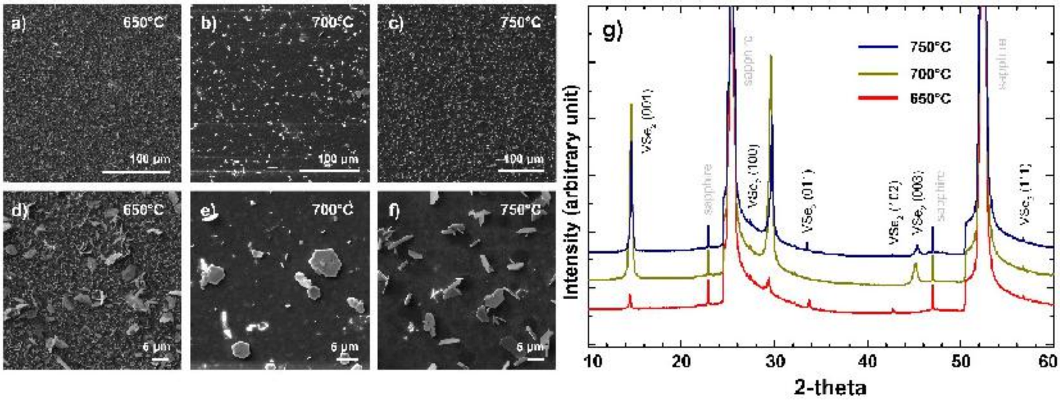

Fig. 4. SEM images of VSe_2 thin films (a, d) converted at 650 °C, (b, e), at 700 °C and (c, f) at 750 °C; (g) XRD spectra of synthesized VSe_2 thin films using different temperatures.

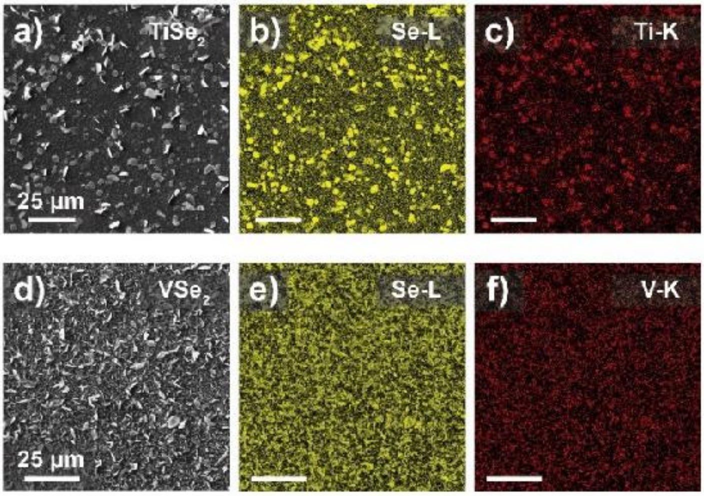

Fig. 5. EDX elemental mapping of (a–c) $TiSe_2$ and (d–f) VSe_2 films synthesized at 650 °C shows presence and distribution of their respective elements across the film.

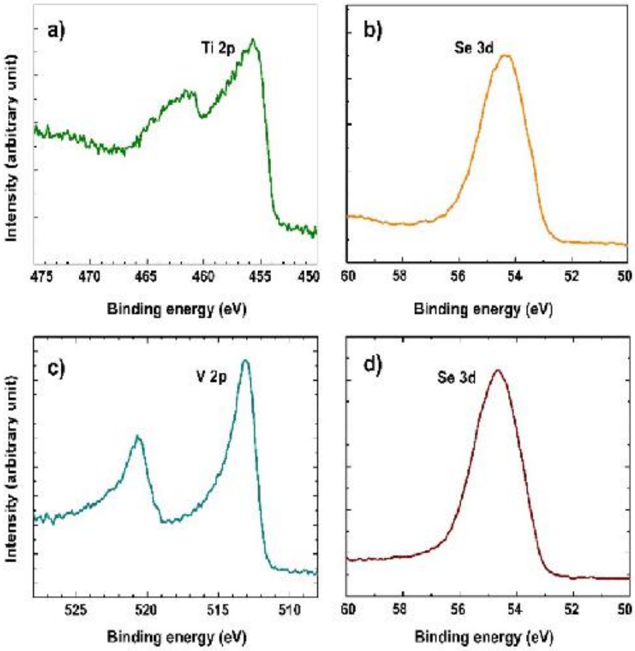

Fig. 6. High-resolution XPS spectra of the $TiSe_2$ synthesized at 650 °C film constituent elements for (a) Ti, and (b) Se and for VSe_2 film constituent elements (c) V and (d) Se.

Furthermore, XPS analysis was performed to verify the chemical states of the constituent elements in the films (Fig. 6a, b). High-resolution spectra were acquired and calibrated relative to the adventitious C 1s peak at 284.8 eV. Regarding the $TiSe_2$ films, Ti $2p_{3/2}$ peak was located at approximately 455.7 eV[34,40](spin-orbit splitting $\Delta_{3/2-1/2}$ = 5.7 eV), matching the chemical state in $TiSe_2$ compound. Each of the spin-orbit components has an additional shoulder towards the higher binding energy, which could be attributed to a possible formation of surface oxide due to the post-synthesis exposure to air[41,42]. The Se $3d_{5/2}$ peak was located at 54.2 eV (spin-orbit splitting $\Delta_{5/2-3/2}$ = 0.86 eV), which corresponded to the $TiSe_2$ compound [34] . Similarly, high-resolution V 2p and Se 3d peaks for VSe_2 were acquired (Fig. 6c, d). V $2p_{3/2}$ peak was located at 513.1 eV (spin-orbit splitting $\Delta_{3/2-1/2}$= 7.5 eV), while the Se $3d_{5/2}$ peak was measured to be at 54.5 eV, corresponding to chemical states in VSe_2[43].

4. CONCLUSIONS

Large-area synthesis of $TiSe_2$ and VSe_2 using a 2-step process was investigated, and to prove the quality of synthesized materials, films were analysed using SEM, EDX, XRD and XPS techniques. Investigation of surface morphology through SEM revealed presence of hexagonal crystals on top for both materials, which varied in size and numbers depending on their synthesis temperatures, but more importantly SEM revealed that both material films remained continuous after their selenization process regardless of the temperature used. XRD patterns, also supported by XPS analysis, confirmed the composition of our synthesized materials and suggested that both the surface crystals (visible in SEM images) and the films underneath contained our desired materials $TiSe_2$ and VSe_2.

According to XRD data, crystalline $TiSe_2$ can be successfully synthesized in the temperature range of 650 °C–750 °C, while VSe_2 – in the temperature range of 700 °C–750 °C. Using elemental mapping by EDX showed surface crystals contributing to higher material concentration in their local spots, while rest of the film area seemed to have identical levels of intensity confirming the continuity of the films further. With our demonstrated methodology, the materials can be deposited on nanostructured substrates (e.g., forest of nanowires), which would increase their surface area drastically and enhance applicability in catalytic and HER applications. This approach can be extended to synthesize other TMDs as well in large areas and create continuous films on various surfaces and even fabricate functional heterostructures.

ACKNOWLEDGEMENTS

The research has been funded by Latvian Council of Science project (No. lzp-2020/1-0261). The Institute of Solid State Physics, University of Latvia (Latvia), as the Centre of Excellence has received funding from the European Union's Horizon 2020 Framework Programme H2020-WIDESPREAD01-2016-2017-Teaming Phase2 under grant agreement no. 739508, project CAMART2.

REFERENCES

1. Duo, Y., Luo, G., Li, Z., Chen, Z., Li X., Jiang, Z., … & Yu, X.-F. (2021). Photothermal and Enhanced Photocatalytic Therapies Conduce to Synergistic Anticancer Phototherapy with Biodegradable Titanium Diselenide Nanosheets. *Small, 17* (40). DOI:10.1002/smll.202103239
2. Han, G. H., Duong, D. L., Keum, D. H., Yun, S. J., & Lee, Y. H. (2018). Van der Waals Metallic Transition Metal Dichalcogenides. *Chem Rev., 118* (13), 6297–6336. DOI:10.1021/acs.chemrev.7b00618
3. Goli, P., Khan, J., Wickramaratne, D., Lake, R.K., & Balandin, A.A. (2012). Charge Density Waves in Exfoliated Films of van der Waals Materials: Evolution of Raman Spectrum in TiSe2. *Nano Lett., 12* (11), 5941–5945. DOI:10.1021/nl303365x
4. Gu, Y., Katsura, Y., Yoshino, T., Takagi, H., & Taniguchi, K. (2015). Rechargeable Magnesium-Ion Battery Based on a TiSe2-Cathode with d-p Orbital Hybridized Electronic Structure. *Sci Rep., 5*. DOI:10.1038/srep12486
5. Zhang, D., Zhao, G., Li, P., Zhang, Y., Qiu, W., Shu, J. … & Sun. W. (2018). Readily Exfoliated TiSe2 Nanosheets for High-Performance Sodium Storage. *Chemistry – A European Journal, 24* (5), 1193–1197. DOI:10.1002/chem.201704661
6. Wen, L., Wu, Y., Wang, S., Shi, J., Zhang, Q., Zhao, B., … & Gao, Y. (2022). A Novel TiSe2 (De)Intercalation Type Anode for Aqueous Zinc-Based Energy Storage. *Nano Energy, 93*, 106896. DOI:10.1016/j.nanoen.2021.106896
7. Duong, D.L., Ryu, G., Hoyear, A., Lin, C., Burghard, M., & Kern, K. (2017). Raman Characterization of the Charge Density Wave Phase of 1T-TiSe2: From Bulk to Atomically Thin Layers. *ACS Nano,11* (1), 1034–1040. DOI:10.1021/acsnano.6b07737
8. Lian, C., Zhang, S.J., Hu, S.Q., Guan, M.X., & Meng, S. (2020). Ultrafast Charge

Ordering by Self-Amplified Exciton–Phonon Dynamics in TiSe2. *Nat Commun., 11* (1). DOI:10.1038/s41467-019-13672-7

9. Yu, W., Li, J., Herng, T.S., Wang, Z., Zhao, X., Chi, X., … & Loh, K. P. (2019). Chemically Exfoliated VSe2 Monolayers with Room-Temperature Ferromagnetism. *Advanced Materials, 31* (40). DOI:10.1002/adma.201903779
10. Li, F., Tu, K., & Chen, Z. (2014). Versatile Electronic Properties of VSe2 Bulk, Few-Layers, Monolayer, Nanoribbons, and Nanotubes: A Computational Exploration. *Journal of Physical Chemistry C, 118* (36), 21264–21274. doi:10.1021/jp507093t
11. Snow, C. S., Karpus, J. F., Cooper, S. L., Kidd, T. E., & Chiang, T. C. (2003). Quantum Melting of the Charge-Density-Wave State in 1T-TiSe2. *Phys Rev Lett., 91* (13), 1364021–1364024. DOI:10.1103/physrevlett.91.136402
12. Kolekar, S., Bonilla, M., Ma, Y., Diaz, H. C., & Batzill, M. (2018). Layer- and Substrate-Dependent Charge Density Wave Criticality in 1T-TiSe2. *2d Mater., 5* (1). DOI:10.1088/2053-1583/aa8e6f
13. Zhu, X., Cao, Y., Zhang, J., Plummer, E. W., & Guo, J. (2015). Classification of Charge Density Waves Based on their Nature. *Proc Natl Acad Sci U S A, 112* (8), 2367–2371. DOI:10.1073/pnas.1424791112
14. Rossnagel, K. (2011). On the Origin of Charge-Density Waves in Select Layered Transition-Metal Dichalcogenides. *Journal of Physics Condensed Matter, 23* (21). DOI:10.1088/0953-8984/23/21/213001
15. Feng, J., Biswas, D., Rajan, A., Watson, M. D., Mazzola, F., Clark, O. J., … & King, P. D. C. (2018). Electronic Structure and Enhanced Charge-Density Wave Order of Monolayer VSe2. *Nano Lett., 18* (7), 4493–4499. DOI:10.1021/acs.nanolett.8b01649
16. Sugawara, K., Nakata, Y., Shimizu, R., Han, P., Hitosugi, T., Sato, T., & Takahashi, T. (2016). Unconventional Charge-Density-Wave Transition in Monolayer 1T-TiSe2. *ACS Nano, 10* (1), 1341–1345. DOI:10.1021/acsnano.5b06727
17. Wang, H., Chen, Y., Duchamp, M., Zeng, Q., Wang, X., Tsang, S. H., … & Liu, Z. (2018). Large-Area Atomic Layers of the Charge-Density-Wave Conductor TiSe2. *Advanced Materials, 30* (8). DOI:10.1002/adma.201704382
18. Chen, P., Chan, Y.-H., Fang, X.-Y., Chou, M. Y., Mo, S.-K., Hussain, Z., … & Chiang, T.-C. (2015). Charge Density Wave Transition in Single-Layer Titanium Diselenide. *Nat Commun., 6*, 8943. DOI:10.1038/ncomms9943
19. Chen, P., Chan, Y.-H., Wong, M.-H., Fang, X.-Y., Chou, M. Y., Mo., S.-K., … & Chiang, T.-C. (2016). Dimensional Effects on the Charge Density Waves in Ultrathin Films of TiSe2. *Nano Lett., 16* (10), 6331–6336. DOI:10.1021/acs.nanolett.6b02710
20. Otto, M. R., Pöhls, J. H., René de Cotret L. P., Stern, M. J., Sutton, M., & Siwick, B. J. (2021). Mechanisms of Electron-Phonon Coupling Unraveled in Momentum and Time: The Case of Soft Phonons in TiSe 2. *Science Advances, 7* (20). http://advances.sciencemag.org/
21. Kumar, A., Sharma, R., Yadav, S., Swami, S. K., Kumari, R., Singh, V. N., … & Sinha, O. P. (2021). A Study on Chemical Exfoliation and Structural and Optical Properties of Two-Dimensional Layered Titanium Diselenide. *Dalton Transactions, 50* (11), 3894–3903. DOI:10.1039/d0dt03689g
22. Luo, H., Krizan, J. W., Seibel, E. M., Xie, W., Sahasrabudhe, G. S., Bergman, S. L., … & Cava, R. J. (2015). Cr-Doped TiSe2 – A Layered Dichalcogenide Spin Glass. *Chemistry of Materials, 27* (19), 6810–6817. DOI:10.1021/acs.chemmater.5b03091
23. Peng, J. P., Guan, J.-Q., Zhang, H.-M., Song, C.-L., Wang, L., He, K., … & Ma, Z.-C.. (2015). Molecular Beam Epitaxy Growth and Scanning Tunneling Microscopy Study of TiSe2 Ultrathin Films. *Phys Rev B Condens Matter Mater Phys., 91* (12). DOI:10.1103/PhysRevB.91.121113
24. Liao, M., Wang, H., Zhu, Y., Shang, R., Rafique, M., Yang, L., … & Xue, Q.-K. (2021). Coexistence of Resistance Oscillations and the Anomalous Metal Phase in a Lithium Intercalated TiSe2 Superconductor. *Nat Commun., 12* (1). DOI:10.1038/s41467-021-25671-8

25. Sree Raj, K. A., Shajahan, A. S., Chakraborty, B., & Rout, C. S. (2020). Two-Dimensional Layered Metallic VSe2/SWCNTs/rGO Based Ternary Hybrid Materials for High Performance Energy Storage Applications. *Chemistry - A European Journal*, *26* (29), 6662–6669. DOI:10.1002/chem.202000243
26. Ming, F., Liang, H., Lei, Y., Zhang, W., & Alshareef, H. N. (2018). Solution Synthesis of VSe2 Nanosheets and their Alkali Metal Ion Storage Performance. *Nano Energy, 53*, 11–16. DOI:10.1016/j.nanoen.2018.08.035
27. Oliveira, C. C., & Autreto P. A. (2023). Optimized 2D Nanostructures for Catalysis of Hydrogen Evolution Reactions. *MRS Advances, 8* (6), 307–310. DOI:10.1557/s43580-023-00549-7
28. Yan M., Pan, X., Wang, P., Chen, F., He, L., Jiang, G., … & Mai, L. (2017). Field-Effect Tuned Adsorption Dynamics of VSe_2 Nanosheets for Enhanced Hydrogen Evolution Reaction. *Nano Lett., 17* (7), 4109-4115. DOI:10.1021/acs.nanolett.7b00855
29. Yan, M., Pan, X., Wang, P., Chen, F., He, L., Jiang, G., ... & Mai, L. (2017). Field-Effect Tuned Adsorption Dynamics of VSe2 Nanosheets for Enhanced Hydrogen Evolution Reaction. *Nano Letters, 17* (7), 4109-4115. DOI: 10.1021/acs.nanolett.7b00855
30. Fu, J., Ali, R., Mu, C., Liu, Y., Mahmood, N., Lau, W.-M., & Jian, X. (2021). Large-Scale Preparation of 2D VSe2 through a Defect-Engineering Approach for Efficient Hydrogen Evolution Reaction. *Chemical Engineering Journal, 411*, 128494. DOI:10.1016/j.cej.2021.128494
31. Song, Z., Yi, J., Qi, J., Zheng, Q., Zhu, Z., Tao, L. …, & Gao, H.-J. (2022). Line Defects in Monolayer $TiSe_2$ with Adsorption of Pt Atoms Potentially Enable Excellent Catalytic Activity. *Nano Res., 15* (5), 4687–4692. DOI:10.1007/s12274-021-4002-y
32. Toh, R. J., Sofer, Z., & Pumera, M. (2016). Catalytic Properties of Group 4 Transition Metal Dichalcogenides (MX2; M = Ti, Zr, Hf; X = S, Se, Te). *J Mater Chem A Mater.*, *4* (47), 18322–18334. DOI:10.1039/c6ta08089h
33. Huang, H. H., Fan, X., Singh, D. J., & Zheng, W. T. (2020). Recent Progress of TMD Nanomaterials: Phase Transitions and Applications. *Nanoscale, 12* (3), 1247–1268. DOI:10.1039/c9nr08313h
34. Chowdhury, T., Sadler, E. C., & Kempa, T. J. Progress and Prospects in Transition-Metal Dichalcogenide Research beyond 2D. *Chem Rev.*, *120* (22), 12563–12591. DOI:10.1021/acs.chemrev.0c00505
35. Chhowalla, M., Liu, Z., & Zhang, H. (2015). Two-dimensional Transition Metal Dichalcogenide (TMD) Nanosheets. *Chem Soc Rev., 44* (9), 2584–2586. DOI:10.1039/c5cs90037a
36. Pasquier, D., & Yazyev, O. V. (2018). Excitonic Effects in Two-dimensional $TiSe_2$ from Hybrid Density Functional Theory. *Phys Rev B., 98* (23). DOI:10.1103/PhysRevB.98.235106
37. Kadiwala, K., Butanovs, E., Ogurcovs, A., Zubkins, M., & Polyakov, B. (2022). Comparative Study of WSe_2 Thin Films Synthesized via Pre-deposited WO3 and W Precursor Material Selenization. *J Cryst Growth., 593*. DOI:10.1016/j.jcrysgro.2022.126764
38. Kwak, T., Lee, J., So, B., Choi, U., & Nam, O. (2019). Growth Behavior of Wafer-Scale Two-dimensional MoS 2 Layer Growth Using Metal-Organic Chemical Vapor Deposition. *J Cryst Growth, 510,* 50–55. DOI:10.1016/j.jcrysgro.2019.01.020
39. Xue, Y., Zhang, Y., Wang, H., Lin, S., Li, Y., Dai, J.-Y., & Lau, S. P. (2020). Thickness-Dependent Magnetotransport Properties in 1T VSe_2 Single Crystals Prepared by Chemical Vapor Deposition. *Nanotechnology, 31* (14), 145712. DOI:10.1088/1361-6528/ab6478

LATVIAN JOURNAL OF PHYSICS
AND TECHNICAL SCIENCES
2024, N 2

DOI: 10.2478/lpts-2024-0010

THE FIRST APPLICATION OF LASER-INDUCED BREAKDOWN SPECTROSCOPY: A FAST-ANALYTICAL TECHNIQUE IN TARGETED SEARCH FOR ELEMENTS IN GEOLOGICAL SAMPLES FROM DEEP BOREHOLES IN LATVIA

R. A. Ganeev [1,*], V. V. Kim [1], D.Vorobyov [2], U. Gross [3], A. Ubelis [3],
D. Ozols [4], J. Butikova [5], J. Grube [5], A. Sarakovskis [5]

[1] Laboratory of Nonlinear Optics,
Institute of Astronomy at the National Science Platform FOTONIKA-LV,
University of Latvia,
3 Jelgavas Str., Riga, LV – 1004, LATVIA
[2] University of Latvia,
1 Jelgavas Str., Riga, LV – 1004, LATVIA
[3] National Science Platform FOTONIKA-LV, University of Latvia,
4 Šķūņu Str., Riga, LV-1050, LATVIA
[4] Nature Conservation Agency of Latvia,
7 Baznīcas Str., Sigulda, LV-2150, LATVIA
[5] Institute of Solid State Physics, University of Latvia,
8 Kengaraga Str., Riga, LV-1063, LATVIA
*e-mail: rashid.ganeev@lu.lv

Laser-induced breakdown spectroscopy (LIBS) provides a rapid, cost-effective, and extra-sensitive analysis of geological samples to make preliminary conclusions about the presence of valuable elements up to the trace levels in the ore. We present the first results of a highly sensitive qualitative analysis of the core samples of geological ore from two boreholes in Latvia (Staicele 1, from a depth range of 794–802 m, and Garsene (Subate) 2A, from a depth range of 1102–1103 m) using LIBS. Our measurements using this technique confirmed the high iron content and indicated traces of rare and high in-demand metals (such as Ti, V, Co, Sm, etc.) in the sample from Staicele, renewing interest in studying boreholes across Latvia. The presented pilot studies demonstrated effectiveness and unique possibility in performing a very sensitive and time-saving qualitative analysis of the composition of samples of ores from the old but still valuable borehole cores by using the LIBS method. We compare these measurements with other methods of sample analysis.

Keywords: *Deep boreholes, geological samples, laser-induced breakdown spectroscopy, valuable elements in the ore.*

1. INTRODUCTION

Mineral magnetite $Fe^{2+}Fe_2^{3+}O_4$ is the main compound of iron ores. Magnetic anomalies caused by magnetite iron ores have been known in Latvia for a long time. They were identified in the northern, southern, and central parts of the country in several studies in the 1960s and described in the book [1]. Gneiss with a high content of magnetite was firstly discovered within a borehole at Staicele, in the northern part of the magnetic belt crossing Latvia in a north-south direction [2], [3].

Staicele and Garsene (Subate) deposits are located in the Latvian–East Lithuanian (LEL) tectonic block (Fig. 1) that consists of gneisses, schists, and amphibolite and includes numerous magnetic anomalies [3], [4]. The concentration of metal ores took place during the metamorphism. In total, more than 26 billion tons of iron ore reserves have been estimated across the country [5]. In the 1980s, costly drillings were carried out and core samples of iron ore from wells were collected and studied. Iron-rich ores were formed in the Proterozoic by deposition of iron compounds on the sea floor after which they were metamorphosed. During their formation the some ores (i.e., Garsene deposit, Sample #2) were enriched during underwater volcanism [5].

The additional value of iron ores deposits is presence of metals and other elements, i.e., manganese, cobalt, phosphorus, etc. in concentrations raising interest owing to steady progress in extraction technologies [6]. The use of advanced methods of materials analysis is a way to determine the iron content and to reveal the traces of the rare and high-demand metals.

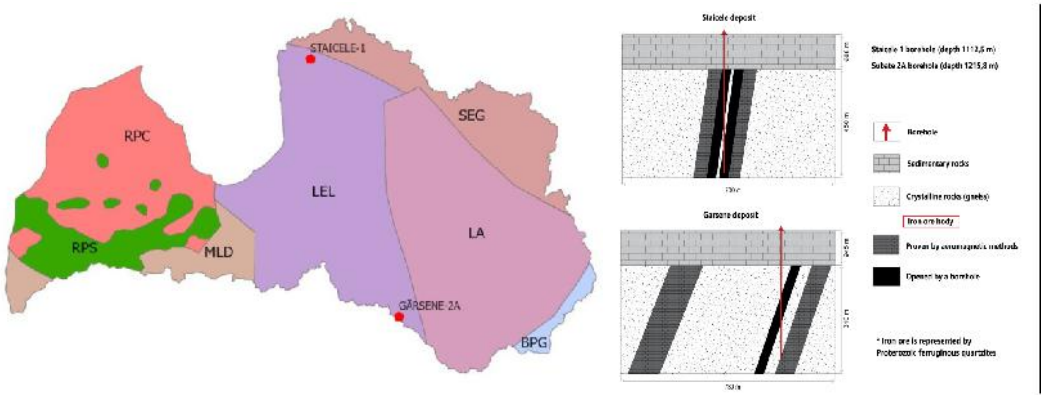

Fig. 1. Locations of the examined iron ore deposits and geological structure of ferruginous quartzite deposits.

Left panel: locations of the studied iron ore deposits – Staicele-1 and Garsene (Subate)-2A and the disposition of the crystalline basement tectonic complexes of Latvia (modified after [3] and [4]): RPC – Kurzeme Pluton Central part – rapakivi granites; RPS – South Kurzeme Pluton South – anorthosites and gabbro-norites; MLD – Mid Lithuanian Domain (West Lithuanian Granulite Belt); LEL – Latvian–East Lithuanian gneiss and amphibolite block; SEG – South Estonian (Estonian-Latvian) granulite belt; LA – Latgalian granite and gneiss block; BPG – Belarus–Podlasie granulite belt.
Right panel: geological structure of ferruginous quartzite deposits – Staicele (according to Staicele 1 exploration borehole) and Garsene (Subate) (according to Subate 2A exploration borehole) in LEL tectonic domain of northern and southern zones (modified after [5] by D. Vorobyov interpretation).

This article presents the results and preliminary conclusions of the pilot studies of elemental composition of two samples of magnetite ores obtained in the 1980s from the boreholes at Staicele and Garsene (Fig. 1, left panel) using the most advanced and sophisticated current method available: laser-induced breakdown spectroscopy (LIBS). The data were compared with results obtained by other methods of material analysis: X-ray diffractometry (XRD), energy-dispersive X-ray fluorescence (EDXRF), and scanning electron microscopy with energy-dispersive X-ray spectroscopy (SEM-EDX). Core samples were obtained from deposits at drilling depths of up to 1 km and deeper (Fig. 1, right panel). The full collection of materials is located in the core sample storage facility at Gardene (at the Latvian Environment, Geology and Meteorology Centre in the municipality of Dobele).

2. EXPERIMENTAL ARRANGEMENTS AND DESCRIPTION OF SAMPLES

LIBS is a sophisticated spectrometric technique [7] applicable to the direct, highly sensitive, and non-destructive spectral analysis of objects of various origins (interacting only with hundreds of ng to a few μg of the sample material). It is used to measure the concentration of macro- and micro-components in solid, liquid, and air samples. The advantage of the method is a relatively simple experimental setup, which includes a laser, a focusing system, a detector, a spectral device, and a data processing system (Fig. 2), and an exceptional ability to indicate the presence of very small concentrations of elements in the sample. Samples for use in the LIBS method of analysis are quick to prepare and enable spectral recording and simultaneous spectral identification [8].

The method is based on the study of the emission spectrum from the plasma induced by a highly energetic, short laser pulse focused on the surface of the sample. The spectral emission characteristics from laser-induced plasma produced on the surfaces of selected samples are analysed in the UV to near-infrared spectral regions.

The experimental procedure is as follows. Laser pulses (HP), with a duration of 150 ps at the wavelength λ=1064 nm and with energies E_{HP} = 15 mJ, were focused using a silica glass lens (L) with a focus of 300 mm. The time delay between the laser pulse and the registration of spectra (integration time T_{int}=1 μs) was controlled by a trigger signal (TS). The delay was fixed at 200 ns to reduce the influence of the continuous plasma emissions at the early stages of laser-induced plasma formation. The spectra were registered using the collecting optics (CO), spectrometer (SP), and iCCD camera.

Laser-induced ablation forms a crater on the sample surface with a typical diameter of 30–400 μm. Laser plasma can be created at any point of any material regardless of its aggregate state. The ablation of atoms from the surface of the sample is induced by a laser pulse for a few tens of nanoseconds, heating the targeted point on the sample surface resulting in electron temperatures of the plasma up to 10 eV and ensuring the excitation of resonance spectra of atoms and even ions of elements present in the sample [9]. It is possible to study a composition (up to trace level) of a very wide range of completely different materials (various gaseous mixtures, metals, alloys, organic samples, geological ores, and minerals, etc.) [10]. As it has been mentioned above, an additional advantage of LIBS technology is the possibility to perform a fast analysis of the composition of elements in various places of borehole core samples for a highly sensitive search for the inclusions of exotic elements. Particularly, LIBS is considered to be practically indispensable for the detection of light elements such as lithium and beryllium, which are problematic for other spectroscopic methods [11].

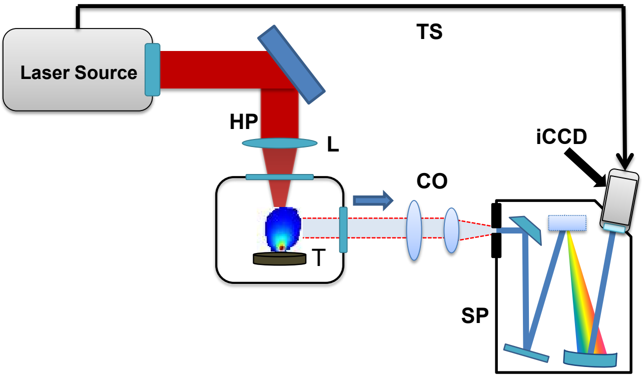

Fig. 2. Experimental scheme for LIBS. Laser source – 150 ps pulses at 1064 nm, TS – a trigger signal from a laser source, HP – a heating pulse, L – 300 mm focusing lens, T – a target, SP – a spectrometer, CO – collecting optics, iCCD – detector (intensified CCD camera).

Samples collected for analysis were the rare and unique geological materials from the boreholes in Latvia’s two largest and most promising deposits – Staicele and Garsene. Each of these two fields has one geological exploration well: named Staicele 1 (at Staicele) and Subate 2A (1979) (at Garsene). The analysed geological materials were taken from the core samples at certain depths, i.e., from the layers of the deposits with the richest magnetite content.

Traces of some elements, such as cobalt, titanium, vanadium, etc., are currently becoming critically important for the EU industry. Particularly, the mass fraction of V_2O_5 reached 0.2 %, as it was determined during the studies performed by the aforementioned instrumentation at the Faculty of Chemistry of the University of Latvia. Staicele iron deposit ores (Sample #1 from a depth range of 794–802 m) have the same history but, in addition, contain a relatively high amount of manganese (the mass fraction of MnO reaches 6.65 %).

3. RESULTS OF LIBS MEASUREMENTS

LIBS measurements were carried out to study the elemental composition of the ore from the Staicele deposit (Sample #1) where the main mineral is magnetite. For the analysis of the selected sample, the laser beam was pointed at the zone with the largest area of magnetite to initiate and study ablation plasma. Table 1 presents the data from the LIBS analysis of Sample #1, comprising a complete list of all elements found in the spectra of LIBS based on the spectra of the studied sample (Fig. 3). These results include the common and intense resonance spectra lines of core elements (iron, manganese, and silicon), as well as the presence of atomic resonance lines of many other elements, including rare earth elements at trace levels, which are important for the industry [12].

Table 1. Elements Detected by the LIBS Method in a Sample of Magnetite Matrix #1 from the Staicele Deposit Evidenced by their Main Resonance Lines

Element	Wavelength, nm	Element	Wavelength, nm
Rb	354.115	Ca	393.366
Fe	355.492	Ca	396.846
Cr	357.868	Tb	400.547
Pm	374.586	Ga	403.298
U	375.834	Mn	404.135
Cr	381.543	Tc	404.911
Fe	382.444	Mn	405.554
Ho	382.927	Th	405.925
Tc	383.282	V	406.392
In	383.465	Fe	407.173
Tm	383.820	Mn	407.941
Mg	383.829	Co	411.877
Pr	384.659	Gd	413.228
Dy	386.880	Mo	414.355
Th	388.691	Gd	426.012
Si	390.552		

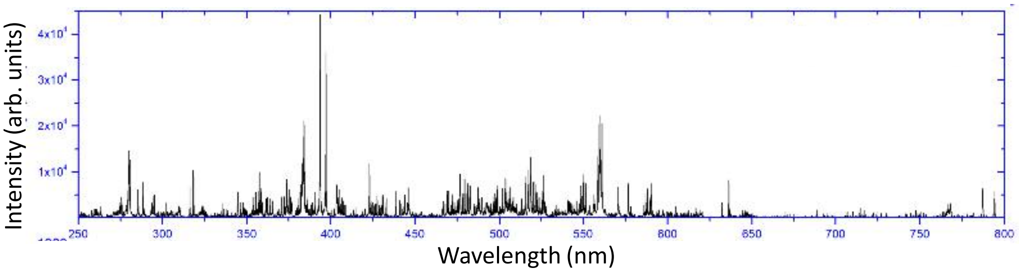

Fig. 3. Example of LIBS plasma emission of Sample #1 (magnetite matrix from the Staicele deposit) recorded 200 ns after ablation by 150 ps laser pulse. The intense lines represent the atoms of the main components in the sample. The interpretation of the spectrum in the region of 354–427 nm is given in Table 1.

Analysis of the spectra obtained from Sample #1 evidenced the presence of the traces of various lanthanides, such as Gd (gadolinium), Tb (terbium), Dy (dysprosium), Pr (praseodymium), Tm (thulium), Ho (holmium), and Pm (promethium). Resonance lines of the atoms of actinides, e.g., U (uranium), Th (thorium), and Tc (technetium), were also present in the spectra. Tc (technetium) is formed due to the radiative decay of radioactive U (uranium) and Th (thorium) isotopes. The presence of Mo (molybdenum), Co (cobalt), V (vanadium), Ga (gallium), In (indium), Cr (chromium), and Rb (rubidium) is evidenced by the typical atomic spectra of the elements mentioned.

The presence of the main components (Fe, Mn, and Si) in the Staicele samples, as well as small amounts of a few other elements (particularly rare earth elements), was also confirmed by other methods. For comparison with our LIBS measurements of Sample #1 resulting in the identification of a large list of elements, we present the results obtained by other methods, leading to the identification of the presence of only a few elements with low concentrations. The measurements using SEM-EDX were carried out by targeting micro-inclusions in the studied samples differing from the main ore mass by visual signs (colour, lustre, fracture, cleavage), which are rather difficult to diagnose by the XRD method.

XRD and EDXRF were made available at the Faculty of Chemistry of the University of Latvia and the Assay Office of Latvia to analyse the elemental content and other characteristics of the two samples and compare them with the LIBS experiment. X-ray diffraction diagram of two studied samples of magnetite ore confirmed the presence of magnetite (Fig. 4).

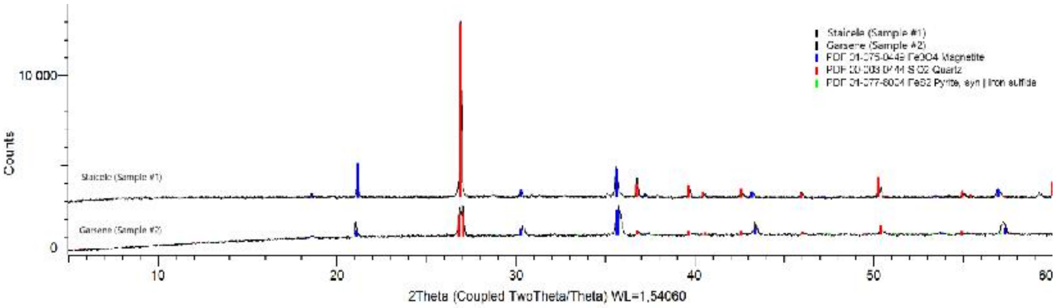

Fig. 4. X-ray diffraction diagram of two studied samples of magnetite ore confirming the presence of magnetite. Further studies of the samples were carried out precisely in the magnetite matrix of the samples.

The elemental qualitative analysis was performed using the EDXRF method. From the comparison of the results of the EDXRF method with the XRD data, it can be concluded that the iron in the samples is in the form of magnetite and pyrite (FeS_2).

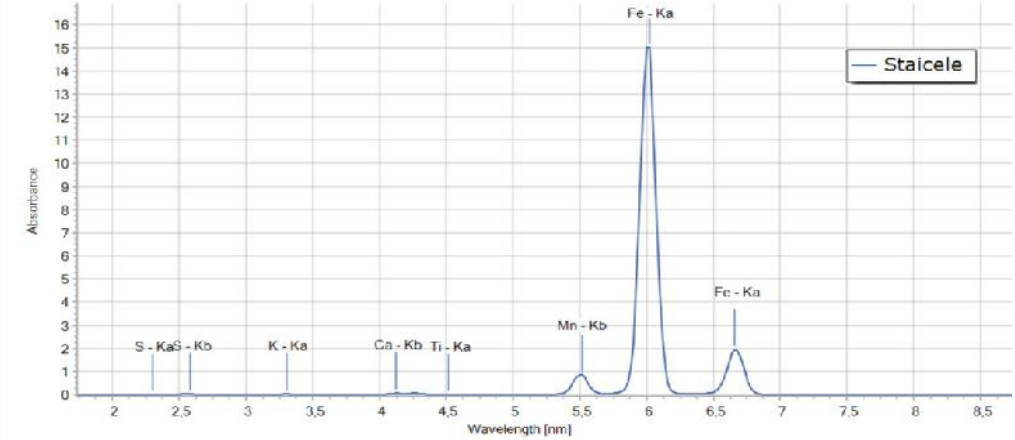

Fig. 5. Example of EDXRF results of Sample #1 from Staicele deposit, which shows a high content of iron in the sample, as well as the impurities of other elements, which are in the form of micro-inclusions of minerals in the studied ore matrix.

The spectrum (Fig. 5) clearly shows that the EDXRF confirmed the presence of the elements, which, in addition to manganese and titanium, can be contained in other associated minerals – ingrowths, e.g., pyrite and various other silicates.

Other minerals, for example, annite - $KFe^{2+}_3(AlSi_3O_{10})$ $(OH)_2)$, from the biotite group, and almandine - $Fe^{2+}_3Al_2(SiO_4)_3]$ rarely found in samples are also the sources of iron. These minerals are found in small quantities, but still can be sources of other "exotic" elements available to advanced extraction methodologies despite small concentrations in the mineral (Fig. 5, Table 2). The largest contributor of iron to the ore is magnetite, which was confirmed in the previously presented spectra and ensured its strong magnetism.

Table 2. Elements Detected by the EDXRF Method in the Samples of the Magnetite Matrix #1 and Matrix #2 from the Staicele and Garsene Deposits

Oxide of element	Sample #1 (Staicele)	Sample #2 (Garsene)
	W, %	
Si_O2	51.9	35.6
Fe_2O_3	36.0	52.4
MnO	5.17	0.03
Al_2O_3	5.01	3.49
MgO	-	3.43
CaO	1.03	1.94
K_2O	0.65	0.17
TiO_2	0.19	-
SO_3	0.09	-
P_2O_5	-	2.72
V_2O_5	-	0.197
Y_2O_3	-	0.008
CuO	-	0.023

The EDXRF data (Table 2) contain information about the elements that were not diagnosed with LIBS (potassium, titanium). This difference is explained by the fact that the EDXRF method analyses the larger surface of the sample. At the same time, its definition boundary is much smaller than that of LIBS, so the data 1 and 2 of Table 2 are distinguishable. In this case, EDXRF shows the main chemical composition of the analysis zone. Meanwhile, LIBS shows the part of the same zone with the presence of elements that EDXRF cannot determine.

The ablation spectra of the geological core sample (#2) from Garsene were measured and compared with the ablation spectra of a pure iron sample (see the recordings of spectra in Fig. 6). This was carried out using pulse energy of 17–20 mJ, pulse duration of 28 ps, an integration time of 2 s, and a delay of 1 sec between the heating pulse and the ICCD gate.

Sample #2 came from a geological core at a drilling depth of 1102–1103 m. Sample #2 appears to be a shiny black mass of magnetite ($Fe^{2+}Fe^{3+}{}_2O_4$) with yellow scar inclusions. Weak yellow inclusions may comprise pyrite (FeS_2), pyrrhotite (Fe_7S_8), or troilite (FeS). The remarkable content of Co, Mn, and several other elements was foreseen earlier based on general considerations and literature data [6].

The black curves in the recorded LIBS plasma spectra of Sample #2 in Fig. 6 are the non-calibrated experimental data. The red, green, and blue curves are taken from the NIST data [13]. The atomic spectrum of Fe from the NIST tables was compared with the LIBS plasma spectra of Sample #2 and the highest purity Fe sample.

The spectra obtained from highest purity Fe show relatively good coincidence with NIST data for Fe I and Fe II, evidencing the proper calibration of our spectrometer. The spectrum of Sample #2 coincides well with the spectra of atomic Fe I and Fe II of an elemental sample of Fe, which means that Sample #2 was predominantly iron.

In contrast to Sample #1, we were unable to find the resonance lines of other metals, even at a trace level. Such a result can be explained by the fact that the position of target ablation in LIBS analysis was located in a crystal of pure magnetite. This is valuable information from a mineralogical point of view, emphasising the advantage of using LIBS in a geological sample analysis.

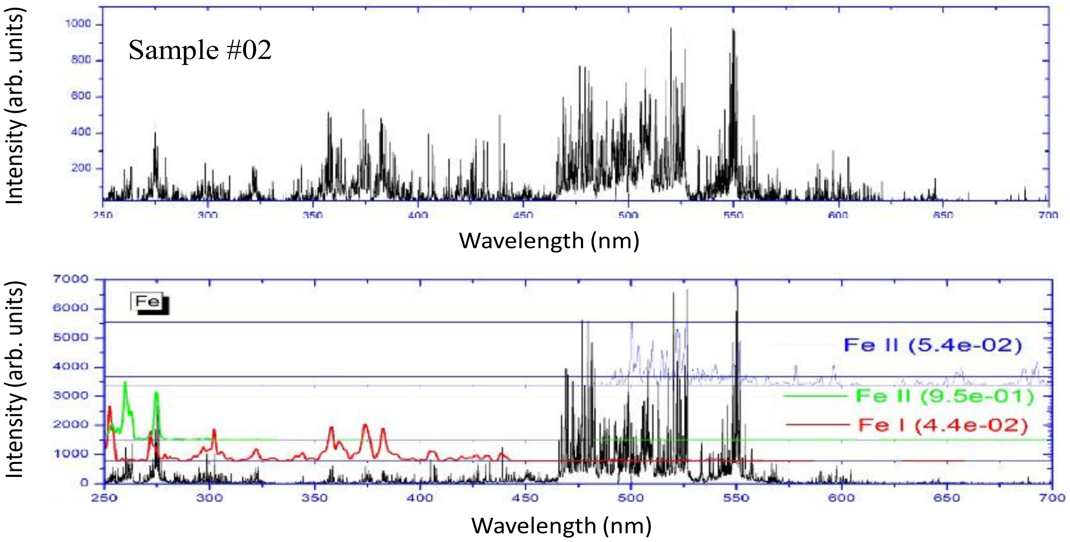

Fig. 6. Upper panel: LIBS of Sample #2 from the Garsene – Subate 2A (1979) borehole. Bottom panel: spectrum of pure iron measured using LIBS. Blue, green, and red spectra are taken from [13] for the iron atoms and ions.

4. DISCUSSION AND CONCLUSION

These pilot studies demonstrated the value and need for further applications of the LIBS technique in studies of Latvian geology, among others, intending to discover economically usable metal ores in crystalline basement rocks at depths ranging from 300–1900 m [4]. The data of XRD were included for comparison with the results obtained using LIBS. Repeated analyses were carried out to confirm the conclusions made using the LIBS. XRD method showed the main mineralogical composition of the studied zone within the detection limits of 0.5%. This made it possible to show the main mineralogical composition excluding microinclusions of other minerals, since this method does not allow studying such small inclusions. Therefore, SEM-EDX was used to recognise microinclusions. This allowed confirming the mineralogy described in previous studies. We did not carry out detailed studies using above methods while considering it sufficient to describe the data in the form of mentioning the minerals without attaching the spectrum to each inclusion, since in this article we were concentrated on the studies of LIBS.

We also included the results of the EDXRF of our samples. The analysis was performed in the same place as LIBS, but the results still differed slightly due to the specifics of these two methods. Due to the fact that the area for EDXRF is larger, a slightly different result is obtained due to the fact that more magnetite matrices with microinclusions of other minerals fall into the analysis area. The advantage is that EDXRF confirms both the presence of the main elements that are part of the minerals diagnosed by the XRD method and those found by the LIBS method. Meanwhile, LIBS in turn shows the content of other useful elements reliably detected by this method, while EDXRF cannot show the content of these elements. Therefore, it is possible to predict the prospects for the use of ores from these two deposits using LIBS. The locations of the deposits are shown in the schematic geological map (Fig. 1), drawn on the basis of the data available in the literature. In Western Latvia, where the basic intrusions are located, the presence of various metals, including precious metals, is possible. The LIBS method could be particularly useful in studies of such deposits.

In conclusion, our studies have shown that the LIBS methodology has the unique ability to conduct sensitive, efficient, not time-consuming qualitative investigations of ore compositions. In the case of core Sample #1 from Staicele, the LIBS technique demonstrated the ability to identify tiny amounts of priceless substances that should be considered for extraction. The presence of Mo, Co, V, Ga, In, Cr, and Rb, and traces of several lanthanides including Gd, Tb, Dy, Pr, Tm, Ho, and Pm (as well as the actinides U, Th, and Tc) were discovered and compared to past examinations.

The results of the study of core Sample #2 by the LIBS method, demonstrated a high iron content and the presence of silicone-based minerals. The presence of iron was confirmed by other techniques that were earlier applied to this sample. Iron was indicated as the second element after silicon at a mass fraction reaching 37 %. The important finding during the application of LIBS technologies in the case of the core sample from Garsene (Sample #2) is a confirmation of the absence of other metals and rare elements identified in the core sample from Staicele (Sample #1), even at a trace level, providing the important information for eventual planning on future exploitation of relevant ores. Our pilot studies, using LIBS methods, show the possibility to obtain promising and remarkable added value, in the case of comprehensive renewed studies of already existing geological borehole core samples related to geology and prospective industrial extraction of various components as well.

ACKNOWLEDGEMENTS

We would like to thank the Institute of Solid State Physics (University of Latvia) that, as the Center of Excellence, has received funding from the European Union's Horizon 2020 Framework Programme H2020-WIDESPREAD-01-2016-2017-TeamingPhase2 under grant agreement No. 739508, project CAMART and European Regional Development Fund (1.1.1.5/19/A/003).

REFERENCES

1. Kuršs, V., & Stinkule, A. (1963). *Mineral Resources in Latvia* (in Latvian). Riga: Zinātne.
2. Birger, A. (1979). Ore occurrence (in Russian). In *Geologicheskoe stroenie i poleznie iskopaemie Latvii,* J. P. Misans (ed.), (p. 448). Riga: Zinātne.
3. Birķis, A. (1979). Archaean and proterozoic groups (in Russian). In *Geologicheskoe stroenie i poleznie iskopaemie Latvii*, J.P. Misans (ed.), (pp. 7–17). Riga: Zinātne.
4. Karušs, J. (2018). Paleosurface and tectonic structures of the crystalline basement (in Latvian). In *Latvija. Zeme, daba, tauta, valsts,* I. Zarāne (ed.), (pp. 80–81). Riga: Latvijas Universitātes Akadēmiskais apgāds.
5. Vetrennikov, V. (1984). Report on the results of work on the topic: the study of iron ore formations of the Precambrian of the Latvian SSR (in Russian). *Skrunda, 1*, 308.
6. *Segliņš, V., & Brangulis, A. (eds.).* (1996). Mineral resources of Latvia (in Latvian). *Latvijas zemes dzīļu resursi. Valsts* Ģeoloģijas *dienests* (pp. 19–25). Riga.
7. Pasquini, C., Cortez, J., Silva, L. M. C., & Gonzaga, F. B. (2007). Laser Induced Breakdown Spectroscopy. *J. Brazil. Chem. Soc. 18* (3), 463–512.
8. Noll, R., Mönch, I., Klein, O., & Lamott, A. (2005). Concept and Operating Performance of Inspection Machines for Industrial Use Based on Laser-Induced Breakdown Spectroscopy. *Spectrochem. Acta B, 60* (7), 1070–1075.
9. Hill, M., & Wagenaars, E. (2022). Modelling of Plasma Temperatures and Densities in Laser Ablation Plumes of Different Metals. *Photonics 9* (12), 937.
10. Marín-Roldán, A., Cruz, J. A., Martín-Chivelet, J., Turrero, M. J., Ortega, A. I., & Cáceres, J. (2014). Evaluation of Laser-Induced Breakdown Spectroscopy (LIBS) for Detection of Trace Element Variation through Stalagmites: Potential for Paleoclimate Series Reconstruction. *J. Appl. Laser Spectrosc., 1* (1), 7–12.
11. Gaft, M., Nagli, L., Gorychev, A., & Raichlin, Y. (2021). Atomic and Molecular Emission of Beryllium by LIBS. *Spectrochimica Acta Part B: Atomic Spectrosc., 182*, 106233.
12. Jha, A. R. (2014). *Rare Earth Materials Properties and Applications.* CRC Press.
13. Kramida, A., Ralchenko, Yu., Reader, J., & NIST ASD Team. (2023). *NIST Atomic Spectra Database (version 5.9)* National Institute of Standards and Technology, Gaithersburg, MD. Available at https://physics.nist.gov/asd

LATVIAN JOURNAL OF PHYSICS
AND TECHNICAL SCIENCES
2024, N 2

DOI: 10.2478/lpts-2024-0011

ENHANCED-REACH POLARIZATION OPTICAL TIME-DOMAIN REFLECTOMETRY TECHNIQUE FOR FIBRE OPTICAL INFRASTRUCTURE MONITORING

J. Braunfelds[1*], S. Spolitis[1,3], D. Cirjulina[2], A. Ostrovskis[3],
J. Porins[4], L. Gegere[1], A. Supe[1]

[1] AFFOC Solutions Ltd.
2-58 Jaunibas Str., Kalnciems, LV-3016, LATVIA
[2] Institute of Microwave Engineering and Electronics,
Riga Technical University
6a Kipsalas Str., Riga, LV-1048, LATVIA
[3] Communication Technologies Research Center,
Institute of Telecommunications,
Riga Technical University
12 Azenes Str., Riga, LV-1048, LATVIA
[4] Institute of Telecommunications,
Riga Technical University
12 Azenes Str., Riga, LV-1048, LATVIA
*e-mail: janis.braunfelds@rtu.lv

This interdisciplinary research is focused on constructing and demonstrating enhanced-reach polarization optical time-domain reflectometer (POTDR) for monitoring single-mode fibre optical communication lines. An optical signal state of polarization measurements enables several new possibilities for real-time monitoring solutions in fibre optics. However, there is no commercial equipment available to determine the location in fibre optical cable where the light polarization state changes. The authors present a monitoring technique of an optical signal state of polarization based on reflected signal time-amplitude analysis with improved operation parameters, namely, timing resolution (2 to 3 ps RMS) and amplitude measurement resolution of nanosecond scale pulses (8 to 10 bits) for monitoring of fibre optical communication lines. Additionally, the demonstrated POTDR provides a considerable optical fibre line measurement reach of up to 40 km.

Keywords: *Optical fibres, optical state of polarization, polarization optical time-domain reflectometer (POTDR).*

1. INTRODUCTION

Polarization-related measurements in optical fibre communication lines typically are based on methods that determine only the total polarization mode dispersion (PMD), polarization-dependent loss (PDL) or instantaneous state of polarization (SOP) of optical signal at some specific point. These measurements neither reveal the location or the cause of change in the SOP. Those two aspects are covered in our proposed high-precision time-amplitude analysis method based on time-domain reflectometry. We have tested this technique on localization of outer mechanical impact on fibre causing increased changes in the SOP. However, potentially it can be used to track fibre sections with increased PMD coefficient. This is very essential since PMD is one of the key parameters limiting high-speed signal (>10 Gbps bitrate per data channel) transmission in fibre optical communication systems [1]. Localisation of unusually high SOP changes in the fibre optical network significantly simplifies the detection and elimination of the cause of the problem.

A polarization optical time-domain reflectometer (POTDR) corresponds to a polarization-sensitive optical time-domain reflectometer (OTDR) measurements, which can identify a change in the SOP in a section of the fibre under a test link. In a POTDR setup, a change in the SOP typically is detected as a change of the received signal power, since most of the setups implement an exact SOP as a reference (a change in the SOP from the reference state will cause power penalties). Also, it is essential to mention that by using conventional polarization related measurements, the exact location of the polarization change in an optical fibre line cannot be determined. Instead, it can be detected in an approximate range.

There are different approaches of how to construct a POTDR setup to improve sensitivity, accuracy and measurement range. One of the techniques is to use traditional OTDR and convert it into POTDR using external polarization-sensitive circuitry typically consisting of two 3-port optical circulators and a polarizer as displayed in the measurement setup in Fig. 1 [3], [4], [11]. Accordingly, OTDR trace consists of all reflectivities due to different backscattering mechanisms and additionally also polarization dependent reflected signal amplitude fluctuations, thus identifying changes in the SOP due to specific fibre properties or environmental perturbations. This increases the versatility of the whole monitoring mechanism [3], [4], [11]. POTDR measurements share the same principles as OTDR, including the use of launch cable (typically 300–500 m in length) to reduce a dead zone. Optical circulators are used to separate the transmitted and reflected optical signals. In such measurements, the OTDR must be operated in the real-time mode because averaging of multiple traces hides information about SOP changes. The main disadvantage of real-time mode measurements is the reduced sensitivity of OTDR measurements. As a result, the operating range or reach of this type of POTDR solution is limited to around 20 km [3], [4].

Current research works demonstrate POTDR solutions for PMD measurements in fibre optical communication lines [4]–[6] and distributed fibre optical sensor solutions for strain and vibration monitoring [7]–[13]. POTDR can be used not only in transmission line monitoring but also for a fibre as a sensor system for object perimeter, infrastructure construction, oil and gas pipeline monitoring, etc.

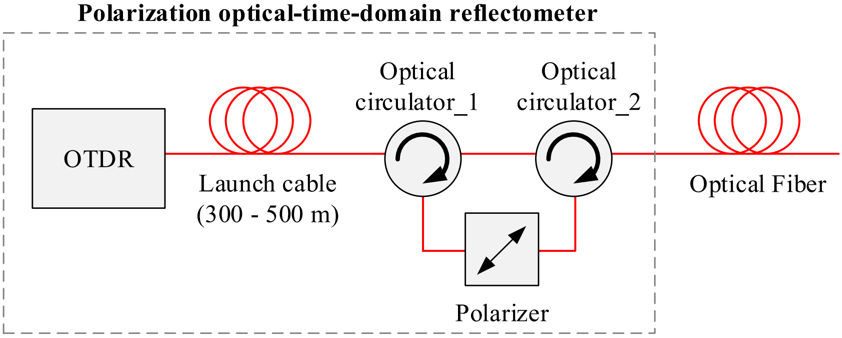

Fig. 1. POTDR measurement setup based on traditional OTDR.

The typical realization of the POTDR measurement setup as demonstrated in [7], [10] is shown in Fig. 2. The pulsed laser source generates POTDR probe pulses. Pulse width and amplitude are adjusted depending on the length of the monitored optical fibre line and its attenuation. The output of the pulsed laser is connected to optical polarizer_1 to attain completely polarized probe pulses. The output of polarizer_1 is connected to the input of the optical circulator, which is used to separate forward travelling and backward reflected optical flows. The common port of the circulator is connected to the launch cable, which, in turn, is connected to the fibre under test. The signal reflected from the optical fibre communication line passes the optical circulator and is therefore directed to Polarizer_2, which converts the changes in the SOP into changes of power. An avalanche photodiode (APD) converts the optical signal into an electrical signal, fed to the signal processor (SP) for further processing.

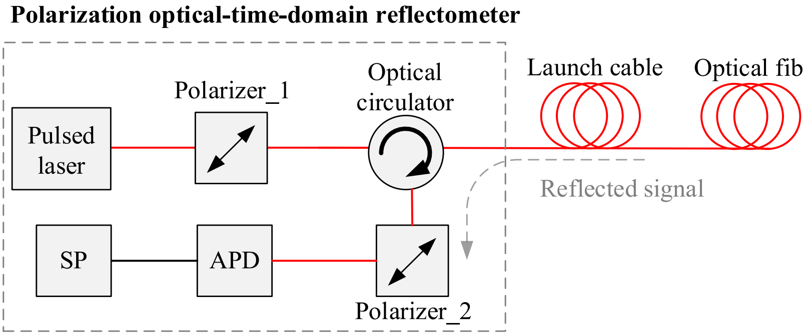

Fig. 2. Typical POTDR block diagram.

Polarization-based effects are stochastic and sensitive to environmental changes (such as temperature, external mechanical impact or even optical fibre vibrations) [1], [3]. Current scientific works [3], [4], [7] report that the operating range of the known POTDR solutions is limited to around 20 km, which is a significant drawback for these measurements. Therefore, it is necessary to develop extended-reach high-accuracy POTDR solutions.

2. POTDR MONITORING SYSTEM

In this research, we demonstrate the setup of an extended reach (up to 40 km) high-accuracy real-time POTDR monitoring system solution (see Fig. 3). Directly-modulated distributed-feedback (DFB) laser is used as the POTDR probe pulse source. The electrical drive signal is generated by a probe pulse generator and fed to the DFB laser RF input. Probe pulse parameters were adjusted depending on the fibre under test length. The typical amplitude (Vpp), frequency (kHz) and pulse width (%) values for 40 km long fibre testing are the following: 2.6 Vpp, 1 kHz, 0.4 %. Since the modulated DFB laser has low output power, an erbium-doped fibre amplifier (EDFA) is used to amplify optical signal up to 4 dBm before launching in the fibre. The use of an optical amplifier increases the power budget and gives the extended measurement range. This approach has not been used widely so far in relation to POTDRs. In [10], it was demonstrated that EDFA extended the reach up to 30 km. Here, we use EDFA in the fixed pump current mode to avoid undesirable gain fluctuations.

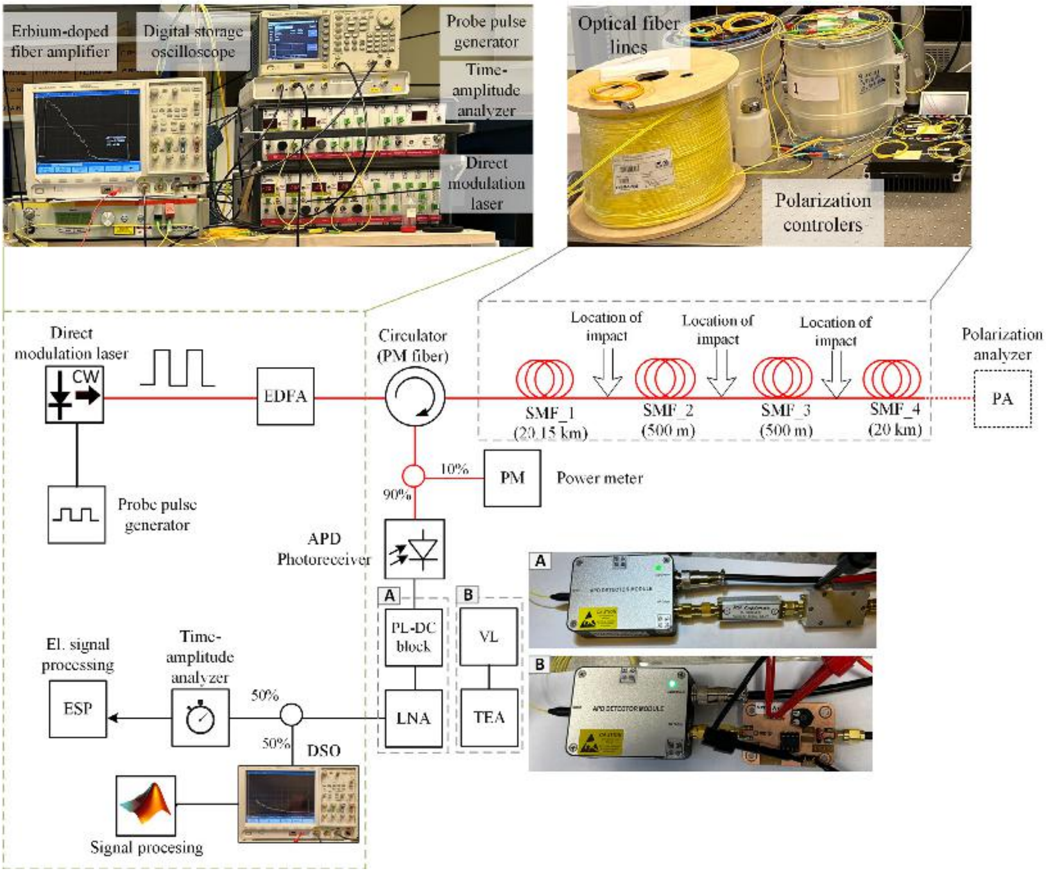

Fig. 3. The developed POTDR measurement setup.

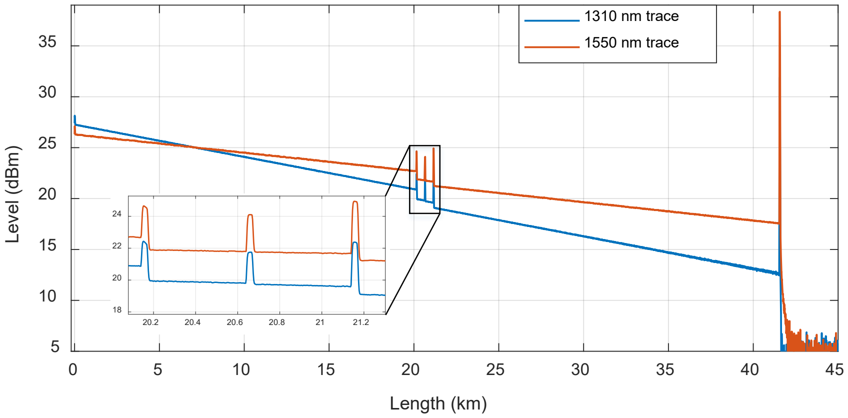

Fig. 4. OTDR trace of the optical fibre under the test line.

As one can see in Fig. 3, the output of the EDFA is connected to a 3-port polarization-maintaining (PM) optical circulator (OC) with an integrated optical polarizer. This type of circulator reduces the need for two optical polarizers (typically being an essential part of POTDR setup (see Fig. 2). This reduces the number of components in the measurement scheme and lowers insertion loss in the probe pulse path. The common port of OC is connected to the optical fibre under the test line consisting of 4 single-mode fibre spans: 20.15 km, 0.5 km, 0.5 km, and 20 km forming the total line length of 41.15 km. Such a number and length of fibre spans are chosen to demonstrate the operation and resolution of the proposed POTDR solution. The measured OTDR trace of this optical line is shown in Fig. 4. The total estimated path loss is 8.77 dB at a reference wavelength of 1550 nm.

Interconnections between fibre spans are used as known locations where the external impact on the optical line can be applied. Here, we consider the case where a mechanical force is applied to the fibre (random vibrations, bending, and torsion). During the initial phase of tests, a polarimeter was used to evaluate the magnitude and nature of SOP changes in the case of external mechanical impact. For comparison, fibre at idle state was also tested to see the PMD-caused test signal SOP variations.

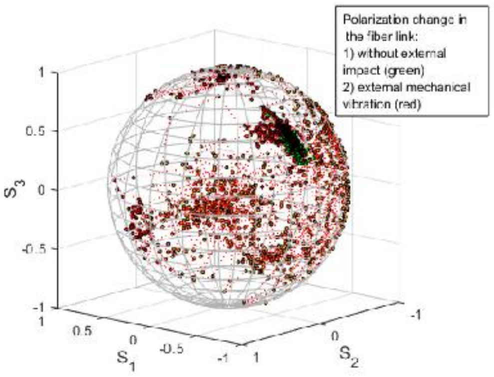

Fig. 5. Poincare sphere with SOP changes in the fibre link:
1) without an external impact (green points); 2) external mechanical vibration applied (red points).

Poincare sphere is used to represent these measurements (see Fig. 5) with and without external impact on optical fibre. Since the fibre vibration/bending causes rather uniform coverage of the Poincare sphere, it was decided to emulate this kind of impact using two motorized polarization controllers (MPCs). Series connection of two quarter waveplate polarizers gives more random SOPs. Figure 6 shows Poincare sphere when MPCs are used. For comparison, green dots represent the case without an external impact.

As one can see in Fig. 3, the reflected optical signal from the optical fibre communication line is transmitted to a non-symmetrical optical power splitter (10/90 %), where the 10 % output port is connected to the optical power meter and the 90 % output port to an APD photodiode with photoreceiver RF bandwidth of 200 MHz (3 dB bandwidth). The optical power meter is only used to monitor the optical power level at the input of the APD.

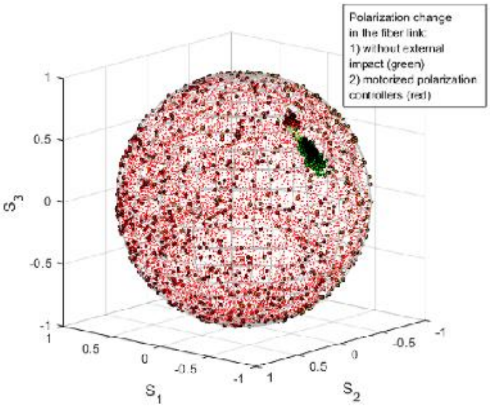

Fig. 6. Poincare sphere with SOP changes in the fibre link:
1) without an external impact (green points); 2) MPC (red points).

The low level optical signal sensitivity of APDs is -47 dBm. Photoreceiver's output electrical signal is, first of all, fed into the amplitude limiter circuitry. Amplitude limiter reduces electrical signal amplifier saturation due to Fresnel reflections from connectors, being much higher than the Rayleigh backscattering. Two electrical signal processing circuit versions are considered in our experimental POTDR measurement setup for signal amplitude limitation and signal amplification:

A. the research team developed voltage limiter (VL) with an adjustable limiting threshold (series positive limiter with bias) and a tunable electrical amplifier (TEA);
B. commercially available power limiter with the direct current block (PL-DC) and fixed 30 dB low noise amplifier (LNA).

The series-positive limiter circuit with bias voltage is presented in Fig. 7. The function of this electronic circuit is to limit the amplitude of an input signal *Vin* considering DC bias offset *VBias*. While the input voltage does not exceed the *VBias*, the diode *D1* will conduct. When the positive *Vin* exceeds *VBias*, the diode becomes reverse biased and limits the positive voltage of the output signal to *VBias*. The reason is that the cathode is positive with respect to the anode, diode *D1* is reverse-biased and will not conduct. The diode *D1* will remain reverse biased until it becomes lower than *VBias*.

The output of the voltage limiter is connected to the operational amplifier (OP-AMP) in voltage repeater mode, also known as a buffer. The buffer divides different stages of the circuit by preventing the input impedance of one stage from loading the output impedance of prior stage, which causes undesirable loss of signal transfer.

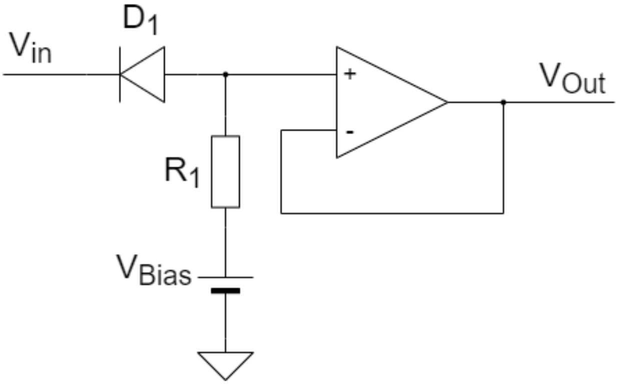

Fig. 7. Series-positive limiter circuit with bias voltage.
$R_1 = 1$ kΩ, D_1 is 1n4148 silicon diode, LT1013 operational amplifier.

The amplified electrical signal is transmitted to the electrical power splitter (50/50 %), where the signal power is split to the digital storage oscilloscope (DSO) and high-precision time-amplitude analyser (timing resolution: 2 to 3 ps RMS), amplitude measurement resolution of nanosecond pulses: 8 to 10 bit). However, time-amplitude measurement is applicable for time interval measurement to get the overall length of fibre cable line (reflections from connectors are high enough to be detected by the timer receiver). Measured time interval is used for digital storage oscilloscope (DSO) measurement data calibration to achieve higher accuracy for location detection of the external impact on the optical line. Simultaneous amplitude measurement enables continuous monitoring of fibre line to detect changes in the fibre under test. Changes in the reflected signal amplitude from the far end of the cable (last connector) can be used as triggering event to start POTDR trace accumulation for further post-processing. MATLAB software is used to process and visualize the signal received from DSO and the time-amplitude analyser.

3. MEASUREMENT RESULTS

The results obtained by constructed POTDR measurement setup are shown in Figs. 8–12. A single POTDR measurement trace is not enough to locate the external impact from the SOP change since fibre under test does not maintain polarization due to internal birefringence. In fact, multiple traces are needed since the change in amplitude fluctuations can be very tiny depending on the distance and the scale of external impact (here represented using MPCs) as can be seen in Fig. 8. The external impact typically creates a tiny change in signal amplitude (millivolts), so the absolute amplitude difference is used for comparison. The data processing involves the following steps:

- calculating the average trace amplitude from all the accumulated POTDR traces;
- finding the absolute amplitude difference (ΔV) of each POTDR trace versus average value;
- accumulation of all ΔV results versus fiber distance and performing moving average filtering (window size 10 points) to reduce data noisiness.

Accumulation of several tenths of traces gives a notable change in the reflected signal amplitude, which reveals the location of external impact. This is studied in more detail by considering a different number of traces and its impact on event location accuracy in the post-processed POTDR trace.

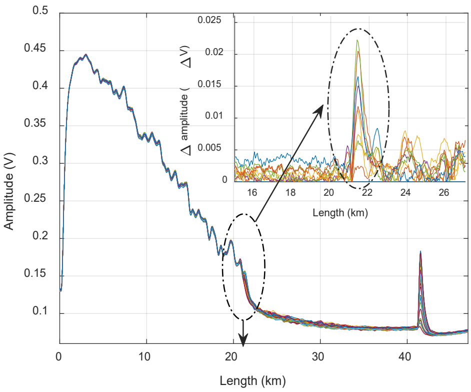

Fig. 8. Delta amplitude calculation and evaluation.

The total absolute amplitude difference accumulated from 5 to 50 real-time POTDR measurement traces at 1550 nm measurement wavelength is considered here (see Fig. 9). As it can be seen, the higher the number of accumulated traces, the more explicit the location of impact. Trace accumulation also raises the total voltage level, thus suppressing the background noise (mainly the EDFA amplified spontaneous emissions and photoreceiver noise) as well as PMD caused power fluctuations. We propose the use of 50 traces; however, finding the optimum number of traces remains a task of further research. The rest of the results (Figs. 10–12) are attained using 50 POTDR trace accumulation.

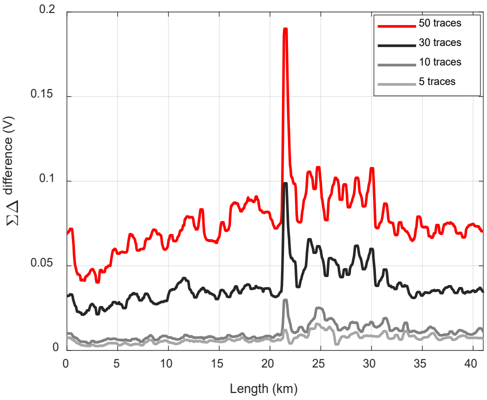

Fig. 9. The number of accumulated POTDR traces versus the absolute amplitude difference in volts.

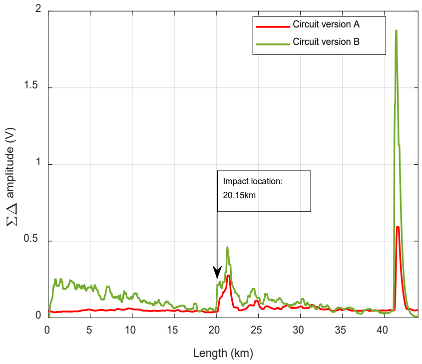

Fig. 10. The accumulated absolute amplitude difference versus fibre length when MPCs are located after the SMF_1 line in the case of electric signal circuitry A and B.

Figures 10 to 12 show results obtained by two electrical signal circuit solutions, where circuit version A uses PL-DC, but B uses AM with an adjustable limiting threshold for amplitude limitation and signal amplification. Figure 10 shows the case when the distance to the location of 2 MPCs is determined to be 20.15 km. Figures 11 and 12 are the cases when the distance to the location of 2 MPCs is determined to be 20.65 km and 21.15 km. All the identified locations correspond to the fibre under the test line with two 500 m spools after 20.15 km.

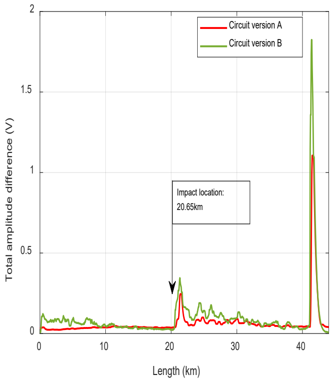

Fig. 11. The accumulated absolute amplitude difference versus fibre length when MPCs are located after the SMF_2 line in the case of electric signal circuitry A and B.

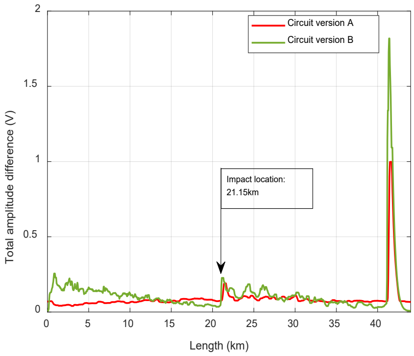

Fig. 12. The accumulated absolute amplitude difference versus fibre length when MPCs are located after the SMF_3 line in the case of electric signal circuitry A and B.

As it can be seen in Figs. 10–12, in all cases it is possible to detect accurately the location of external impact from 2 MPCs using both (A and B) circuit versions. The combination of PL-DC and LNA gives less noisy trace, thus giving more noticeable location of external impact. On the other hand, the VL – TEA version produces higher fluctuations amplitude and more distinct front of the event. As it has been mentioned previously, in all cases the total length of fibre under test (41.38 km) has been determined using time-amplitude analyser with timing resolution of 2 to 3 ps RMS. The total length is afterwards used as the reference for DSO measurements.

4. CONCLUSIONS

In this research, the enhanced-reach POTDR technique was experimentally developed for real-time monitoring of the fibre optical infrastructure. The research presented a monitoring technique of an optical signal state of polarization based on reflected signal time-amplitude analysis with improved operation parameters, namely, timing resolution (2 to 3 ps RMS) and amplitude measurement resolution of nanosecond scale pulses (8 to 10 bits) for monitoring of fibre optical communication lines. This technique can detect the location of external impacts (mechanical vibrations, strain, etc.) on the optical fibre lines. The demonstrated POTDR provides a considerable optical fibre line measurement reach of up to 40 km.

ACKNOWLEDGEMENTS

The research has been funded by the European Regional Development Fund (ERDF) project “Technology for High-Precision Time-Amplitude Analysis of Event Flow (TIME-AMP)”, No. 1.1.1.1/20/A/076.

REFERENCES

1. Dubovan, J., Litvik, J., Benedikovic, D., Mullerova, J., Glesk, I., Veselovsky, A., & Dado, M. (2020). Impact of Wind Gust on High-Speed Characteristics of Polarization Mode Dispersion in Optical Power Ground Wire Cables. *Sensors*, *20* (24), 71102020. DOI:10.3390/s20247110.
2. Salgals, T., Supe, A., Bobrovs, V., Porins, J., & Spolitis, S. (2021). Comparison of Dispersion Compensation Techniques for Real-Time up to 160 Gbit/s DWDM C-Band Transmission. *Elektronika ir Elektrotechnika*, *27* (4). DOI:10.5755/j01.eie.26.2.25892.
3. Braunfelds, J., Spolitis, S., Gegere, L., Pikulins, D., Stepanovs, V., & Supe, A. (2022). Demonstration of polarization optical-time-domain reflectometer for monitoring of optical fiber lines. In *2022 Workshop on Microwave Theory and Techniques in Wireless Communications (MTTW)*, (pp. 9–12). 5–7 October 2022, Riga, Latvia. DOI: 10.1109/MTTW56973.2022.9942583.
4. Franciscangelis, C., Floridia, C., Simões, G., Schmidt, F., & Fruett, F. (2015). On-field Distributed First-Order PMD Measurement Based on pOTDR and Optical Pulse Width Sweep. *Optics Express, 23* (10). DOI: 10.1364/OE.23.012582.

5. Huttner, B., Gisin, B., & Gisin, N. (1999). Distributed PMD Measurement with a Polarization-OTDR in Optical Fibers. *Journal of Lightwave Technology*, *17* (10), 1843–1848. DOI: 10.1109/50.793764.
6. Wuilpart, M., Ravet, G., Mégret, P., & Blondel, M. (2002). Polarization Mode Dispersion Mapping in Optical Fibers with a Polarization-OTDR. *IEEE Photonics Technology Letters*, *14* (12), 1716–1718.
7. Xiong, B., Luo, X., Gu, J., Li, M., Wang, F., & Dou, R. (2020). A POTDR System Based on Dual Sensing Directions. *IEEE Photonics Journal*, *12* (2), 1–8. DOI: 10.1109/JPHOT.2020.2979903.
8. Palmieri, L., & Galtarossa, A. (2021). Distributed Polarization-Sensitive Reflectometry in Nonreciprocal Single-Mode Optical Fibers. *J. Lightw. Technol.*, *29* (21), 3178–3184.
9. Rogers, A. J. (2000). Distributed Measurement of Strain Using Optical-Fibre Backscatter Polarimetry. *Strain*, *36* (3), 135–142.
10. Song, M., Yin, C., Xia, Q., Lu, Y., & Zhu, W. (2017). Development of Distributed POTDR with Analyzers of Different SOP Directions. *AIP Conf. Proc., 1839* (1), 020100. DOI: 10.1063/1.4982465.
11. Wang, F., Zhang, Y., Wang, W., Dou, R., Lu, J., Xu, W., & Zhang, X. (2018). Development of a Multiperimeter Sensing System Based on POTDR. *IEEE Photonics Journal*, 10 (3), 1–7, 7102907. DOI: 10.1109/JPHOT.2018.2832186.
12. Wang, F., Zhang, X., Wang, X., & Chen, H. (2013). Distributed Fiber Strain and Vibration Sensor Based on Brillouin Optical Time-Domain Reflectometry and Polarization Optical Time-Domain Reflectometry. *Opt. Lett.*, *38*, 2437–2439. DOI:10.1364/ol.38.002437.
13. Bai, Q., Wang, Q., Wang, D., Wang, Y., Gao, Y., Zhang, H., … & Jin., B. (2019). Recent Advances in Brillouin Optical Time Domain Reflectometry. *Sensors*, *19* (8), 1862. DOI: 10.3390/s19081862.

LATVIAN JOURNAL OF PHYSICS
AND TECHNICAL SCIENCES
2024, N 2

DOI: 10.2478/lpts-2024-0012

ENERGY PERFORMANCE OF HIGHER EDUCATION INSTITUTIONS BUILDINGS OPERATING DURING QUARANTINE RESTRICTIONS AND/OR MARTIAL LAW IN UKRAINE

V. Deshko[1], I. Bilous[1]*, T. Boiko[1], O. Shevchenko[1], A. Borodinecs[2], J. Zemitis[2]

[1] National Technical University of Ukraine
“Igor Sikorsky Kyiv Polytechnic Institute”,
Institute of Engineering Thermophysics,
37 Peremohy Ave, Kyiv, 03056, UKRAINE
[2] Riga Technical University,
Department of Heat Engineering and Technology
6A Kipsalas Str., Riga, LV-1048, LATVIA
* e-mail: biloys_inna@ukr.net

During the pandemic and periods of martial law, educational institutions in Ukraine implemented various forms of organising the educational process, combining in-person and remote classes. As a result, there has been a decrease in the level of use of building premises. The analysis of the characteristics of energy consumption in these conditions requires additional attention. In this study, a dynamic energy model of the building was created using the educational building of Igor Sikorsky Kyiv Polytechnic Institute as an example. Energy consumption for heating needs was determined for normal operating conditions and quarantine conditions in Ukraine (only a specific part of the premises is being operated, ensuring that the standard temperature value is maintained while people are present). Based on the results of the study, the features of the energy consumption of the building during quarantine/martial law restrictions, subject to the partial use of the building, were analysed, and the main disadvantages of such a mode were identified. For the educational building of the university, the total energy consumption for heating needs depends on the number of rooms that are actively used, and the modes of regulation of heating and ventilation; the consumption can decrease depending on the chosen scenario by 61 %, 56 %, and 34 % in quarantine mode. The findings indicate that the efficiency of regulation modes can decrease by more than four times when compared to normal mode due to internal heat exchange with unoccupied rooms.

Keywords: *Air exchange, building operation during quarantine and/or martial law, educational institutions, energy consumption, energy saving, hourly infiltration rate, indoor air temperature.*

1. INTRODUCTION

1.1. Overview

At the end of 2019, humanity faced the challenges of the global COVID-19 pandemic, which impacted all spheres of economic and social development worldwide. The most significant challenge was the need for a radical change in approaches to organising and conducting business/work activities. Many organisations implemented remote work arrangements, either fully or partially, wherein employees worked from home or adopted a hybrid model, combining remote work with occasional visits to their workplace. The sphere of education was no exception, including in Ukraine. Therefore, to prevent the spread of COVID-19 and ensure the continuity of learning, educational institutions introduced remote or blended learning formats. In addition to the challenges of the pandemic, in 2022 Ukraine faced full-scale military operations on its territory. Educational institutions have switched to remote mode of operation. The consumption of electricity and water in educational institutions has decreased, but the issue of heating educational institutions remains unresolved. In the conditions of the energy crisis in Ukraine caused by targeted and regular missile attacks on critical energy infrastructure, the energy-efficient use of energy is an urgent issue.

In most educational institutions in Ukraine, operational control of the centralised heating system occurs simultaneously at the system's entry point for the entire building. Therefore, to reduce the use of energy resources, the feasibility of maintaining normative temperature conditions in rooms that are not involved in face-to-face learning during quarantine/war restrictions becomes an additional factor that will alleviate the deficit of generating capacities in the energy system. Currently, the possibilities of such an approach can be explored using dynamic simulation modelling of heat distribution in the premises of the educational building with the construction of a corresponding energy model of the building. Such a model consists of energy characteristics during the partial use of the building. It allows analysing the characteristics of heat consumption during distance learning for different operating modes of heating and ventilation systems, as well as conducting simulations and evaluating the heat exchange between rooms with different operating modes. This will enable making informed decisions regarding the more compact placement of certain departments within the educational institution, which will operate during distance learning and will require adequate temperature regulation. Energy saving and enhancement of energy efficiency are priority areas of political activity in Ukraine as well as globally. These measures are crucial requirements for the European integration of the national energy system. Buildings deserve special attention in the field of energy saving because they account for more than a third of the world's energy consumption [1]. At the same time, during the evaluation and formulation of an energy-saving action plan, it is imperative to consider various parameters that characterise the building. In particular, these parameters include a set of operational factors. Such factors include the work schedule, indoor air temperature, duration, and frequency of occupancy, lighting operation, equipment usage, and more. Occupants differ in their requirements for comfort, which are also influenced by their behaviour. The efficient use of energy resources in buildings is influenced by operational and behavioural factors [2], [3].

Understanding occupant behaviour has been emphasised as an important factor in occupancy modelling to achieve energy efficiency improvements, especially in building heating, ventilation and air conditioning systems [4]. To this end, the authors of [4] conducted an experiment to monitor indoor environmental variables such as temperature, lighting, relative humidity, and CO_2 levels in the living room of a residential building. The residential building consists of five separate rooms, in Taman Teratai Johor, Malaysia, which has a tropical climate with typical temperatures ranging from 25 °C to 30 °C all year round. Five different occupancy prediction models were used to predict occupancy. According to this study, occupancy detection can reduce energy costs by up to 30 % while boosting indoor air quality. Educational institutions are interesting from an operational perspective, as they are characterised by intensive occupancy during regular classes [5], [6], which in turn largely affects the integral characteristics of heat gains into the premises and energy consumption depending on the level of awareness of potential consumers (whether the light is turned off, the faucet is closed towards the end, windows are opened / closed, etc.) [7]–[9].

1.2. Energy Performance of Educational Institutions during the Pandemic Period

Research [10] shows the effect of 15 architectural building design parameters (ABDPs) on energy consumption and students' thermal comfort for a single-storey education building at the University of Newcastle, Australia. Sensitivity and uncertainty analyses were used to assess the most important ABDPs. According to the authors' recommendation, these results can be useful for building designers, but they do not take into account the dynamics of operational factors.

A comprehensive effectiveness analysis of the deep retrofitting process of an educational building located in north-eastern Poland is presented [11]. Planned and actual energy effects were compared, as well as the associated reductions in pollutant emissions. The analysis of the reasons for the change in the final Heating Energy Indicator within four years after retrofitting did not take into account possible changes in the schedule of use of the building.

An overview of thermal comfort and indoor air quality (IAQ) of educational buildings closely related to ventilation energy consumption was conducted [12]. This paper critically reviewed the interaction of thermal comfort, IAQ and ventilation energy consumption at different educational levels under different climates. It was noted that more studies were required for investigating thermal comfort in educational buildings during the heating period. University buildings require increased attention. The number of publications concerning Central European countries is relatively limited, particularly regarding university premises where the level of ventilation control is comparatively low. The review overlooked the issues related to energy consumption during the dissipation and reduced use of premises, which are particularly prominent under quarantine conditions and the prevalent combination of in-person and online forms of classes during the war period in Ukraine.

The COVID-19 pandemic significantly affected the energy consumption of government institutions, including higher education establishments, due to the implementation of social distancing, ensuring adequate indoor ventilation, and personal hygiene measures [13].

Consequently, there are now stricter needs for maintaining high standards of in-door air quality in order to prevent airborne virus transmission [14]. The developed strategy for the optimal control of the HVAC system allows reducing energy consumption by an estimated 30 % for the case study of an educational building of the University of Pisa. Schedules of the building use are taken into account. It is acknowledged that addressing the issue of COVID-19 necessitates a higher ventilation rate to achieve improved air quality levels. Simultaneously, when analysing the challenge of balancing occupants' comfort with energy consumption in buildings, it is crucial to consider reduced schedules for use of premises under quarantine restrictions.

1.3. Educational Institutions in Ukraine during the Pandemic/Wartime Conditions

With the aim of increasing social distancing and limiting contact between people, a significant number of countries implemented partial or full transition to remote learning for educational institutions, commercial establishments, and industrial enterprises [15]. These measures resulted in significant changes in energy usage schedules and patterns [16]. At the beginning of the pandemic in Ukraine, most educational institutions at all levels of education also shifted to blended or remote working modes. This was determined by the epidemiological situation in the area where the educational institution was located. In 2023, when most countries worldwide had overcome the threat of COVID-19 spread and returned to in-person learning, Ukraine was facing a new challenge related to military threats. This situation requires the ongoing implementation of alternative learning methods to prioritize safety and protect the lives of students and educators. Under such circumstances, to avoid excessive use of energy and ensure the smooth operation of buildings, a very important issue arises – the establishment of schedules for the rational use of energy for heating needs, while considering the occupancy patterns of the premises. At the same time, the regulation of heating, ventilation, and air conditioning systems according to these schedules requires the availability of appropriate energy monitoring systems and the optimal configuration of equipment, which will ensure economic viability of such regulation. Currently, an increasing body of evidence suggests that the performance of a building is affected by the dynamics of occupant behaviour [17]. In particular, the results of a study by the World Business Council for Sustainable Development [18] estimate that inefficient user behaviour can contribute to a one-third increase in a building's energy consumption, whereas energy-saving behaviour can lead to a one-third reduction in energy costs.

Considerable attention in the study of energy consumption during the COVID-19 pandemic is devoted to the increase in consumption of electricity [12], [19], [20] and water [21] in residential buildings, provided that employees work from home. For Ukraine with a sharply continental climate, the issue of the use of heat energy is the most urgent, because its level can make up to 85 % of the total energy balance of the building [22]. Energy-efficient modes of heating energy use in buildings are associated with the use of intermittent modes of heating and ventilation [23]. In the article [24], a study of the natural level of air exchange in educational institutions of Ukraine was conducted. The obtained results are used to adjust the energy model of the building under study.

A thorough analysis of implementing short-term and energy-saving modes of operation for the heating and ventilation systems of educational premises not used during remote learning is relevant and aligns with the approaches outlined in the Law of Ukraine "On Energy Efficiency of Buildings" [25]. Furthermore, it serves to justify the viability and importance of implementing monitoring capabilities for energy and operational parameters in buildings, as a fundamental requirement to enable effective energy resource conservation in cases of excessive usage. The results of the study [17] represent the possibilities of using data from the energy monitoring system, using the example of a set of three residential buildings, including a total of 305 student apartments located at the main campus of the Royal Institute of Technology (KTH) in Stockholm. An additional analysis is required, which would take into account the schedules and distribution of the use of premises when determining energy consumption in the conditions of quarantine restrictions and martial law for Ukrainian universities. Such an analysis can deepen the understanding of the distribution of energy consumption and of how comfort can be ensured under changing conditions of use of educational institution buildings.

Pandemic restrictions in Europe and worldwide were somewhat eased in 2022, but due to the enforcement of martial law in Ukraine, the implementation of blended learning was not possible due to the constant threat of rocket attacks. Educational institutions continued to operate in a remote mode, and the requirements for educational institutions remained unchanged.

1.4. Objectives

The subject of this study is Building No. 17 of the Radio Engineering Faculty at Igor Sikorsky Kyiv Polytechnic Institute. The research focuses on the heating energy consumption patterns of the building during both remote and in-person learning modes.

The objectives of the study are as follows:

1. To create a dynamic model of the building using the DesignBuilder software environment, based on the investigated object.
2. To conduct simulations of the building's energy consumption patterns using three proposed scenarios: No. 1 – at a constant temperature and steady air exchange (indoor air temperature t = const, hourly infiltration rate n = const); No. 2 – with intermittent heating mode (lowering the temperature during non-working hours and weekends) and steady air exchange (t = var, n = const); No. 3 – with intermittent heating and intermittent air exchange (t = var, n = var).
3. To simulate the energy consumption of the building under quarantine, considering the schedules for using the premises and the permissible levels of temperature drop in them when implementing the three proposed scenarios (No. 1, No. 2, No. 3 – similarly).
4. To evaluate the indicators of building energy consumption in the case of implementing distance learning.

2. MATERIALS AND METHODS

Building Energy Modelling (BEM) involves predicting a building's energy consumption and its corresponding energy-saving level compared to a standard baseline. BEM approaches are implemented through software products, with EnergyPlus and TRNSYS being the most commonly used ones [26]. Unlike TRNSYS, which is a paid software product, EnergyPlus is more appealing for usage due to its free availability. EnergyPlus does not have its own graphical editor, so the building geometry is created using the DesignBuilder software environment, which is synchronized with EnergyPlus. The software allows for conducting energy simulations for the entire building or individual zones with a time step of 10 minutes. It includes defining the thermal properties of the building envelope, window constructions with optical glazing properties, engineering systems, energy sources, equipment operating schedules, lighting and temperature regimes, occupancy schedules, human activity, clothing insulation properties, and more. The software considers the inertial characteristics of the building envelope and systems, as well as the dynamics of climate data variability. The output provides information on air temperature, surface radiant temperature, loads on heating/cooling and ventilation (HVAC) systems, comfort levels, and more. EnergyPlus incorporates codes from DOE-2, ASHRAE, and BLAST, which are aligned with European standards, making it a viable choice for use [27].

The model takes into account heat transfer between building zones. The thermal balance of the building/zone is calculated dynamically with respect to the indoor air temperature, considering variable conditions at zone boundaries and heat gains inside the zone, zone air heat balance, internal and solar heat gains, and transmission links with adjacent zones and the external environment through zone boundaries (envelope). A detailed description of dynamic energy simulation is presented in EnergyPlus "Input Output Reference" [28].

In order to study the energy performance of the building, energy models of one of the educational buildings of Igor Sikorsky Kyiv Polytechnic Institute (Kyiv, Ukraine) were created based on the software product EnergyPlus [26]. 3-D model of the building geometry was created in the graphic editor DesignBuilder; thermal properties of the multi-layer enclosure, window structures with optical features of glazing, engineering systems, operation schedule and temperature regimes, etc. were specified [9]. The software product takes into account the inertial characteristics of the building envelope and systems, the dynamics of climatic data variability. At the output, the software product allows obtaining air temperature, surface radiation temperature, heating/cooling and ventilation system (HVAC-system) load, and others [22].

The results presented in this article are a continuation of the research presented in the article [9]. Below are the initial data of the research object used to create the building energy model.

Initial data. Building and model [9]: For creating a building model in the DesignBuilder software, educational building No. 17 of Igor Sikorsky Kyiv Polytechnic Institute was used. It was built in 1969. The building is located in Kyiv. Geometrically, the building is of a regular extended rectangular shape. The main part of the facades is oriented to the north and south. The building comprises five floors, as along with a heated basement and an unheated attic. The heating volume of the building is 42371 m^3, the area is 12185 m^2. All windows of the building were replaced with metal-plastic single-chamber double-glazed windows with air-filled chambers, with the exception of the technical floor, where glass blocks were installed. At the same time, the share of the area of translucent structures is 36.7, 12.0, 35.4 and 12.0 % in the northern, eastern, southern and western orientations, respectively. The bearing layer of the outer walls of the building is made of expanded clay concrete. For external walls U-Factor with Film – 1.02 W/m^2·K. Covering of the building – flat roof, rolled: U-Factor with Film – 0.80 W/m^2·K; one part of the coverage is the coverage of the 5th floor, another part is the coverage of the technical floor. Foundation – concrete blocks (floor U-Factor with Film – 0.75 W/m^2·K). Glass U-Factor for windows – 2.38 W/m^2·K. The building is supplied with heat through the networks of a centralized heating system, the model of which allows for the introduction of intermittent heating modes. The building has a water central heating system with regulation at the system's entrance. Zone temperature control for office spaces according to the occupancy schedule is achieved through electric heating. The building's heating system is two-pipe with shut-off valves. In addition, it is provided that the heating devices installed on the premises are M140 cast-iron radiators with thermostatic heads, which allow for adjustment by building zones. The ventilation system is natural – it is provided at the level of 0.7 ac/h by opening the windows and doors; another 0.3 ac/h is provided by the infiltration component (due to the looseness of the enclosed structures). Thus, the total air exchange is 1 ac/h, aligning with the standard requirement for educational buildings. The number of people in the building during normal operation is 2763.

The 3-D model of the educational building No. 17, created in the DesignBuilder software environment, is shown in Fig. 1.

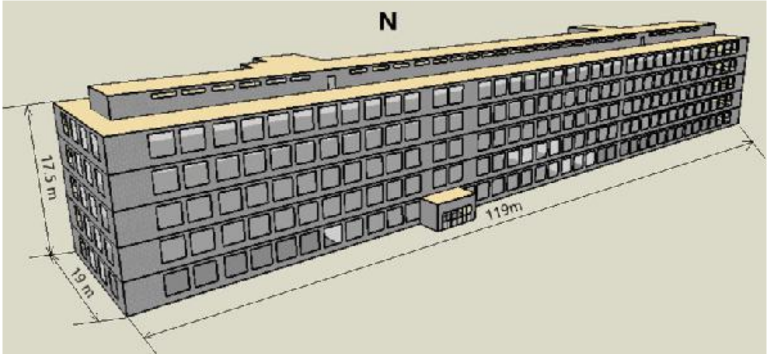

Fig. 1. 3-D-model of educational building No. 17 of Igor Sikorsky Kyiv Polytechnic Institute (N – North).

During the quarantine and especially during the period of martial law, the number of occupants and room occupancy schedules changed. Apart from remote learning, mixed forms of education were sometimes used, and safety conditions were maintained during air raids. Therefore, the model applied both the normal mode of operation and the quarantine mode, where only administrative and office spaces were utilized during remote learning. In the applied occupancy schedules, heat gains from occupants and office equipment were considered according to the standards [29], [30].

For the building model under normal operation mode (in-person learning period), rooms with similar functional purposes were merged into a single zone in the building model, including:

- Educational spaces (lecture halls, computer labs, methodological rooms, etc.);
- Common areas (corridors, restrooms);
- Utility rooms (basement, attic, vestibules).

Such merging is justified as the operational parameters of the combined zone (internal temperature, air exchange, occupancy per unit area) remain unchanged. However, during the period of distance learning, significant differences in operational parameters, as well as thermal and mass flows at the boundaries between the utilized and unutilized spaces, led to the addition of thermal zones for individual rooms in the model with designated parameters based on the simulated scenario. Figure 2 illustrates the zoning of a typical floor of the building.

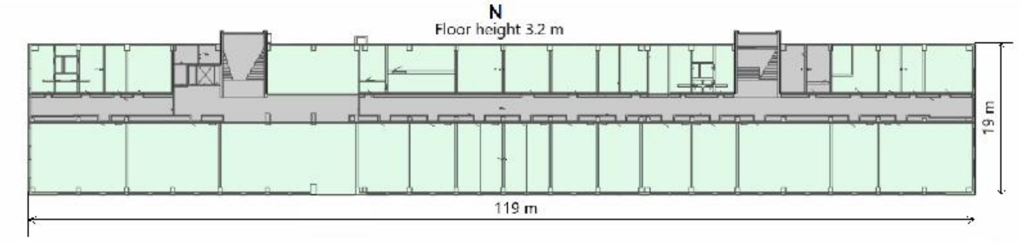

Fig. 2. Zoning of a building, using a typical floor as an example (N – North).

Initial data. Schedules of operation of the building and engineering systems. The hourly climate data used for the simulation is an IWEC hourly file for a typical year for Kyiv conditions [31]. The analysis of weather data, namely, the hourly variations in outdoor temperature and the amount of solar heat gains received by the room through window structures per unit of heated area of the room, is presented in [9]. Specific indicators of solar heat gains are determined taking into account the area and location of window structures using DesignBuilder on the basis of typical hourly data on the direct and diffuse component of solar radiation for the conditions of Kyiv, taken from IWEC.

For the normal operation mode of the premises, the number of occupants in the building was determined according to the requirements of standard [30], and for educational institutions, the average value of this parameter per building is 5 m^2/person. Before the pandemic, the total number of staff and students in the educational building corresponded to the specified number of individuals according to the requirements of regulatory documents. Under the conditions of the pandemic, the Ministry of Health of Ukraine demanded compliance with the requirements of not less than 4 m^2/person for the yellow level of danger [32], which corresponded to the accepted normative number of people for normal working conditions. For the pandemic mode, the occupancy density in administrative premises remained unchanged compared to the normal working mode. However, since the educational process was switched to remote mode, the model assumed the absence of people in classrooms and laboratories. For the simulated operating modes of the investigated building, the occupancy density throughout the day was set according to the schedule presented in Table 1.

Table 1. Occupancy Profile during Working Days

Time	Normal mode	Quarantine mode
	Educational and administrative premises	Administrative premises
	Load (%)	
7:00–8:00	25	
8:00–9:00	50	
9:00–12:00	100	
12:00–14:00	75	
14:00–17:00	100	
17:00–18:00	50	
18:00–19:00	25	
19:00–7:00	0	

Visitors are absent in educational premises for quarantine mode and in all premises on weekends, public holidays, vacations for all time.

In DesignBuilder, metabolism is considered a constant value, representing the amount of heat generated by an average adult with a typical body surface area of 1.8 m^2. The model of the investigated building assumes an equal number of men and women, so the metabolic factor is set at 0.9, which corresponds to 0.85 for women and 1.0 for men. The metabolic rate M and the thermal insulation of clothing I_{clo} are adopted at the level of typical office work, which is 140 W (taking into account the metabolic factor – 126 W) and 1, respectively.

Artificial lighting was set at a level of 300 lux on the work surface, and the lighting system's power consumption was 2.1 W/m^2. On weekends, holidays, and vacations, artificial lighting was not used. The power consumption of office equipment was 4.74 W/m^2, and its usage schedule coincided with the visitors' activity schedule in the building.

A 3D model of the building was created in the DesignBuilder software, taking into account the efficiency of the building engineering systems. The calculation of the building energy characteristics was carried out using the detailed method, which allows considering the efficiency of engineering systems. EnergyPlus software allows taking into account the thermal inertia of the building envelope. In the adopted calculation scheme, the inertia of the engineering systems was not considered, resulting in losses in the systems amounting to 15 %.

Several scenarios were developed for the investigated building model: for normal building operation mode (in-person learning) and partial utilization of the building premises (remote learning): Scenario No. 1 provided for maintaining the temperature and air exchange at stable values throughout the entire time; when implementing Scenario No. 2 – during non-working hours and weekends the temperature was lowered to 17 °C; under Scenario No. 3 – temperature was decreased to 17°C during non-working hours and weekends and the standard air exchange was decreased to the level of 0.3 ac/h during non-working hours and weekends (during non-working hours, the windows were not open and only the infiltration component remained). Detailed parameters of the proposed modes and premise schedules are given in Table 2.

Table 2. Parameters of the Proposed Modes

Scenario No.	Normal mode of operation	Quarantine mode	
		Used premises (separate premises and toilets on the 1st and 2nd floors)	All other unused premises
1	t = 20 °C [24 hours & 7 days] n = 1 ac/h [24 hours & 7 days]		t = 14 °C 24 hours & 7 days n = 0.3 ac/h 24 hours & 7 days
2	$t_{heating}$ = 20 °C [from 7:00 until 18:00] $t_{heating\ set\ back}$=17°C [the rest of the working hours + weekends]		
3	$t_{heating}$ = 20 °C [from 7:00 until 18:00] $t_{heating\ set\ back}$=17°C [the rest of the working hours + weekends] n = 1 ac/h [from 7:00 until 18:00] n = 0.3 ac/h [the rest of the working hours + weekends]		

* Air exchange (ac/h); t: Given indoor air temperature without the regulation (°C); $t_{heating}$: During working hours in premises occupied by people (°C), $t_{heating\ set\ back}$: When it is lowered during non-working hours (°C)

3. RESULTS

Output parameters. Based on the input data presented in Section 2, a series of energy dynamic simulations were conducted for different modes of operation of engineering systems and building operation schedules. The results yielded hourly data, including thermal heating loads, indoor air temperatures, and mean radiant temperatures within the premises. Additionally, annual heating energy demand data were obtained for a subsequent analysis.

Below are the first results of the research on the impact of heating and ventilation system operations in educational institutions on energy consumption during the period of military state and pandemic for the conditions of Ukraine.

The calculation of the basic level of energy consumption was carried out in accordance with the comfort parameters outlined in the standards of Ukraine [29], [30], [33], [34], taking into account the typical climatic conditions for Kyiv. It is worth noting that since 2016, Ukraine has fully transitioned to European and international standards for assessing the energy efficiency of buildings. The temperature regulations for different types of buildings are uniformly specified both in modern Ukrainian standards and in the EN series standards. However, there are differences in the requirements for air exchange in the standards of various EU countries and Ukraine.

It is worth noting that during the pandemic, specific requirements are imposed on the level of air exchange. In the case of adaptive mechanical ventilation systems, it is recommended to reduce the CO_2 level almost by half and maintain it at 400 ppm, whereas in normal conditions, this parameter should not exceed 1000 ppm, depending on the building purpose [24]. In the context of the pandemic, ensuring an increase in air quality/air exchange requirements is challenging for the majority of educational institutions in Ukraine due to limitations in the existing engineering systems. This is one of the reasons for the transition to distance learning. In office and administrative premises, the distance between occupants and the level of air exchange (occupant density, lighting density, device heat density, and schedule) are assumed to be the same for normal and quarantine conditions. A possible reduction in occupant density does not significantly affect energy consumption for maintaining comfort conditions in working areas.

The primary measure to limit the spread of the COVID-19 virus was to transfer students to distance learning. After the full-scale military invasion and the introduction of martial law in Ukraine, the Ukrainian educational institutions (particularly in northern, southern, and eastern regions) continued to operate in a remote mode.

The created 3-D energy model of the educational building at Igor Sikorsky Kyiv Polytechnic Institute was validated using actual energy consumption data, considering the real indoor air temperature, room occupancy schedules, equipment usage, etc., under normal operating conditions before the implementation of quarantine restrictions. The difference between the actual energy consumption recorded by the heat energy meter and the energy model of the building in the EnergyPlus software environment is approximately 10 %. Additionally, a comparison was made between the results of energy modelling of the building heating requirements using the quasi-stationary method DSTU B A.2.2-12:2015 [30], a national calculation method for establishing the baseline energy consumption and assessing the energy efficiency level of buildings, and the dynamic energy model of the building created in the EnergyPlus software environment, showing a discrepancy of about 18 %.

Total area of used premises for normal and quarantine mode is presented in Table 2. Tables 3 and 4 present the results of building energy consumption modelling. The first number in the designation shows the mode of operation X/X: 1/X – normal mode, 2/X – quarantine; the second number corresponds to the scenario number (for example, X/3 is Scenario No. 3). Similar designations will be maintained here and below. For example: "1/1" – normal mode, with stable temperature and air exchange values throughout the entire time; "2/1" – quarantine mode, with stable temperature and air exchange values throughout the entire time. Different temperature levels are maintained for the used and unused rooms. "Δ%" – the percentage deviation of energy consumption in the quarantine mode compared to the normal mode under a given scenario.

Table 3. Need for Heating by the Created Models

1	Mode / scenario, X/X	1/1	2/1	Δ (%)
2	Heating area of the building (m^2)	12184.8		-
3	Area of used premises (m^2)	12184.8	992.1	-91.9
4	The need for heating, used premises (kWh/season)	-	219483.0	-
5	Energy consumption for the heating season (kWh/season)	1596335.8	617532.9	-61.3
6	Specific energy consumption (kWh/m^2)	131.0	50.7	-61.3
7	Specific energy consumption of used premises (kWh/m^2)		221.2	68.9
8	Specific energy consumption of the used representative premises, north orientation (kWh/m^2)	131.9	241.7	83.2
9	Specific energy consumption of the used representative premises, south orientation (kWh/m^2)	115.1	215.1	86.8
Δ: Deviation of calculation results 2/1 from 1/1 (%).				

Table 4. Heat Consumption by the Created Models

1	Mode / scenario, X/X	1/2	2/2	Δ (%)
2	Heating area of the building (m^2)	12184.8	12184.8	-
3	Area of used premises (m^2)	12184.8	992.1	-91.9
4	The need for heating, used premises (kWh/season)	-	169745.7	-
5	Energy consumption for the heating season (kWh/season)	1363925.1	592826.0	-56.5
6	Specific energy consumption (kWh/m^2)	111.9	48.7	-56.5
7	Specific energy consumption of used premises (kWh/m^2)		171.1	52.9
8	Specific energy consumption of the used representative premises, north orientation (kWh/m^2)	110.8	185.2	67.1
9	Specific energy consumption of the used representative premises, south orientation (kWh/m^2)	94.4	162.0	71.6
Δ: Deviation of calculation results 2/2 from 1/2 (%)				

In addition to the aforementioned information, the comparison of heat consumption is presented in Table 5.

Table 5. Heat Consumption by the Created Models

1	Mode / scenario, X/X	1/3	2/3	Δ (%)
2	Heating area of the building (m^2)	12184.8	12184.8	-
3	Area of used premises (m^2)	12184.8	992.1	-91.9
4	The need for heating, used premises (kWh/season)	-	120678.3	-
5	Energy consumption for the heating season (kWh/season)	829736.1	546852.8	-34.1
6	Specific energy consumption (kWh/m^2)	68.1	44.9	-34.1
7	Specific energy consumption of used premises (kWh/m^2)		121.6	78.6
8	Specific energy consumption of the used representative premises, north orientation (kWh/m^2)	66.9	134.3	100.8
9	Specific energy consumption of the used representative premises, south orientation (kWh/m^2)	53.0	112.2	111.6
Δ: Deviation of calculation results 2/3 from 1/3 (%)				

Therefore, according to the modelling results for Scenario No. 1, partial utilization of the building during remote learning will reduce heating energy consumption by 61.3 % [9], No. 2 – 56 %, No. 3 – 34 % in quarantine mode. At the same time, the specific consumption to the total heating area is reduced by the equivalent value. However, if we compare the specific consumption of heat energy in heated rooms to the appropriate level, this value increases by 68.9 % compared to the usual mode. If we consider a single room, which is zonally separated in both models for analysis, its specific consumption increased by 83.2 % and 86.9 % for the northern and southern orientation compared to the usual mode, respectively. Similar observations can be made for scenarios No. 2 and No. 3. If we compare Scenario No. 1 and Scenario No. 2, we see that the use of intermittent heating mode reduces energy consumption both in normal operation (by 14.6 %) and in quarantine (by 4 %, savings are reduced due to the flow to adjacent premises). The reduction in heat energy consumption during quarantine is not particularly significant since only a small part of the premises is operational. Consequently, there will be a decrease in temperature during non-working hours. Scenario No. 3 is the most energy efficient as evidenced by the obtained results. Energy savings, compared to Scenario No. 2 for the normal mode, are 39.2 % and for the quarantine – 7.8 %. Thus, the total energy savings for scenarios No. 1 and No. 3 for normal/steady state are 48 % and for quarantine – 11.5 % [9]. The hourly heating load for in-person (normal) and remote learning conditions is shown in Fig. 3. The illustration of the heating load on the heating system for Scenario No. 1 is presented in the paper [9]. It follows from Figs. 4 and 5 that when the proposed operating modes are implemented under quarantine restrictions, the load on the heating system is generally reduced, and Scenario No. 3 is the most energy efficient for both operating modes.

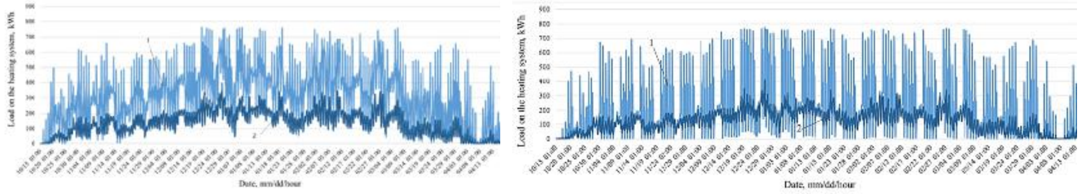

a)

b)

Fig. 3. Hourly need for heating by the building.
(a – Scenario No. 2; b – Scenario No. 3;
1 – normal mode; 2 – quarantine mode).

However, as noted, the specific energy consumption per unit of heating area (up to the appropriate temperature level) has increased. Figure 3 shows the graphical hourly specific consumption of heat energy for the heating of a separate room, which is operated under quarantine and normal conditions. To compare the consumption of heat energy at different orientations, the azimuth of the building model was rotated in the program by 180° (the results obtained are given in Table 2) and one room was considered for two cases. The room under consideration has an area of 37.4 m^2 and two windows (5.4 m^2), the glazing factor is 0.52. The increase in specific consumption indicates that in rooms where the proper temperature is maintained during working hours, the heat flow intensifies through the inner walls to neighbouring rooms, where the level of heating is reduced. The southern orientation is characterised by more frequent shutdowns / reductions in the load on the heating system compared to the northern orientation, due to the intensity of solar revenues.

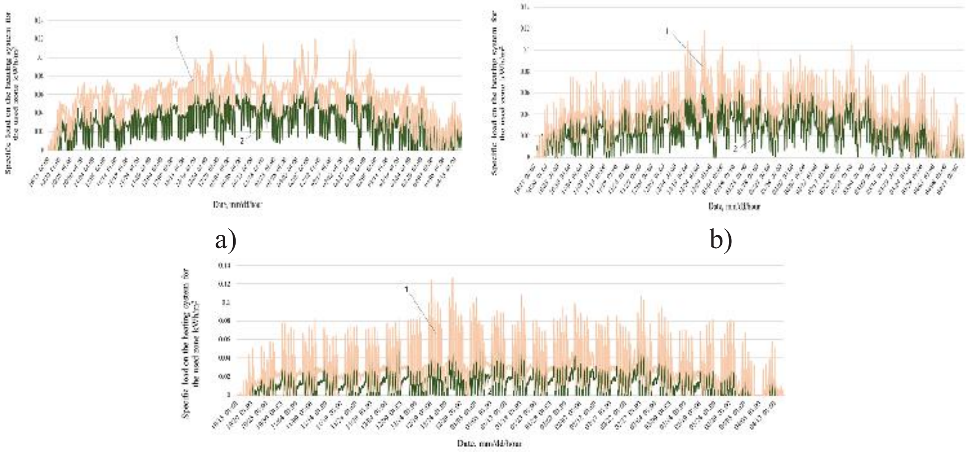

a)

b)

c)

Fig. 4. Hourly heat consumption by representative premises of north orientation. (a – Scenario No. 1; b – Scenario No. 2; c – Scenario No. 3; 1 – quarantine mode; 2 – normal mode).

Figure 5 shows hourly graphs of air temperature fluctuations, average radiation temperature and air exchange during normal operation and quarantine in the considered representative room of northern orientation.

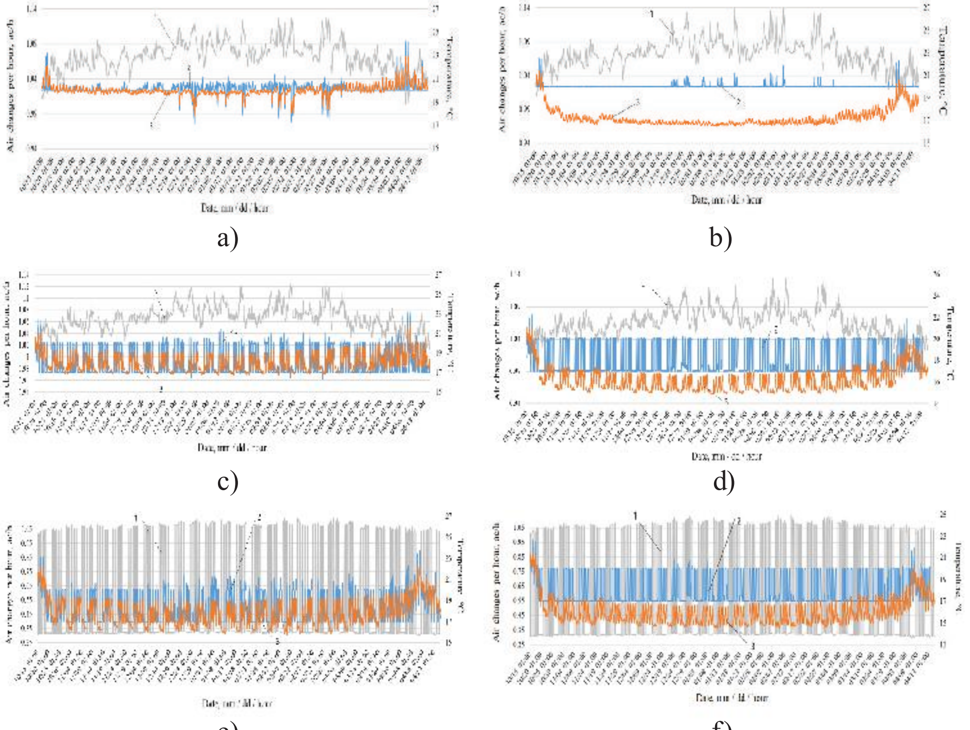

a)

b)

c)

d)

e)

f)

Fig. 5. Fluctuation of air temperature, average radiation temperature, air exchange level during the heating period for representative premises of north orientation. (a – 1/1; b – 2/1; c – 1/2; d – 2/2; e – 1/3; f – 2/3; where: 1/X – normal mode, 2/X – quarantine mode, X/1 – Scenario No. 1; X/2 – Scenario No. 2; X/3 – Scenario No. 3; 1 – air exchange; 2 – deviation of indoor air temperature; 3 – deviation of the average radiation temperature).

The same analysis was carried out for the south orientation. The general trend for south orientation is similar, but the values of indoor temperature and mean radiation temperature are higher. The average difference between the room temperature and the average radiation temperature for the calculation period are presented in Table 6, where X/X_S – south and X/X_N – north orientation.

Table 6. Indoor Air Temperature and Average Radiation Temperature for the Obtained Models

Scenario	t_{air_in} (°C)	t_{mean_rad} (°C)	Δ(°C)	Scenario	t_{air_in} (°C)	t_{mean_rad} (°C)	Δ(°C)
1/1_S	20.1	20.0	0.1	2/2_S	18.1	16.7	1.4
1/1_N	20.3	20.6	-0.3	2/2_N	18.2	16.9	1.3
2/1_S	20.1	17.3	2.8	1/3_S	18.3	17.9	0.4
2/1_N	20.2	17.9	2.3	1/3_N	18.6	18.6	0.0
1/2_S	18.1	18.1	0.0	2/3_S	18.1	16.0	2.1
1/2_N	18.3	18.7	-0.4	2/3_N	18.3	16.8	1.5

* North orientation, S: South, tair_in: Indoor air temperature, (°C), tmean_rad:
Average radiant temperature (°C), Δ: Temperature difference between tair_in and tmean_rad (°C)

From the given results, it follows that the parameters of comfort in the premises used under quarantine restrictions are deteriorating (the average radiation temperature decreases).

This is caused by the contact of these spaces with cold zones, where the temperature is tair_in= 14 °C. Due to the existence of internal heat flows between these zones, there is a reduction in the average radiant temperature (tmean_rad) in the occupied spaces. For Scenario No. 1, the lowest average radiation temperature is typical of the northern orientation room used in quarantine. The highest average radiation temperature – for the southern orientation in normal operation (in this case, the average radiation temperature even exceeds the air temperature by 0.3 °C). A characteristic feature of south-facing rooms, in addition to the general increase in average radiation temperature, is the increase in the amplitude of fluctuations in both average radiation temperature and indoor air temperature during the day and night, due to additional heat from the sun on the south side. Similar analogies are observed for scenarios No. 2 and No. 3. For Scenario No. 2, there is a decrease in the average radiant temperature and indoor air temperature during the heating period. Additionally, the difference between the indoor and average radiant temperatures is also reduced. Scenario No. 3 compared to No. 2 is characterised by an increase in indoor air temperature, as the air exchange in the premises during non-working hours decreases. However, this slightly reduces the average radiation temperature. As a result, in the implementation of Scenario No. 3, the moisture in the air condenses to a greater extent than in No. 2 and diffuses into the enclosing structures, removing heat from them and, as a result, reducing the average radiation temperature. However, the reduction is very small compared to the savings of heat energy in Scenario No. 3, so the most appropriate scenario to be used for both modes of operation is Scenario No. 3.

4. DISCUSSION

The conditions of the COVID-19 pandemic have led to a significant transformation of teaching methods adopted in higher educational institutions, shifting towards a reliance on online learning systems. Considerable attention from researchers has been directed towards studying electricity consumption issues [35]–[37]. Overall, the analysis shows that the total electricity consumption in 2020 was significantly lower for educational institutions compared to 2019 [35], [36]. For instance, in the buildings of the University of Jordan campus, electricity consumption decreased by 20.8 % [36]. Similar studies on electricity consumption reduction have been conducted for universities in Michoacan, Mexico [35]. The article [37] explores how the COVID-19 pandemic has affected the demand and changes in electricity consumption in the energy system of the USA. However, the issue of thermal energy consumption for heating needs in educational institutions during the pandemic period has not been studied sufficiently.

The article [38] presents results regarding the increased energy consumption for heating and cooling purposes in residential buildings of the sleeping districts in Geneva, Switzerland. The obtained results indicate that the energy demand for heating and cooling of the premises tended to increase by 8 % and 17 %, respectively, during partial lockdown, while these figures grew to 13 % and 28 % in the case of a full lockdown. In the present article, the assessment of the change in energy consumption for heating in university buildings has been conducted for the conditions of Kyiv, Ukraine, for the first time.

During the pandemic and periods of martial law, a decrease of classes and classrooms has been observed in educational institutions of Ukraine and, consequently, a decrease in the number and area of rooms in which the comfort conditions necessary for classes are maintained. For the academic building of the university, the total energy consumption for heating needs depends on the number of rooms that are actively used and the heating and ventilation control modes. Simulation of dynamic modelling was conducted to analyse the energy consumption of the educational building, specifically focusing on heating requirements. The simulation was performed using the educational building of Igor Sikorsky Kyiv Polytechnic Institute as a representative example.

The conducted studies consider the unique characteristics of energy processes within the multi-component structure of the building, specifically when determining energy consumption for heating purposes. These characteristics include the influence of the dynamics of solar heat gains, the building orientation in relation to cardinal directions, heat accumulation and internal heat flow. Special attention is dedicated to investigating the impact of various modes of operation of the heating and ventilation system.

The article presents data on the impact of decentralization and occupancy schedules of the utilised premises on energy consumption reduction. The results were obtained using dynamic modelling of a multi-zone three-dimensional model of energy processes in the building. The magnitude of potential savings for different scenarios and the justification for the placement of the occupied premises were the main objectives of this study.

If we consider the utilization of the

building according to Scenario No. 1, the reduction of the utilized areas during the quarantine mode by 92 % (Table 3) leads to an 83 % decrease in energy consumption for heating in simplified proportional estimations without considering interzone airflows based on average outside temperatures during the heating period. In Table 4, we observe a 61 % decrease, meaning that the percentage reduction in the utilization of building spaces does not lead to a proportionate decrease in energy consumption due to inter-zone heat flows between neighbouring spaces.

During dynamic simulations, the reduction in energy consumption relative to the base calculation for normal building operation (mode 1, Scenario No. 1) is as follows:

1) In the case of implementing pandemic-specific mode 2/1 (with constant temperature levels throughout the day for working spaces not in use) – 61.3 %; 2/2 (with intermittent operation modes for heating systems) – 62.7 %; 2/3 (intermittent heating and ventilation modes) – 65.7 %;

2) for normal operating mode, with the implementation of intermittent heating system operation 1/2 – 14.6 %, and with intermittent heating and ventilation operation 1/3 – 48 %.

The articles [22], [38], [39] present potential energy savings when implementing temperature level regulation throughout the day for residential [38]–[40] and administrative buildings [22], but not for conditions of martial law and pandemic. In [22], it is indicated that implementing a reduction of indoor air temperature by 3 °C from the set level allows for a 18 % reduction in thermal energy consumption. Introducing variable temperature regimes in residential buildings [38] can lead to a 16 % reduction in thermal energy consumption. The implementation of variable operation modes for ventilation systems and temperature regimes in residential buildings [39] can reduce heating energy demand by 25 % compared to a model with constant air exchange. It is worth noting that the obtained results in [22], [38] correspond to different usage patterns of residential building spaces, which significantly differ from the occupancy schedules of educational institutions. The effects of heat transfer between zones were not investigated in the results of [22], [39], as the temperature regime was uniform across all building zones. This underscores the necessity of conducting studies that allow for the assessment of thermal transfer between building zones under different temperature schedules and variations in the conditions of use for different spaces.

The increase in the specific consumption of heat energy by the premises used during quarantine is attributed to their proximity to colder zones. This proximity also results in a decrease in the average radiation temperature, impacting the comfort parameters, particularly for premises with a northern orientation. This observation is supported by the collected hourly data on fluctuations in air temperature, average radiation temperature, and their overall averages throughout the heating season.

The conducted research indicates that the difference between indoor air temperature and average radiant temperature can reach up to 14 %, depending on the orientation of the spaces and the temperature regimes in the considered and adjacent rooms. Temperature studies conducted for educational institutions in Ukraine show that the difference between indoor air temperature and average radiant temperature can reach up to 21 % [41].

Therefore, when choosing separate working areas during quarantine, preference should be given to south-facing rooms. Based on the analysis of various parameters, it can be concluded that Scenario No. 3 represents the most energy saving mode. The disadvantage of this mode is a decrease in the intensity of mass transfer processes as a result of a decrease in the level of air exchange. This leads to moisture retention on the enclosing structures, which leads to a decrease in the average radiation temperature compared to Scenario No. 2. However, this decrease is very small and imperceptible for the human body. Therefore, this mode can be recommended for implementation in quarantine / martial law mode and normal mode.

Therefore, it is demonstrated that the spatial arrangement of the premises and different modes of their use need to be taken into account when determining energy consumption for heating in each specific case. In order to address these challenges, the use of multi-zone dynamic energy models for buildings is recommended.

5. CONCLUSIONS

A dynamic model of a typical educational building for the conditions of Ukraine of Igor Sikorsky Kyiv Polytechnic Institute with centralized heating and natural ventilation was chosen as the object of research. Dynamic modelling of the energy state of the building was performed using EnergyPlus software, which takes into account the improvement of heating and air exchange modes.

The paper presents the first results of research on the impact of the peculiarities of heating and ventilation systems operation in educational institutions on energy consumption during the period of military state and pandemic conditions in Ukraine.

The main results of the research include the following:

1. Modelling of thermal energy consumption by the building under normal operation conditions (in-person learning) was performed for three developed scenarios: No. 1 – modelling of the operation of engineering systems at preset constant temperature and steady air exchange (indoor air temperature 20 °C, hourly infiltration rate 1 ac/h, t = const, n = const); No. 2 – with intermittent heating mode (lowering the temperature during non-working hours and weekends to 17 °C) and steady air exchange (t = var, n = const); No. 3 – with intermittent heating and intermittent air exchange (during non-working hours and weekends lowering the temperature to 14 °C and hourly infiltration rate to 0.3 ac/h, t = var, n = var). For the premises under quarantine mode that are utilized (distributed, 12 % of the total area), the same scenarios were employed. For unused premises t = 14 °C and n = 0.3 ac/h, t = const, n = const. According to the results of modelling of the three proposed modes of operation for the heating system and natural ventilation, the most substantial influence on reducing energy consumption for heating is attributed primarily to the reduction of air exchange rate and temperature in the unutilized premises during quarantine periods (for scenarios No. 1, No. 2, and No. 3, these values are 61.3 %, 62.7 %, and 65.7 %, respectively). It has been determined that the most energy saving result corresponds to Scenario No. 3. The total energy savings between scenarios No. 1 and No. 3 for the normal mode are 48 % and

for quarantine – 11.5 %. The analysis reveals that the efficiency of regulation modes during the quarantine period can decrease by more than four times compared to the normal mode. This decrease is primarily attributed to a reduction in the number of actively utilised rooms subject to control, as well as internal heat exchange with unoccupied spaces.

2. It has been determined that in the case of partial use of the building during quarantine, with the implementation of zone regulation, the total energy consumption of the building decreases by 61.3 %, 56.5 %, and 34 % for scenarios No. 1, No. 2, and No. 3, respectively. When the building is partially used under distance learning conditions, the specific thermal energy consumption for heating per unit of heated area increases compared to the conditions of in-person learning (normal mode). Specifically, for scenarios No. 1, No. 2, and No. 3, the increase is by 68.9, 52.9, and 78.6 %, respectively. Additionally, when considering a separate research room with north and south orientations, the difference in specific consumption is more prominent in the southern orientation (+86.8 %) compared to the northern orientation (+83.2 %), primarily due to uneven heat distribution from the sun. If it is possible to change the choice of premises used, it is advisable to try to place them next to each other and on the south side to reduce energy consumption for heating.
3. The introduction of intermittent heating allows reducing energy consumption in normal mode of operation by 14.6 %, in quarantine – by 4 % (internal heat flows between warm and cold zones of the building result in a decrease of the average radiant temperature in the occupied rooms and reduce the expected thermal energy savings). The introduction of intermittent ventilation allows increasing energy savings by 39.2 % for normal operation and by 7.8 % for quarantine / martial law. Thus, the total energy savings from the introduction of intermittent heating and ventilation for the normal mode is 48 % and for quarantine – 11.5 %. When considering the permissible typical control values, the reduction of preset indoor air temperature and ventilation has a greater impact on heating energy consumption. Decreasing the air exchange rate, both under normal operating conditions and during partial occupancy, has a greater impact on heating energy consumption for both normal and partial use conditions.

The modelling results provide a basis for determining the efficiency and feasibility of implementing zonal heating regulation in the university building under Ukrainian conditions. It is recommended to employ the suggested approaches to reduce energy consumption when planning schedules for the use of educational facilities with partial loading outside the pandemic period or martial law. This can be the subject of further studies.

Research limitation. The article conducts modelling of the energy characteristics of buildings aimed at maintaining the indoor air temperature at a specified level without considering comfort parameters, which can be assessed using the Predicted Mean Vote method (PMV). To ensure comfort within the premises during partial operation under quarantine restrictions, it is advisable to investigate the impact of increasing the air temperature in the operated premises to a level that aligns with the PMV comfort parameter within the acceptable range of ±0.5.

ACKNOWLEDGEMENTS

This research has been funded with support of European Regional Development Fund project "Optimal Control of Indoor Air Quality and Thermal Comfort Based on Room Real-time 3D Motion Scanning Data", Grant Agreement No 1.1.1.1/21/A/010.20:23

REFERENCES

1. Yoshino, H., Hong, T., & Nord, N. (2017). IEA EBC Annex 53: Total Energy Use in Buildings—Analysis and Evaluation Methods. *Energy Build*, 152. DOI: 10.1016/j.enbuild.2017.07.038.
2. Deshko, V., Bilous, I., Buyak, N., & Shevchenko, O. (2020). The impact of energy-efficient heating modes on human body exergy consumption in public buildings. In *ESS 2020 – Proceedings*. 12–14 May 2020, Kyiv, Ukraine. DOI: 10.1109/ESS50319.2020.9160270.
3. Upitis, M., Amolina, I., Geipele, I., & Zeltins, N. (2020). Measures to Achieve the Energy Efficiency Improvement Targets in the Multi-Apartment Residential Sector. *Latvian Journal of Physics and Technical Sciences*, *57* (6), 41–52. DOI: 10.2478/lpts-2020-0032.
4. Aliero, M. S., Pasha, M. F., Smith, D. T., Ghani, I., Asif, M., Jeong, S. R., & Samuel, M. (2022). Non-Intrusive Room Occupancy Prediction Performance Analysis Using Different Machine Learning Techniques. *Energies (Basel)*, *15* (23), 9231. DOI: 10.3390/en15239231.
5. Saraiva, T. S., de Almeida, M., Bragança, L., & Barbosa, M. T. (2018). Environmental Comfort Indicators for School Buildings in Sustainability Assessment Tools. *Sustainability (Switzerland)*, *10* (6), 1849. DOI: 10.3390/su10061849.
6. Katić, D., Krstić, H., & Marenjak, S. (2021). Energy Performance of School Buildings by Construction Periods in Federation of Bosnia and Herzegovina. *Buildings*, *11* (2), 42. DOI: 10.3390/buildings11020042.
7. He, Z., Hong, T., & Chou, S. K. (2021). A Framework for Estimating the Energy-Saving Potential of Occupant Behaviour Improvement. *Appl. Energy*, *287* (1), 116591. DOI: 10.1016/j.apenergy.2021.116591.
8. Laaroussi, Y., Bahrar, M. Elmankibi, M., Draoui, A., & Si-Larbi, A. (2019). Occupant behaviour: A major issue for building energy performance. In *IOP Conference Series: Materials Science and Engineering*, *609*, 072050. DOI: 10.1088/1757-899X/609/7/072050.
9. Deshko, V., Bilous, I., & Boiko, T. (2022). Influence of Heating and Ventilation Modes on the Energy Consumption of University Educational Buildings under Quarantine Conditions in Ukraine. *Journal of New Technologies in Environmental Science*, *6* (1), 36–40.
10. Alghamdi, S., Tang, W., Kanjanabootra, S., & Alterman, D. (2022). Effect of Architectural Building Design Parameters on Thermal Comfort and Energy Consumption in Higher Education Buildings. *Buildings*, *12* (3), 329. DOI: 10.3390/buildings12030329.
11. Sadowska, B., Piotrowska-Woroniak, J., Woroniak, G., & Sarosiek, W. (2022). Energy and Economic Efficiency of the Thermomodernization of an Educational Building and Reduction of Pollutant Emissions—A Case Study. *Energies (Basel)*, *15* (8), 2886. DOI: 10.3390/en15082886.
12. Jia, L. R., Han, J., Chen, X., Li, Q. Y., Lee, C. C., & Fung, Y. H. (2021). Interaction between Thermal Comfort, Indoor Air Quality and Ventilation Energy Consumption of Educational Buildings: A Comprehensive Review. *Buildings*, *11* (12), 591. DOI: 10.3390/buildings11120591.

13. Sun, C., & Zhai, Z. (2020). The Efficacy of Social Distance and Ventilation Effectiveness in Preventing COVID-19 Transmission. *Sustain Cities Soc.*, *62*. doi: 10.1016/j.scs.2020.102390.
14. Franco, A., Bartoli, C., Conti, P., Miserocchi, L., & Testi, D. (2021). Multi-Objective Optimization of HVAC Operation for Balancing Energy Use and Occupant Comfort in Educational Buildings. *Energies (Basel)*, *14* (10), 2847. DOI: 10.3390/en14102847.
15. Ivanko, D., Ding, Y., & Nord, N. (2021). Analysis of Heat Use Profiles in Norwegian Educational Institutions in Conditions of COVID-Lockdown. *Journal of Building Engineering*, 43. DOI: 10.1016/j.jobe.2021.102576.
16. Bahmanyar, A., Estebsari, A., & Ernst, D. (2020). The Impact of Different COVID-19 Containment Measures on Electricity Consumption in Europe. *Energy Res Soc Sci*, *68*, 101683. DOI: 10.1016/j.erss.2020.101683.
17. Rolando, D., Pallard, W. M., & Molinari, M. (2022). Long-Term Evaluation of Comfort, Indoor Air Quality and Energy Performance in Buildings: The Case of the KTH Live-In Lab Testbeds. *Energies (Basel)*, *15* (14), 4955. DOI: 10.3390/en15144955.
18. World Business Council for Sustainable Development. (2019). *Transforming the Market: Energy Efficiency in Buildings*. Survey Report. Geneva.
19. Chattopadhyay, K., Garg, V., Paruchuri, P., Mathur, J., & Valluri, S. (2022). Impact of COVID-19 on Energy Consumption in a Residential Complex in Hyderabad, India. *Energy Informatics*, *5*. DOI: 10.1186/s42162-022-00240-5.
20. Todeschi, V., Javanroodi, K., Castello, R., Mohajeri, N., Mutani, G., & Scartezzini, J. L. (2022). Impact of the COVID-19 Pandemic on the Energy Performance of Residential Neighborhoods and their Occupancy Behaviour. *Sustain Cities Soc.*, *82*. DOI: 10.1016/j.scs.2022.103896.
21. Tleuken, A., Tokazhanov, G., Serikbay, A.-B., Zhalgasbayev, K., Guney, M., Turkyilmaz, A., & Karaca, F. (2021). Household Water and Energy Consumption Changes during COVID-19 Pandemic Lockdowns: Cases of the Kazakhstani Cities of Almaty, Shymkent, and Atyrau. *Buildings*, *11* (12), 663. DOI: 10.3390/buildings11120663.
22. Deshko, V., Bilous, I., Sukhodub, I., & Yatsenko, O. (2021). Evaluation of Energy Use for Heating in Residential Building under the Influence of Air Exchange Modes. *Journal of Building Engineering*, *42*. DOI: 10.1016/j.jobe.2021.103020.
23. Deshko, V., Bilous, I., Biriukov, D., & Yatsenko, O. (2021). Transient Energy Models of Housing Facilities Operation. *Rocznik Ochrona Srodowiska*, *23*. DOI: 10.54740/ros.2021.038.
24. Deshko, V., Bilous, I., Vynogradov-Saltykov, V., Shovkaliuk, M., & Hetmanchuk, H. (2020). Integrated Approaches to Determination of CO2 Concentration and Air Rate Exchange in Educational Institution. *Rocznik Ochrona Srodowiska*, *22* (1), 82–104.
25. Verhovna Rada of Ukraine. (2017). *Law of Ukraine On Energy Efficiency of Buildings*. The Official Bulletin of the Verkhovna Rada, 33, Article 359. Available at https://zakon.rada.gov.ua/laws/show/2118-19?lang=en#Text.
26. Hong, T., Chen, Y., Belafi, Z., & D'Oca, S. (2018). Occupant Behavior Models: A Critical Review of Implementation and representation approaches in Building Performance Simulation Programs. *Building Simulation*, *11* (1). DOI: 10.1007/s12273-017-0396-6.
27. Crawley, D. B., Lawrie, L. K., Winkelmann, F. C., Buhl, W. F., Huang, Y. J., Pedersen, C. O., … & Glazer, J. (2001). EnergyPlus: Creating a New-Generation Building Energy Simulation Program. *Energy Build*, *33* (4), 319–333. DOI: 10.1016/S0378-7788(00)00114-6.
28. U.S. Department of Energy's (DOE) Building Technologies Office (BTO). (n.d.). *EnergyPlus*. Available at https://energyplus.net/
29. Minbud Ukrainy. (2021). *Teplova izoliatsiia ta enerhoefektyvnist budivel, chynnyi vid 2022-09-01, na zaminu DBN V.2.6–31:2016. Vyd. ofits*. (pp. 1–27). Ukraine.

30. Minrehionbud Ukrainy. (2015). *Enerhetychna efektyvnist budivel. Metod rozrakhunku enerhospozhyvannia pry opalenni, okholodzhenni, ventyliatsii, osvitlenni ta hariachomu vodopostachanni; chynnyi vid 2016-01-01. Vyd. ofits*. (pp. 1–145). Ukraine.
31. International Weather for Energy Calculations. (n.d.). Available at https://energyplus.net/weather-location/europe_wmo_region_6/UKR.
32. Ministry of Health of Ukraine. (n.d.). Available at https://covid19.gov.ua/karantynni-zakhody.
33. Minbud Ukrainy. (2013). *DBN V.2.5-67:2013. Opalennia, ventyliatsiia ta kondytsiiuvannia; chynnyi vid 2014–01–01*, (pp. 1–149).
34. Minrehionbud Ukrainy. (2013). *DSTU-N B V.1.1–27:2010. Budivelna klimatolohiia; chynnyi vid 2011-11-01*, (pp. 1–123).
35. López-Sosa, L. B., Alvarado-Flores, J. J., del Niño Jesús Marín-Aguilar, T., Corral-Huacuz, J. C., Aguilera-Mandujano, A., Rodríguez-Torres, G. M., … & Ávalos-Rodríguez, M. L. (2021). COVID-19 Pandemic Effect on Energy Consumption in State Universities: Michoacan, Mexico Case Study. *Energies*, *14* (22), 7642. https://doi.org/10.3390/en14227642.
36. Ayadi, O., Alnaser, S., Haj-ahmed, M., Khasawneh, H., Althaher, S., Alrbai, M., & Arabiat, M. (2023). Impacts of COVID-19 on Educational Buildings Energy Consumption: Case Study of the University of Jordan. *Front Built Environ*, *9*. DOI: 10.3389/fbuil.2023.1212423.
37. Agdas, D., & Barooah, P. (2020). Impact of the COVID-19 Pandemic on the U.S. Electricity Demand and Supply: An Early View from Data. *IEEE Access*, *8*, 205034-205050 DOI: 10.1109/ACCESS.2020.3016912.
38. Valeriy, D., Inna, B., Maryna, S., & Maksym, H. (2020). Evaluation of Differentiated Impact of Apartment Building Occupants' Behavior on Energy Consumption. *2020 IEEE 7th International Conference on Energy Smart Systems, ESS 2020 – Proceedings,* (pp. 196–200). Kyiv, Ukraine, 2020. DOI: 10.1109/ESS50319.2020.9160046.
39. Deshko, V., Sukhodub, I., & Yatsenko, O. (2018). Building Thermal State and Technical Systems Dynamic Modeling. *Journal of New Technologies in Environmental Science*, *2*, 36–46.
40. Lebedeva, K., Borodinecs, A., Krumins, A., Tamane, A., & Dzelzitis, E. (2021). Potential of End-User Electricity Peak Load Shift in Latvia. *Latvian Journal of Physics and Technical Sciences*, *58* (2), 32–44. DOI: 10.2478/lpts-2021-0010.
41. Savchenko-Pererva, M., Radchuk, O., Rozhkova, L., Barsukova, H., & Savoiskyi, O. (2021). Determining Heat Losses in University Educational Premises and Developing an Algorithm for Implementing Energy-Saving Measures. *Eastern-European Journal of Enterprise Technologies*, *6* (8(114)), 48–59. DOI: 10.15587/1729-4061.2021.245794.

LATVIAN JOURNAL OF PHYSICS
AND TECHNICAL SCIENCES
2024, N 2

DOI: 10.2478/lpts-2024-0013

INJECTION OF RENEWABLES GASES INTO THE EXISTING GAS DISTRIBUTION GRIDS AND EMPLOYMENT OF REVERSE GAS FLOW TECHNIQUE

L. Jansons[1,2*], J. Silina[1], I. Bode[1], L. Zemite[1], N. Zeltins[1], K. Palkova[3]

[1]Riga Technical University,
Faculty of Computer Science, Information Technology and Energy,
Institute of Power Engineering,
12-1 Azenes Str., Riga, LV-1048, LATVIA
[2]Riga Technical University,
Faculty of Engineering Economics and Management,
6 Kalnciema Str. 210, Riga, LV-1048, LATVIA
[3]Riga Stradins University,
Faculty of Social Sciences,
16 Dzirciema Str., Riga, LV-1007, LATVIA
*e-mail: leo.jansons@rtu.lv

Sustainability and longevity of existing gas grid exploitation perspective are closely related to two fundamental issues: their ability to adopt to changing gas fuel production and supply landscape in the context of methane-based fuels, mostly, biomethane, and in the context of non-methane-based fuels, mostly, low carbon and green hydrogen. Renewable gases and their ever-growing presence in gas transmission and distribution systems open up a discussion about the necessity to revise and restructure the original – vertically integrated layout of the gas systems, where gas supply is only technically possible from the transmission system towards distribution one, and not vice versa. Development of numerous decentralized biomethane production facilities connected to the gas distribution system causes a necessity to ensure the possibility to pass biomethane surplus of a certain production area into the gas transmission grid, thus avoiding necessity to install biomethane storage capacities locally and granting other regions an opportunity to use said surplus in their gas consumption immediately. The article addresses biomethane production trends and actions taken towards the development of reverse flow gas stations in France – one of biggest biomethane producers in Europe to date, and opportunities and challenges, which this technique might face in smaller and less active renewable gas markets as the one of Latvia.

Keywords: *Biomethane, gas distribution grids, renewable gases, reverse gas flow.*

1. INTRODUCTION

For a long time, natural gas has been perceived as the only viable bridging fuel in transition from fossil fuel dependency to green and sustainable energy future on the road towards European carbon neutrality in 2050. In some countries, natural gas has become the main fuel to generate electricity and heat energy, as the gas sector enjoyed rapid development in the first two decades of 21st century characterised by a considerably steady and favourable price [1]. However, the extensive utilization of fossil gas also had and still has its shortcomings. For instance, the EU dependency on natural gas imports went from 83 % in 2021 to 97 % in 2022, and in 2020 fossil gas that dominated the gas sector accounted for a quarter of European Union's (EU) greenhouse gas (GHG) emissions, which started to decrease steadily only in 2022 onwards. According to Eurostat data, in comparison with 2008 – the first year when statistical information on actual GHG emissions in different sectors of the EU's industry was collected, 2022 showed a significant decrease in emissions in the electricity, gas, steam and air conditioning sectors, accounting to 37% [2]. At the same time, in the gas power generation sector, reduction in GHG and more precisely carbon dioxide emissions is often in correlation with power plant age and the sophistication level of generating equipment: power generation at newer gas-fired plants is up to 30 % lower than that at older ones and up to 50 % lower than that at newer coal-fired plants [3].

Also, the Russian invasion of Ukraine constituted a significant breach of the global geopolitical order, with wide and far-reaching economic consequences. These include, but are not limited to, deterioration and turbulent changes of the world macroeconomic outlook, disruptions in trade, strong shockwaves across financial and commodity markets, and disrupted functionality of global fossil gas market [4]–[8]. It strongly impacted, yet did not completely ruined fossil natural gas positions as bridging fuel in the EU's energy transition. To meet its energy and economy decarbonisation targets, the EU aims at shifting into low-carbon gases whilst reducing the total gas consumption by 25 % by 2030. However, a clear roadmap for this cut-transition still needs to be approved.

At the same time, reduction of fossil gas presence in the EU energy sector poses a question – whether the gas sector will be thrown into total decline, thus gradually losing all the infrastructure investment done in this sector during the last 60 plus years, or it will be renewed by means of introduction of both methane and non-methane based renewables gases (RGs) to the grids [9]. According to the European Agency for the Cooperation of Energy Regulations and the Council of the European Union, such RGs as biomethane and hydrogen, have the potential to cover 30 % to 70 % of the total EU gas consumption by 2050 [10]–[11].

In terms of existing gas infrastructure and its availability, the EU gas networks provide an extensive integration potential for a wide range of RGs. The EU gas network is capable of transporting and storing large quantities of energy: it constitutes more than 200 000 km of transmission pipelines, over 2 million km of distribution network and over 20 000 compressor and pressure reduction stations. The value of the total infrastructure investments is approximately 65 billion euro (EUR) in EU gas transmission system operators' (TSO) regulated asset bases. Distribution system operators' (DSO) assets add to that figure at least by a factor of 3 [3]. In many cases, transformation and repurposing of the existing gas networks both at transmission and especially – distribution level, for RG application may prove itself to be more cost-efficient solution than building of new gas pipelines.

For the most well-known RG in the EU – biomethane, even special gas pipeline fittings are not necessary, as biomethane is chemically, and in its physical properties, indistinguishable from fossil natural gas [12]. As for mid-2023, Europe reached a total of 1322 biomethane-producing facilities, which is quite a decent share in comparison with total amount of biogas producing facilities, which then stood at approximately 20 000 [13]. In 2020, 4 % of total consumed gas in the EU and UK was RG, chiefly biogas and its derivates, like biomethane. Total volumes have more than doubled in the past 10 years.

Europe's combined biogas and biomethane production in 2022 amounted to 21 billion cubic meters (BCM). This is more than Poland's entire inland natural gas demand and represents 6 % of the EU's natural gas consumption in 2022. Biomethane production alone grew from 3.5 BCM in 2021 to 4.2 BCM in 2022. In the case of Denmark, the share of biomethane in the gas grid was close to 40 %. There are also plans to increase this production to substitute 100 % of the gas demand by 2030. The versatility of biomethane as a renewable energy source is reflected in its balanced distribution pattern across end-uses, all in urgent need for decarbonisation: 22 % was used for buildings in 2022, whereas a further 14 % was used in industry, 19 % for transport and 15 % for power generation [14].

It is a bit different in a case of the most promising RG of the future – hydrogen. In the transitional phase from methane based to non-methane-based RGs, forms of low-carbon hydrogen, for example, its blends, are needed to replace the existing natural gas and kick-start an economy of scale. The gas networks may use hydrogen blend of 5–20% [15] by volume and be tolerated by most systems without the need for major infrastructure upgrades or end-use appliance retrofits or replacements. The transmission of existing gas networks to hydrogen networks is one of the main aspects to achieve the hydrogen availability and in the meantime large-scale transportation. The promotion of hydrogen networks as future energy centres of the EU is gaining momentum, and the development of hydrogen related activities in all segments of energy sector are ongoing [16]. To decarbonise the natural gas grids, the threshold of hydrogen allowance in the existing grid systems must be increased. To create a consistent and long-lasting plan, the current energy sector players must participate in the development of the strategy, as actors in the field have command of currently used facilities and technologies.

However, in the mid-term perspective, along with emerging green and low-carbon hydrogen, biomethane will play an important role to achieve EU's energy decarbonisation, diversification of gas supplies and reduction of the EU's dependence on external energy deliveries, while simultaneously reducing exposure to volatile natural gas prices [17].

As a renewable and dispatchable energy source, scaling up the production and use of biomethane also help address the climate change. For these reasons, according to the EC, biomethane production needs to reach 35 BCM per year by 2030. To achieve this ambitious target, the EC presented in 2022 a Staff Working Document accompanying *REPowerEU* plan that includes a number of possible actions to unlock the potential of biogas and biomethane across the EU [18]. The proposed actions aim at supporting production to a sustainable potential volume of biogas to further upgrade it to biomethane and to direct biomethane production from waste and residues, avoiding the use of food and feed feedstocks leading to land use change issues. These actions should also create the preconditions for sustainable upgrading and safe injection of biomethane into the gas grid.

Also, for Latvia, which has rather developed and historically well-maintained gas TS and distribution system (DS), covering approximately 40 % of the country's territory, decarbonisation of the gas grids by means of introduction of biomethane and, with time, green and low-carbon hydrogen is one of the priorities in its energy agenda. It will allow not only using gas DS assets in the closest future, but also upgrading this system for successful exploitation in at least next fifty years.

2. PRINCIPLE OF REVERSE GAS FLOWS BETWEEN TS AND DS

Historically, the EU and the Latvian gas networks only worked in one direction. It meant a vertically integrated one-way operation, where the gas, once it got in the transmission system (TS), was routed at high pressure throughout TS and towards gas DS. In DS, its pressure is lowered to supply industrial facilities or pass through the network as far as individual residential consumers. As it has been described above, the EU gas network is very extensive at both transmission and distribution level [3].

As a result of these one-way operations, the predicted impact of biomethane development is blunted, unless its production points are connected directly to the TS. However, the gas DS is much more extensive, the probability that anaerobic digestion units are located close to one of the loops of this system is much higher, especially when full advantage is taken of the tremendous potential of raw materials in the form of household waste in and around urban areas. With the employment of reverse-flow station, gas systems become bi-directional; the surplus biomethane from DS can enter the TS and continue a conventional path to any consumption point.

Fig. 1. Noyal-Pontivy reverse gas flow station.

Source: GRTgaz

Industrial and agricultural waste treatment plants produce biomethane, which is equal in its quality to fossil natural gas, and can be used directly in the commercial and private markets. These units, featured by constant biomethane production throughout the year, are often connected to gas DS in urban or rural areas, where consumption is usually lower than production and is subjected to additional fluctuation challenges like seasonality. This excess represents added value if recovered and used in areas where demand exceeds supply. In this perspective, a number of green solutions have been designed to recover and reuse biomethane surplus, such as storage and the reverse flow techniques. The reversal technique consists of compressing unconsumed biomethane till distribution network working pressure level and then injecting it into the network at a higher pressure allowing locally produced RG to be supplied to a wider a consumption area.

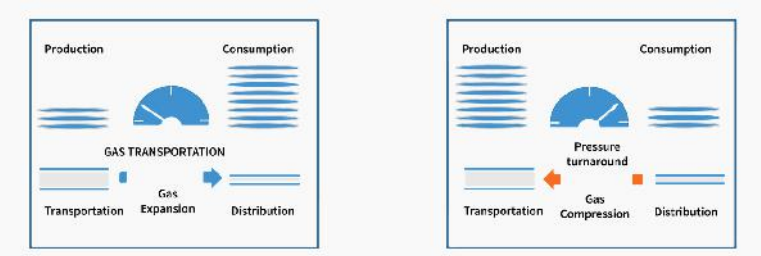

Fig. 2. The functionality of traditional gas TS and DS (a), and employment of reverse flow techniques between DS and TS (b).

The main function of a reverse gas flow station is that of a compressor: gas produced and unconsumed is compressed to a pressure equivalent to that of the transportation network. The mechanism works automatically: the compression unit starts up when the network pressure reaches the maximum expected threshold, above the estimated consumption of the biomethane station area. Then, the excess gas is compressed and injected into another network, bringing the initial network pressure to a low threshold where the compressor will stop.

With this versatile solution, the network becomes bi-directional and excess biomethane can join the transportation network at any point of consumption. These compression systems, from the distribution network to the transportation network, maximize the efficiency of the entire energy system because, thanks to a play of pressure peaks, they encourage the circulation of any surplus gas for immediate consumption or, otherwise, in storage units for future consumption. This avoids saturation of the system and the consequent dispersion of exceeding gas.

3. BIOMETHANE PRODUCTION AND EMPLOYMENT OF REVERSE GAS FLOW TECHNIQUE IN FRANCE

3.1. Biomethane Production in France

The gas TS in France is operated by two TSOs: GRTgaz and Terega. GRTgaz operates 8 110 km of the main network and 24 043 km of the regional networks, which makes around 87 % of the total gas TS in the country. Teréga, on the other hand, operates the remaining 13 % of gas TS, with 650 km of the main network and 4450 km of the regional networks in the south-west of France. The two networks interconnect in Castillon-la-Bataille and Cruzy.

DSs are owned by local communities and are managed through a concession-based system between local authorities and Gaz Réseau Distribution France (GRDF). GRDF operates 95 % of France's gas DSs, while 22 local distribution companies cover the remaining 5 % and offer their own regulated tariffs. The French gas distribution network totals 195 000 km, the second-longest gas network in Europe after Germany. Both TSs and DSs are open to third-party users, including RG producers [19].

As for early 2023, France had 1705 biogas production facilities. About 30 % of them – 514 facilities, purified biogas till the level of biomethane and provided injection of it into the regional gas grids. In comparison with 2020, the amount of biomethane facilities in France more than doubled, as in late 2020 there were only 214 of them in operation in the country.

The role of gas TSOs and DSOs in the development of biomethane production and distribution in France cannot be underestimated, if even many challenges in this process still lay ahead. The first role for gas operators such as Terega is to guarantee the right to inject for any biomethane producer located near a network – be it TS or DS related. Once certain technical and economic conditions are met, operators must make the necessary arrangements to allow access to their infrastructures.

TS, with a support of all DSs located close to production premises, carries out connection zoning: this jointly-run futurology exercise makes it possible to determine the optimal way of welcoming all producers onto the grid who want to inject their biomethane over the coming years. The subtle technical and economic balance found as a result of the process is aimed at creating the best possible conditions for developing the grid at the lowest possible cost. Once the mapping is decided upon, operators will be able to consult the Energy Regulation Commission (CRE) and stakeholders wanting to have a stake in those projects, and then get the investment funding released, to build, operate and maintain the new plants.

This process is part of our public service mission, supporting the creation of energy and jobs in local areas, at the same time guaranteeing sustainability of gas related industry. In France in 2022, close to 7000 gigawatt – hours (GWh) of biomethane were injected into the gas grids (see Fig. 3), representing 10 % of former imports of Russian fossil gas. Thus, these 7000 GWh covered only 2 % of France's gas consumption over the year, the peak levels of biomethane injections were observed in August, 2022, when 10 % of all gas flowing through the grid in the southern part of the country, was biomethane [20].

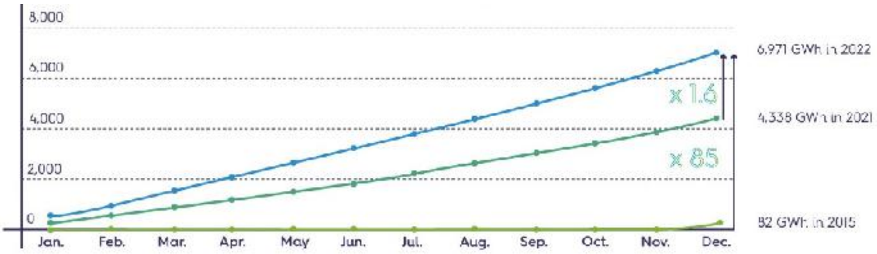

Fig. 3. Biomethane injected into the gas grids in France (2015, 2021, 2022, in GWh), [20].

Source: *Terega*

Tools to speed up biomethane markets growth are also considered or introduced in France and a few other EU countries, namely:

- indexation of the regulated purchase tariff to keep up with fluctuation of inflation rates. Announced at the end of 2022, the change in the tariff also considers the hourly cost of labour and the production price index;
- support for biomethane production by invitations to tender. At the end of 2022, public stakeholders decided to launch calls for tender for biogas production. The first tranche was for 500 GWh, at a price judged by producers to be too low. A new round of invitations to tender were launched afterwards;
- issue of biogas production certificates. The idea to put energy suppliers under an obligation to supply a proportion of their portfolio of customers with biomethane. Whether they produce it themselves or buy it from third party producers, that biomethane will give them certificates to prove they are full filling the obligations. This arrangement would help share out the work of developing the industry across the state, producers and energy suppliers;
- biomethane purchase agreement. These direct negotiation contracts are negotiable directly and freely between a biomethane producer and an end consumer. This simplification of the transaction process is meant to speed up the development of a virtuous local ecosystem [21].

3.2. Employment of Reverse Gas Flow Technique in France

In recent years, France has experienced a fast development of biomethane production. To facilitate this development and maximize its potential, the gas TSO GRTgaz is planned to build more than 30 reverse gas flow stations plants, most of which were commissioned between 2022 and 2024, facilitating the integration of RG into existing gas networks. To date, GRTgaz operates five such plants, and further 13 sites are under construction and CRE has already validated the investment for seven new projects and the study of nine additional ones.

A reverse flow station transfers local biomethane surpluses on the distribution networks to the transmission network, to be transported to another territory or stored. Reverse flow, thus, gives a greater visibility to project owners and encourages concrete plans for anaerobic digestion units, as it allows all local production to be accepted by the network at any time, particularly in summer when production may be higher than consumption. These gas infrastructure developments offering smart biomethane logistics provide renewable energy that is fully controllable and storable, and hence extremely useful for the stability of the energy system.

Maximum reliability and availability are one of the key factors for successful development and utilisation of reverse gas flow stations. Compression units are installed inside soundproof, water-resistant steel cabins and are equipped with gas and fire detection systems ensuring high levels of safety. The control panel, which manages both the power and the compressor unit, has been designed and installed in a dedicated room. Through manual dryers (present in two out of eight stations) installed upstream the compression unit cleans and dries the gas when the water content of the network is too high. Furthermore, water cooling system cools the gas at each compression stage ensuring that the compressor works properly.

The systems can be equipped with a compressor unit with an installed power of 2.2 kW and a maximum capacity of 3 m^3/h. This compressor unit operates over a wide range of pressures in both suction (10 to 500 mbar) and discharge (40 to 67.7 bar). Its operation is automatic and controlled by the control panel fully integrated inside the system: each time the inlet gas exceeds a pressure of 200 mbar, the compressor unit is activated, recovering any gas leaks, thus avoiding dispersion into the atmosphere. Once the gas pressure is reduced to 10 mbar, the compressor unit stops.

It is a technique that makes it possible to optimize the flow of biomethane, confirming that biomethane is a flexible, efficient and programmable source. The solutions highlighted are the result of know-how gained in over 40 years of activity in the compression technology, which has enabled the development of tailor-made and highly innovative projects.

In a decision published in July 2021, CRE approved the launch of studies for the installation of nine new reverse flow projects. GRTgaz currently has a portfolio of 32 reverse flow projects in France, for a total investment of nearly EUR 100 million. GRTgaz already operates five reverse flow stations in Noyal Pontivy, Pouzauges, Mareuil-lès-Meaux and Marchémoret and Marmagne [22].

With its project portfolio, GRTgaz confirms its commitment to RGs and its ability to support the development of the sector by combining the rollout of reliable solutions with targeted investments where necessary. As part of its business plan for 2021–2024, GRTgaz also aims at connecting around a hundred anaerobic digestion sites directly to its network.

4. A BRIEF OVERVIEW OF THE LATVIAN GAS DS

The gas DS plays an essential role in the continuous, safe supply of natural gas not only to the households, but also to commercial and industrial consumers.

The technical operation of distribution gas pipeline systems in Latvia is carried out by the gas DS JSC Gaso (GASO), which is the only operator of the natural gas DS in Latvia and ensures the supply of gas from the TS to end consumers. The company ensures development of distribution infrastructure, construction of gas connections, system operation and natural gas accounting, as well as emergency service operation. GASO was founded on 22 November 2017, separating the operation of the gas DS from JSC Latvijas Gāze and fulfilling the EU and state requirements for ensuring the independence of the natural gas DSO. In 2023, the process of selling the company was started, after the Competition Council of Republic of Latvia ruled that the Estonian company Eesti Gaas was allowed to gain decisive influence over GASO [23].

Until the 1990s, mainly steel pipes were used for the construction of distribution gas pipelines. However, now polyethylene pipes are increasingly preferred – this practice is not only in the Baltic States, but also in other parts of Europe. This change in preferences is, accordingly, also reflected in the current share of materials for the production of distribution gas pipelines in the Latvian gas supply system. The percentage distribution of distribution gas pipelines in Latvia according to the material used is 60.5 % steel and 39.5 % polyethylene, from which it can be concluded that most of the pipelines that have been replaced in the past twenty-five years are made of polyethylene.

Therefore, the share of steel distribution gas pipelines in the gas supply system of Latvia is shrinking; however, their further use should be continued in case of good technical condition.

According to the data collected in 2023, the total length of distribution system gas pipelines in Latvia is 6 409 km.

However, gas distribution systems do not consist only of gas pipelines, they also include gas regulation equipment, special structures, shut-off devices, anti-corrosion equipment, as well as other technical devices. At present, there are 175 gas regulation points, 2 383 cabinet-type gas regulation points, 18 979 home regulators, 5 222 home stabilizers in the Latvian gas DS.

The total amount of distribution gas pipelines in Latvia is divided by service districts: the total length of distribution gas pipelines in the territory of Riga district reaches 3 296.9 km, in the territory of Ogre district – 294.9 km, in the territory of Liepaja district – 459.8 km, in the territory of Jurmala district – 468.8 km, in the territory of Jekabpils district – 197 km, in the territory of Jelgava district – 589.4 km, in the territory of Daugavpils district – 227.1 km, in the territory of Cesis district – 473.1 km and in the territory of Bauska district – 401.7 km. According to the percentage distribution, the pressure classes of gas DS pipelines are as follows: low pressure (<=0.05 bar) – 38.6 %, mean pressure (<= 0.1 bar) – 6.6 %, mean pressure (<= 4 bar) – 36.4 %, high pressure I (<=6 bar) – 12.3 %, high pressure II (<= 12 bar) – 3.5 %, high pressure III (<= 16 bar) – 2.6 %. The technical operation of distribution gas pipeline systems is based on LVS 445-1:2011 on “Operation and maintenance of natural gas distribution systems and user natural gas supply systems with a maximum working pressure of up to 1.6 MPa (16 bar)” performing the specified actions, but is not aimed at determining the causes of deterioration (damage) of the technical condition of gas pipelines, as well as predicting further safe operation [24].

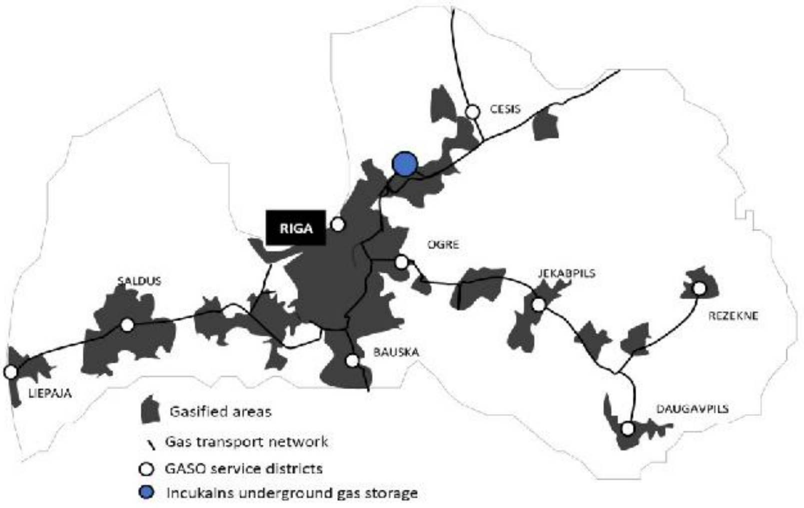

Fig. 4. Principal scheme of the Latvian gas TS and DS.

Source: GASO

Over time and in the process of operation of the technical equipment and equipment of the system, the technical characteristics of this equipment deteriorate, the adjustment of nodes and the aging of elements occur, as well as the risk of explosive situations increases [25]. Most often, already performing preventive maintenance of the elements of the gas DS, potential faults are detected and eliminated in time. Permanent preventive measures of the whole system are not necessary; it should most often be done only partially – with the aim of restoring damaged or potentially damaged elements [26]. The most effective is prevention, depending on the technical condition of the equipment and facilities of the gas DS [27], but to ensure it, continuous control of the system is required, which is associated with additional financial investments.

5. REVERSE GAS FLOW EMPLOYMENT PROSPECTS AND LIMITATIONS

Following gas infrastructure planning, the network has been upgraded or is planned to better match prospects of decentralized biomethane production. In this context, gas DS and TS improvements are required to accommodate the injection of biomethane at various sites different from originally vertical, one-way operation structure of the grid. As a solution, certain reverse flow facilities can be considered to allow the bi-directional flow from the TS to the DS and vice versa. In 2021, 15 reverse flow facilities were operation in Denmark, France, Germany, and the Netherlands, with 25 under construction in Denmark, France, and Belgium and 16 feasibility studies were announced in France and Italy. It is important to consider that reverse flow facilities not always depend on the degree of interconnection in a country's gas systems, which can reduce the need for compression [28].

The European gas TSOs and DSOs are identifying the zones with abundant feedstock availability and developed gas grid infrastructure, with injection technically and economically viable. These zones are sometimes also targeted as priority locations for biomethane hub development. This should speed up permitting procedures in these areas as the grid infrastructure check is already done. Areas with good feedstock availability but weaker grid infrastructure should also be considered important, if the most of the sustainable feedstocks that should be mobilized in the short term are agricultural waste and residues. For these zones, TSOs and DSOs will be able to anticipate the grid upgrades that might be necessary if biomethane projects are to be developed there. The EU Member States could choose to mandate TSOs and DSOs to prepare for potential project connections, so that biomethane can be integrated into the grid in case projects are developed. The overall grid infrastructure assessment should include the potential need for gas grid upgrades including capacities and injection points, but also regarding flows, pressure levels etc. Additional grid equipment installation and reverse flow capacities should also be considered and planned [29].

Currently, more than 40 biogas plants with a total installed capacity of approximately 56 megawatts are operating in Latvia. 41 agricultural biogas stations annually use a total of 1.85 million tons of raw materials, of which 847 thousand tons are different types of manure. The rest of the volume is made up of food production waste, sewage sludge, damaged fodder. All kinds of manure and other waste make up about 70 % of the raw materials for biogas production in Latvia. Approximately 12 % of the Latvian biogas plants use waste landfill resources for biogas production, two percent are sewage sludge substrate biogas plants, five percent are facilities that produce biogas from production residues or wastewater, and the majority – 81 % – are powered by agricultural waste. Most of them are located quite close to both the natural TS and DS. A number of obstacles, such as land ownership and the lack of well-defined and transparent support schemes, may hinder the transfer of biomethane into the gas supply network, and these issues should be adequately addressed in the future.

As for the case of Latvia, employment of reverse gas flow stations would be a beneficial in regions, where biomethane production would constantly exceed its local consumption or were there are no possibilities to distribute the surplus biomethane to local gas consumers via DS connections only. If examining a historical map of the Latvian biogas production facilities locations, and speculating that about ¼ of them would, in passage of time, convert itself into biomethane production facility, it is obvious, that the biogas stations grouping has two obvious patterns.

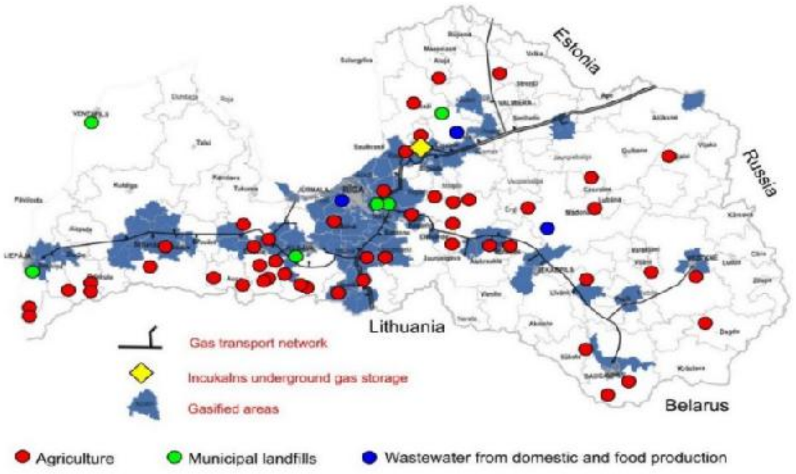

Fig. 5. Location and type of biogas plants in Latvia in 2020, with respect to the natural gas network [9].

Source: GASO, the Latvian Biogas Association

The first is the proximity of facilities to rather big gas consumption centres and their clustering, where connection to both gas TS and DS is available. The second is slightly different, manifesting remoteness of such consumption hotbeds, but obvious closeness to big amounts of resources for both biogas and biomethane production. The facilities of the second group are not obviously clustering in groups, they are more regionally speeded, and in most cases, geographically closer to DS. Some facilities are also significant, as they stand in locations where the closest point to any gas network is really far away, and, even in case of their conversion for biomethane production, they most likely will not be among contributors to biomethane grid injections.

6. CONCLUSION

There are evident benefits to employment of a reverse gas flow technique in large countries and gas markets such as France, but clear benefits from potential employment of it in smaller countries with limited gas consumption such as Latvia are not so obvious in the short- and mid-time perspective. In larger countries with a mature biomethane production portfolio, a large number of biomethane producers, significant fuel output capacities, and a rapidly developing RG market, which is considered both part of gas market as a whole and its exclusive part, entitled to specific and expanding range of support schemes or tools, the use of a reverse gas flow technique could be regarded almost inevitable.

The market situation in smaller countries, such as Latvia, is not manifesting an immediate practical necessity for employment of a reverse gas flow technique, as owners of biogas facilities with a biomethane production potential in any location in Latvia cannot currently evaluate business risks associated with engaging with a reverse gas flow station development project in the foreseeable future. The first, production process unrelated, reason is a lack of legal framework and clear expense sharing blueprint for such a project, as well as a small number of realized biomethane production facilities and projects currently exploring gas grid connection opportunities.

Therefore, employment of a reverse gas flow technique could be immediately suitable only for:

- large and extensive, rapidly growing diversified gas markets at the national scale;
- large and extensive, rapidly growing diversified gas markets at a limited transnational scale (for projects located on the border with one neighbouring country, which has enough gas interconnections with country of biomethane origin, and has regulation allowing passing neighbour's biomethane surplus to its TS);
- smaller countries, but with the same intensive development of diversified gas market, large-scale biomethane production and injection into the grid;
- clusters of smaller countries with both large and extensively developing or/and emerging diversified gas markets (for projects located on the border with more than one neighbouring country, which has enough gas interconnections with country of biomethane origin, and has regulation allowing passing neighbour's biomethane surplus to its TS).

Also, the issue of non-methane-based RG usage in gas TS and DS in respect to the exploitation of reverse gas flow stations should be raised. It should be clarified, can these stations, dedicated to the use of methane-based RG only, in foreseeable future facilitate unknown percentage (in case of Latvia, up to 2 %) of hydrogen by volume in the gas mix. Here only theoretical assumptions can be made, i.e., safe percentage of hydrogen contents in the methane-based fuel should be legally and technically set before realization of any reverse gas flow station project. It would help ensure the longevity of reverse gas flow station equipment in the period of time when designated safe percentage of hydrogen would not be exceeded in TS and/or DS.

ACKNOWLEDGEMENT

The research has been funded by the Latvian Council of Science, project “Mitigating Energy Poverty through Innovative Solutions”, project No. lzp-2023/1-0214.

REFERENCES

1. FRED. Economic research. (n.d.). *Global Price of Natural Gas, EU.* Available at https://fred.stlouisfed.org/series/PNGASEUUSDM
2. EC. (2023). *EU Economy Emissions in 2022: Down 22% since 2008*. Available at https://ec.europa.eu/eurostat/web/products-eurostat-news/w/ddn-20231221-3
3. ACER. (n.a.). *Gas Factsheet.* Available at https://www.acer.europa.eu/gas-factsheet
4. Albrizio, S., Bluedorn, J.C., Koch, C., Pescatori, A., & Stuermer M. (2022). *Market Size and Supply Disruptions: Sharing the Pain from a Potential Russian Gas Shut-off to the EU.* IMF Working Papers.
5. Garicano, L., Rohner, D., & Weder, B. (2022). *Global Economic Consequences of the War in Ukraine: Sanctions, Supply Chains and Sustainability*. Centre for Economic Policy Research. Available at https://cepr.org/publications/books-and-reports/global-economic-consequences-war-ukraine-sanctions-supply-chains-and
6. World Bank. (2022). *The Impact of the War in Ukraine on Global Trade and Investment*. Equitable Growth, Finance and Institutions Insight.
7. Ferriani, F., & Gazzani, A. (2023). *The invasion of Ukraine and the Energy Crisis: Comparative Advantages in Equity Valuations.* Available at https://cepr.org/voxeu/columns/ukraineinvasion-and-energy-crisis-comparative-advantages-equity-valuations
8. Boungou, W., & Yatié, A. (2022). The Impact of the Ukraine–Russia War on World Stock Market Returns. Economics Letters, *215*, 110516.
9. Savickis, J., Zemite, L., Zeltins, N., Bode, I., Jansons, L., Dzelzitis, E., … & Ansone, A. (2020). The Biomethane Injection into the Natural Gas Networks: The EU’s Gas Synergy Path. *Latvian Journal of Physics and Technical Sciences*, *57* (4), 34–50. https://doi.org/10.2478/lpts-2020-0020
10. ACER. (2020). *ACER Report on NRAs Survey – Hydrogen, Biomethane, and Related Network Adaptations*. ACER, Ljubljana.
11. EC. (2019). *Smart Sector Integration: Promoting Clean Energy – Policy Debate.* Available at https://data.consilium.europa.eu/doc/document/ST-13854-2019-INIT/en/pdf
12. Bakkaloglu, S., & Hawkes, A. (2024). A Comparative Study of Biogas and Biomethane with Natural Gas and Hydrogen Alternatives. *Energy & Environmental Science*. DOI: 10.1039/D3EE02516K
13. EBA. (2023). *Biomethane Map 2022–2023*. Available at https://www.europeanbiogas.eu/wp-content/uploads/2023/05/GIE_EBA_Biomethane-Map-2022-2023.pdf
14. EBA. (2023). *20% Increase in Biomethane Production in Europe, Shows Biogases Industry Report Released Today.* Available at https://www.europeanbiogas.eu/wp-content/uploads/2023/12/PR_EBA-Statistical-Report-2023.pdf
15. Zemite, L., Jansons, L., Zeltins, N., Lapuke, S., & Bode, I. (2023). Blending Hydrogen with Natural Gas/Biomethane and Transportation in Existing Gas Networks. *Latvian Journal of Physics and Technical Sciences*, *60* (5), 43–55. https://doi.org/10.2478/lpts-2023-0030_
16. EHB. (2023). *European Hydrogen Backbone Maps*. Available at https://ehb.eu/page/european-hydrogen-backbone-maps

17. BMP Greengas. (n.d.). *Benefits of Biomethane*. Available at https://www.bmp-greengas.com/knowledge/benefits-of-biomethane/
18. EC. (2022). *Commission Staff Working Document Implementing the REPowerEU Action Plan: Investment Needs, Hydrogen Accelerator and Achieving the Bio-methane Targets Accompanying the Document Communication from the Commission to the European Parliament, the European Council, the Council, the European Economic and Social Committee and the Committee of the Regions.* REPowerEU Plan. {COM(2022) 230 final} https://eur-lex.europa.eu/legal-content/EN/TXT/PDF/?uri=CELEX:52022SC0230
19. IEA. (2020). *France Natural Gas Security Policy*. Available at https://www.iea.org/articles/france-natural-gas-security-policy
20. Terega. (n.d.). What are the Prospects for Biomethane in France in 2023? Available at https://www.terega.fr/en/newsroom/editorial/what-are-the-perspects-for-biomethane-in-france-in-2023
21. Kanda, W. (2024). Systems and Ecosystems in the Circular Economy: What's the Difference? *Journal of Circular Economy, 2* (1). https://doi.org/10.55845/RMDN3752
22. GRTgaz. (n.d.). *GRTgaz Steps up its Plans to Accommodate Biomethane from the Regions.* Available at https://www.grtgaz.com/en/medias/press-releases/32-reverse-flow-projects
23. Konkurences padome. (2023). *Konkurences padome atļauj Igaunijas kompānijai iegādāties AS "Gaso" [The Competition Council authorises an Estonian company to acquire JSC Gaso].* Available at https://www.kp.gov.lv/lv/jaunums/konkurences-padome-atlauj-igaunijas-kompanijai-iegadaties-gaso
24. Latvijas Standarts. (2011). *Dabasgāzes sadales sistēmas un lietotāja dabasgāzes apgādes sistēmas ar maksimālo darba spiedienu līdz 1,6 MPa (16 bar) ekspluatācija un tehniskā apkope. 1. daļa: Vispārīgās prasības (LVS 445-1:2011).* Available at https://www.lvs.lv/lv/products/29043
25. MBS Engineering. (2019). *The Benefits of Preventative Maintenance to your Gas Pipes.* Available at https://www.mbs.engineering/mbs-engineering-blog/the-benefits-of-preventative-maintenance-to-your-gas-pipes
26. Kermanshachi, S., Cobanoglu, M., & Damnjanović, I. (2017). An optimal preventive maintenance model for natural gas transmission pipelines. In A. Pridmore, J. Geisbush (Eds.), *Pipelines 2017: Condition Assessment, Surveying, and Geomatics*: *Proceedings of Sessions of the Pipelines 2017* (pp. 517–526). American Society of Civil Engineers (ASCE). https://doi.org/10.1061/9780784480885.048
27. Zemite, L., Kutjuns, A., Bode, I., Kunickis, M., & Zeltins, N. (2018). Consistency Analysis and Data Consultation of Gas System of Gas-Electricity Network of Latvia. *Latvian Journal of Physics and Technical Sciences*, *55* (1), 22–34. https://doi.org/10.2478/lpts-2018-0003
28. Gas for Climate. (2021). *Market State and Trends in Renewable and Low-Carbon Gases in Europe.* Available at https://www.europeanbiogas.eu/wp-content/uploads/2021/12/Gas-for-Climate-Market-State-and-Trends-report-2021.pdf
29. Gas for Climate. (2019). *The Optimal Role for Gas in a Net-Zero Emissions Energy System.* Available at https://www.europeanbiogas.eu/wp-content/uploads/2019/11/GfC-study-The-optimal-role-for-gas-in-a-net-zero-emissions-energy-system.pdf

LATVIAN JOURNAL OF PHYSICS
AND TECHNICAL SCIENCES
2024, N 2

DOI: 10.2478/lpts-2024-0014

ANALYSIS OF THE ENERGY CONSUMPTION FOR HEATING IN SCHOOLS

M. Sinakovics, A. Zajacs*, A. Palcikovskis, V. Jacnevs

Department of Heat Engineering and Technology,
Riga Technical University,
6A Kipsalas Str., LV – 1048, Riga, LATVIA
*e-mail: aleksandrs.zajacs@rtu.lv

The aim of the study is to analyse energy consumption for heating in set of the school buildings. Data analysis includes three data sets – predictions from energy performance certificates (EPC), measured data from heat meters and measured climate corrected data. Data sets were statistically checked and processed and represented graphically. The actual energy consumption differs from the one stated in the EPCs in all cases, which means that schools consume on average 15 % more energy than it is stated in the EPC. Overall, the data reveal that the actual energy consumption differs from the theoretical consumption, with all schools having higher actual consumption than the theoretical values. The differences in the data sets are discussed, and possible improvements are suggested taking into account strong relation between energy consumption and indoor air quality.

Keywords: *Energy consumption, energy performance certificates, heating, school buildings.*

1. INTRODUCTION

Importance of the indoor air quality (IAQ) and thermal comfort in the educational buildings cannot be underestimated. According to the ASHRAE IAQ, upgrades can improve learning outcomes and mitigate the risk of transmission of airborne pathogens within the educational environment [1]. However, every school and its HVAC systems are unique and require certain efforts of a qualified professional in assessing each facility's unique characteristics. School buildings are considered to be one of the most diverse structures from the perspective of energy-efficient design and construction [2]. The current study is focused on the Latvian secondary education buildings with purpose to compare predicted energy demand according to the energy performance certificates (EPC), actual energy consumption according to the heat meter data and actual consumption adjusted according to the degree days. It is important to discover the reasons of discrepancies between those mentioned data sources and provide possible solutions to improve data reliability.

This is important due to several reasons. First of all, it is necessary to understand whether it is possible to reduce energy consumption without lowering the indoor air quality and thermal comfort of the building users. Influence of building envelope properties on the energy efficiency is described in studies [3], [4]. The second reason is the fact that usually educational buildings are operated, maintained and paid or subsidised by municipalities or government. Finding the proper methods and strategies for the reduction of energy demand will provide considerable savings in terms of funds and primary energy consumption, which is beneficial for authorities to reach high European and national energy and climate targets. For example, in [5] it is stated that in Sweden the largest amount of energy is consumed in school buildings, i.e., where schools form the highest number of public properties (30 million m2). In total, schools consumed 4 222 GWh of district heating and about 3 GWh of electricity for heating and other purposes in 2020. Correlation of energy efficiency and thermal comfort based on simulation results is discussed in the studies [6]–[9], which show how window orientation and opening influence ventilation efficiency and thermal comfort. Many studies have already been performed across the world in order to analyse and compare energy consumption and conclude on further optimization steps [10], [11].

Authors of the study [12] argue that the methodology used for the evaluation of school buildings can be extended from public buildings to a commercial building stock, residential buildings and small houses. This can provide valuable information, in particular, for property owners whose buildings have been recently renovated or who intend to do so in the future. Renovation wave of the existing building stock of the European Union is spinning off, which means that the results of the study will be relevant for different stakeholders related to the building operation and management. In Canadian northern climate, researchers also conclude [13] that newer and renovated building consume less energy; however, electricity consumption is higher. Researchers from Korea [14] show that energy demand in school buildings is rising alongside with an increase in the use of interactive teaching methods, cooling and cooking options. It varies a lot between 67–240 [kWh/m^2/yr]; however, it should be mentioned that there is no significant difference in energy consumption per student.

However, some problems with moisture accumulation in the construction and best practice examples of retrofitting solutions are described in [15]–[18]. The design of the ventilation system in retrofitted buildings with passive use of solar energy is discussed in [19]–[21], showing how to avoid unnecessary overheating during summer months. While indoor air quality is a very important factor, it strongly depends and correlates with specific energy demand of the building. Study [22] reports the indoor air quality and overheating levels in eight recently built classrooms of two new low-carbon primary schools during heating and non-heating seasons. The analyses indicated that most of these classrooms had experienced overheating for more than 40 % of school hours, as well as revealing that CO2 concentration levels were above the maximum threshold of 1000 ppm for more than 60 % of school hours in heating and non-heating seasons.

Decentralised ventilation units can be proposed as a local solution; the efficiency of these units is described in [23], with precautions to use it, while delivering very poor heat recovery efficiency between 20 % and 50 %. The effect of CO_2 concentration on children's well-being during the process of learning is evaluated in [24]. Additionally, it is important to note that for renovated building rooms the concentration of volatile organic compounds (VOC) can be a problem, while any pollution requires additional ventilation rates and energy consumption for ventilation. The influence of renovation and pollution on the energy performance and ventilation rates is discussed in [25]–[27]. The paper [28] analyses a performance gap between predicted (calculated) and measured (actual) delivered energy for space heating in 185 school buildings. Considering the abovementioned information, it is important to perform evaluation of the energy demand in school buildings on a national or even a regional level with the aim to provide a basis for developing strategies and plans to improve energy efficiency both with passive and active methods.

2. METHODOLOGY

An analysis was conducted on the energy consumption of 25 public schools in Riga. The data used for analysis included the following parameters: monthly energy consumption from January 2020 to September 2022 for all 20 schools, climate data of Riga for the above-mentioned period and EPC for 11 schools. The 11 schools with EPC provided additional data, including information about the school address, area, heating system, hot water preparation, mechanical ventilation, lighting, cooling and additional features. All data sets were statistically evaluated and checked. A basic survey of the buildings was performed, such as visual inspection from the outside.

With this information, it was possible to compare three different types of heating energy consumption: theoretical (as provided in the EPC), actual (as provided in the monthly energy consumption reports) and degree day consumption, which was recalculated based on the external temperature for each year.

Out of 25 buildings, only for 20 of them data were fully available and reasonable for further evaluation. 20 buildings were divided into two groups, where 9 buildings were without existing EPC and 11 buildings were with EPCs. Thus, it was possible to make comparison between predicted EPC values and actual consumption data.

For further evaluation, the actual heat energy consumption data were processed using the following assumptions: all 20 buildings did not have data on hot water consumption, so heat energy consumption for the period outside the heating season was considered as consumption for domestic hot water (DHW) preparation. Note: these are not representative values during the summer months (June–August).

For the corrections of the climate influence the heating degree day (HDD) method was used and all heat energy consumption values associated only with heating needs were corrected by an actual climatic HDD factor for corresponding time periods. Climate data were obtained from the public web database of the official Centre of Environmental Geology and Meteorology of Latvia. Further data were processed and presented graphically.

3. RESULTS

Upon comparing the schools without EPC (a total of 9), the data demonstrated the following trends (summarised in Table 1): the total heating energy consumption for the 7 schools in Riga varied from 226.32 MWh in School 1 to 682.48 MWh in School 4 in 2021. Overall, there was a noticeable pattern of rising energy consumption from 2020 to 2021, as evidenced by the decreasing MWh values in most of the buildings, which could be attributed to 2021 being a colder year compared to 2020.

Table 1. Heating Energy Consumption (Schools without EPC)

	Heating energy consumption, MWh			Heating energy consumption (HDD corrected), MWh		
School	2020	2021	2022, until September	2020	2021	2022, until September
School 1	461.33	226.32	127.99	585.18	236.19	142.13
School 4	561.67	682.48	381.69	712.45	712.25	423.85
School 6	509.87	642.56	412.54	646.75	670.59	458.11
School 9	392.85	468.89	281.92	498.31	489.34	313.06
School 10	223.88	313.20	180.18	283.98	326.86	200.08
School 11	269.35	306.62	176.78	341.66	320.00	196.30
School 12	470.65	537.62	316.17	597.00	561.07	351.10
School 18	516.41	565.87	306.05	655.05	590.55	339.85
School 19	480.40	629.24	342.37	609.36	656.69	380.19

For instance, in School 4, the energy consumption increased from 561.67 MWh in 2020 to 682.48 MWh in 2021. Similarly, in School 6, the energy consumption increased from 509.87 MWh in 2020 to 642.46 MWh in 2021.

Data from schools with EPC show similar results. If degree days are included in the analysis of energy consumption, it is possible to see that 2021 is colder than 2020 (data summarised in Table 2).

Table 2. Heating Energy Consumption (Schools with EPC)

School	Heating energy consumption, MWh			Heating energy consumption (HDD corrected), MWh		
	2020	2021	2022, until September	2020	2021	2022, until September
School 5	311.23	396.20	218.28	394.78	413.49	242.39
School 7	495.78	593.92	334.27	628.88	619.83	371.20
School 8	549.51	626.11	326.02	697.03	653.42	362.03
School 13	226.49	362.51	212.79	287.29	378.32	236.30
School 14	602.01	710.62	395.34	763.63	741.62	439.01
School 15	433.29	519.87	387.67	549.61	542.55	430.49
School 21	468.52	503.45	330.66	594.29	525.41	367.19
School 22	590.30	760.23	390.97	748.77	793.39	434.16
School 23	544.85	521.32	278.02	691.12	544.06	308.73
School 24	435.58	490.72	344.49	552.52	512.13	382.54
School 25	408.58	485.24	280.60	518.27	506.40	311.59

Specifically, when considering degree days, half of the schools showed higher energy consumption in 2020 compared to 2021. For example, the consumption of School 4 in 2020 and 2021 was 561.67 MWh and 682.48 MWh, yet with degree days it was 712.45 and 712.25 MWh; consumption in 2020 increased by 28 % and in 2021 by 4.5 %.

4. CONCLUSIONS

From the preliminary analysis of the study, it can be concluded that the accounting of degree days has a significant impact on heat energy consumption. To illustrate this point further, schools such as School 8, School 14 and others show an increase of approximately 27 % in heating consumption in 2020. The consumption values changed from 549.51 MWh to 697.03 MWh and from 602.01 MWhto 763.63 MWh, respectively.

The summary of the results is presented in Fig. 1.

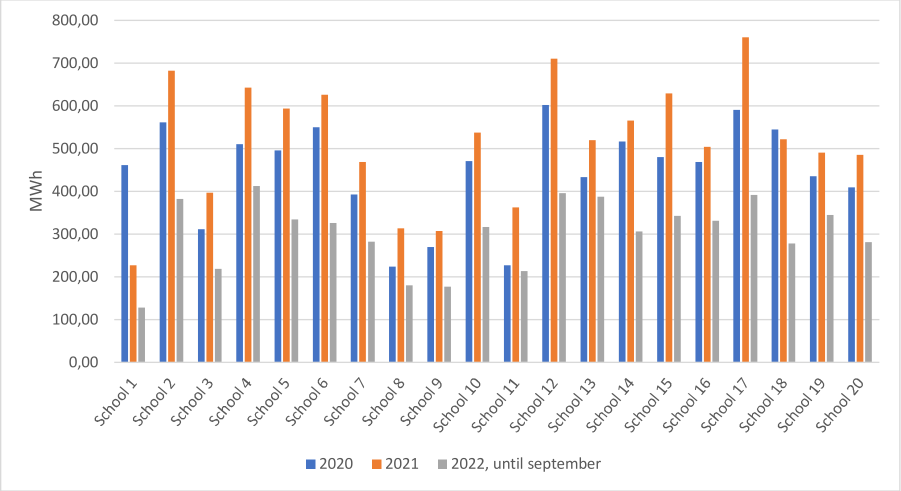

Fig. 1. Heat energy consumption.

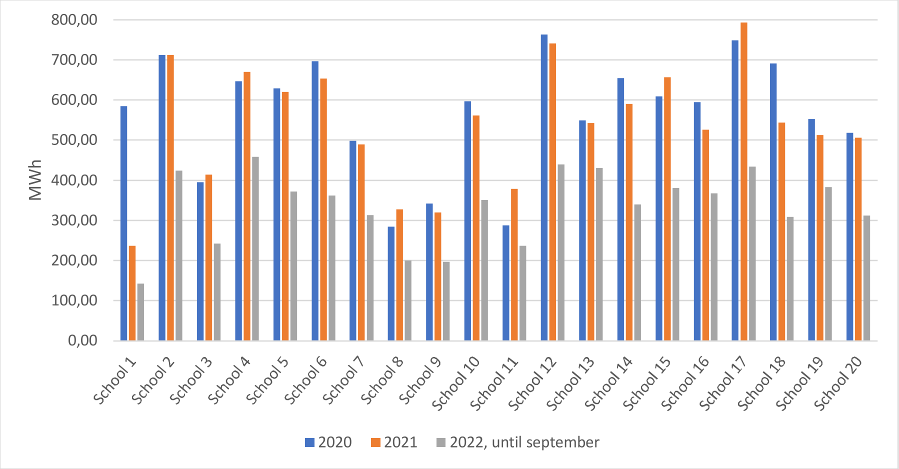

Fig. 2. Heat energy consumption adjusted according to HDD.

Upon examining the graphs, it becomes apparent that degree day adjustment helps to slightly even out the consumption patterns across the years, enabling a clearer view of the actual energy consumption.

Since more data were available for schools with EPC, including the area of the building and EPC, it facilitated a comparison of the heating energy consumption stated in the certificates and reports against the calculated consumption in kWh/m^2. The results are presented in Table 3.

Table 3. Heating Energy Consumption for m^2 (Schools with EPC)

Heating energy consumption, kWh/m^2				Heating energy consumption (HDD corrected), kWh/m^2		
School	2020	2021	2022, until September	2020	2021	2022, until September
School 5	60.53	77.05	42.45	76.78	80.41	47.14
School 7	48.27	57.82	32.54	61.22	60.34	36.14
School 8	54.34	61.91	32.24	68.92	64.61	35.80
School 13	47.90	76.67	45.00	60.76	80.01	49.97
School 14	60.15	71.00	39.50	76.30	74.10	43.86
School 15	42.63	51.15	38.14	54.08	53.38	42.36
School 21	91.56	98.39	64.62	116.15	102.68	71.76
School 22	58.57	75.44	38.80	74.30	78.73	43.08
School 23	52.23	49.97	26.65	66.25	52.15	29.60
School 24	83.36	93.91	65.92	105.74	98.01	73.21
School 25	89.58	106.38	61.52	113.63	111.02	68.31

As shown in Table 3, using degree day adjustment evens out heating consumption and allows seeing the real kWh/m^2 consumption regardless the temperature in the following year. Table 4 shows energy consumption that was stated in the EPC.

Table 4. Energy Consumption Data

School address	kWh/m^2
School 5	68.79
School 7	53.04
School 8	58.12
School 13	62.28
School 14	65.58
School 15	46.89
School 21	94.98
School 22	67.01
School 23	51.10
School 24	88.63
School 25	97.98

Figure 3 shows the comparison between the theoretical and actual HDD corrected heat energy consumption.

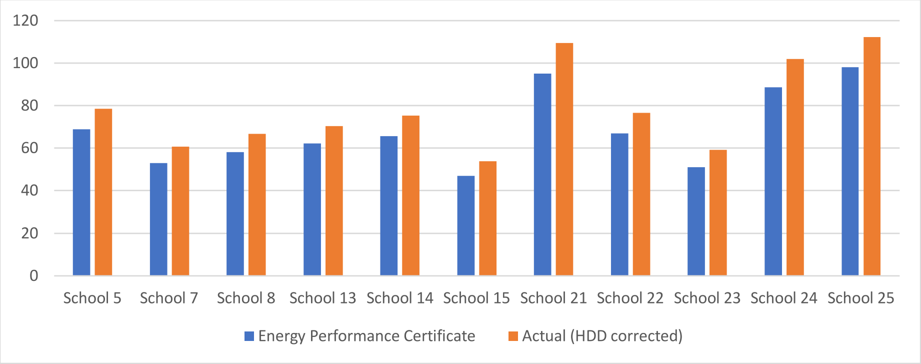

Fig. 3. Energy consumption comparison between EPC and actual heating consumption.

As it can be seen in the graph, the actual energy consumption differs from the one stated in the certificate in all cases, which means that schools consume on average 15 % more energy than it is stated in the EPC. The biggest difference occurred in the case of School 23, where actual consumption of energy for heating was 16 % higher than the theoretical consumption.

Overall, the data reveal that the actual energy consumption differs from the theoretical consumption, with all schools having higher actual consumption than the theoretical values, while possible reasons and solutions will be elaborated in further studies.

ACKNOWLEDGEMENTS

The study has been supported by the European Regional Development Fund project "Optimal Control of Indoor Air Quality and Thermal Comfort Based on Room Real-time 3D Motion Scanning Data", Grant Agreement No 1.1.1.1/21/A/010.

REFERENCES

1. NEMI. (2023). *Design Guidance for Education Facilities: Prioritization for Advanced Indoor Air Quality*. Available at https://www.nemionline.org/design-guidance-for-education-facilities/
2. Lazović, I. M., Turanjanin, V. M., Vučićević, B. S., Jovanović, M. P., & Jovanović, R. D. (2022). Influence of the Building Energy Efficiency on Indoor Air Temperature: The Case of a Typical School Classroom in Serbia. *Thermal Science*, *26* (4).
3. Tihana, J., Zajacs, A., Ivancovs, D., & Gaujena, B. (2022). Influence of Ventilation Operating Modes on Energy Efficiency. *Buildings*, *12* (5), 668.
4. Borodinecs, A., Nazarova, J., Zajacs, A., Malyshev, A., & Pronin, V. (2016). Specifics of Building Envelope Air Leakage Problems and Airtightness Measurements. *MATEC Web of Conferences*, *73* (1), 02020.
5. Shahid, Z. K., Saguna, S., & Ahlund, C. (2023). Forecasting Electricity and District Heating Consumption: A Case Study in Schools in Sweden. *IEEE Green Technologies Conference*, 169–175.
6. Zemitis, J., Borodinecs, A., Sidenko, N., & Zajacs, A. (2023). Simulation of IAQ and Thermal Comfort of a Classroom at Various Ventilation Strategies. *E3S Web of Conferences*. DOI: 10.1051/e3sconf/202339603005

7. Baranova, D., Sovetnikov, D., Semashkina, D., & Borodinecs, A. (2017). Correlation of Energy Efficiency and Thermal Comfort Depending on the Ventilation Strategy. *Procedia Engineering*, *205*, 503–510.
8. Tihana, J., Odineca, T., Borodinecs, A., Gendelis, S., & Jakovics, A. (2019). Optimal Properties of External Building Envelope for Minimization of Over Heating. *IOP Conference Series: Earth and Environmental Science*, *390*, 012046.
9. Krumins, A., Lebedeva, K., Tamane, A., & Millers, R. (2022). Possibilities of Balancing Buildings Energy Demand for Increasing Energy Efficiency in Latvia. *Environmental and Climate Technologies*, *26* (1), 98–114.
10. Wang, Y., Boulic, M., Phipps, R., Plagmann, M., Cunningham, C., & Guyot, G. (2023). Field Performance of a Solar Air Heater Used for Space heating and Ventilation – A Case Study in New Zealand Primary Schools. *Journal of Building Engineering*, 76, 106802.
11. woo Ham, S., Kim, D., Barham, T., & Ramseyer, K. (2023). The First Field Application of a Low-Cost MPC for Grid-Interactive K-12 schools: Lessons-Learned and Savings Assessment. *Energy and Buildings*, *296*, 113351.
12. Raatikainen, M., Skön, J. P., Leiviskä, K., & Kolehmainen, M. (2016). Intelligent Analysis of Energy Consumption in School Buildings. *Applied Energy*, *165* (6427), 416–429.
13. Ouf, M. M., & Issa, M. H. (2017). Energy Consumption Analysis of School Buildings in Manitoba, Canada. *International Journal of Sustainable Built Environment*, *34* (3), 665–677.
14. Kim, T. W., Kang, B. J., Kim, H., Park, C. W., & Hong, W. H. (2019). The Study on the Energy Consumption of Middle School Facilities in Daegu, Korea. *Energy Reports*, *5*, 993–1000.
15. Borodinecs, A., Prozuments, A., Zemitis, J., Zajecs, D., & Bebre, G. (2020). Hydrothermal Performance of the External Wooded Frame Wall Structure Reinforced with Ballistic Panels. *E3S Web of Conferences*, *172*, 07005.
16. Attia, S., Kurnitski, L., Kosiński, P., Borodiņecs, A., Belafi, Z. D., István, L., ... & Laurent, O. (2022). Overview and Future Challenges of Nearly Zero-Energy Building (nZEB) Design in Eastern Europe. *Energy and Buildings*, *276*, 112165.
17. Borodinecs, A., Prozuments, A., Zajacs, A., & Zemitis, J. (2019). Retrofitting of Fire Stations in Cold Climate Regions. *Magazine of Civil Engineering*, *90* (6), 85–92.
18. Borodinecs, A., Zemitis, J., Dobelis, M., Kalinka, M., Prozuments, A., & Šteinerte, K. (2017). Modular Retrofitting Solution of Buildings Based on 3D Scanning. *Procedia Engineering*, *205*, 160–166.
19. Zemitis, J., Borodinecs, A., Geikins, A., Kalamees, T., & Kuusk, K. (2016). Ventilation System Design in Three European Geo Cluster. *Energy Procedia*, *96*, 285–293.
20. Borodinecs, A., Zemitis, J., & Prozuments, A. (2012). Passive use of solar energy in double skin facades for reduction of cooling loads. In *World Renewable Energy Forum, WREF 2012, Including World Renewable Energy Congress XII and Colorado Renewable Energy Society (CRES) Annual Conference*, (pp. 4181–4186). 13–17 May 2012. Denver, Colorado, USA.
21. Bogdanovics, R., Borodinecs, A., Zemitis, J., & Zajacs, A. (2021). Using a Mobile Modular Energy Unit with PV Panels for Heating. *ASHRAE Journal*, *63* (4), 38–45.
22. Mohamed, S., Rodrigues, L., Omer, S., & Calautit, J. (2021). Overheating and indoor Air Quality in Primary Schools in the UK. *Energy and Buildings*, *250*, 111291.
23. Zemitis, J., & Bogdanovics, R. (2020). Heat Recovery Efficiency of Local Decentralized Ventilation Devices. *Magazine of Civil Engineering*, *94* (2), 120–128.
24. Bogdanovica, S., Zemitis, J., & Bogdanovics, R. (2020). The Effect of CO2 Concentration on Children's Well-Being during the Process of Learning. *Energies*, *13* (22), 6099.

25. Zemitis, J., Borodinecs, A., & Lauberts, A. (2018). Ventilation Impact on VOC Concentration Caused by Building Materials. *Magazine of Civil Engineering*, *84* (8), 130–139.
26. Sánchez, E. C., Bardón, C. C., & Viviana, O. P. (2023). Architectural and Environmental Strategies towards a Cost Optimal Deep Energy Retrofit for Mediterranean Public High Schools. *Energy Reports*, *9,* 6434–6448.
27. Kanama, N., Ondarts, M., Guyot, G., Outin, J., Golly, B., & Gonze, E. (2023). Effect of Energy Renovation on Indoor Air Quality and Thermal Environment in Winter of a Primary School in a Highly Polluted French Alpine Valley. *Journal of Building Engineering*, 106529.
28. Katić, D., Krstić, H., & Marenjak, S. (2021). Energy Performance of School Buildings by Construction Periods in Federation of Bosnia and Herzegovina. *Buildings*, *11* (2), 42.

LATVIAN JOURNAL OF PHYSICS
AND TECHNICAL SCIENCES
2024, N 2

DOI: 10.2478/lpts-2024-0015

TOWARDS HIGH-PRECISION QUADROTOR TRAJECTORY FOLLOWING CAPABILITIES: MODELLING, PARAMETER ESTIMATION, AND LQR CONTROL

A. Hanif, I. E. Putro*, A. Riyadl, O. Sudiana, Hakiki, H. Y. Irwanto

Research Organization for Aeronautics and Space,
National Research and Innovation Agency (BRIN),
Jakarta 10340, INDONESIA
*e-mail: idris.eko.putro@brin.go.id

Quadrotor unmanned aerial vehicles (UAVs) are small, agile four-rotor systems suitable for various applications, from surveillance to disaster support missions. Hence, achieving high-precision trajectory tracking is crucial for their successful deployment. This research focuses on modelling, parameter identification, and Linear Quadratic Regulator (LQR) control design for quadrotors, aiming to enhance their trajectory following capabilities. The quadrotor dynamics are a sixth degree-of-freedom (6DOF) equation of motion derived from Newton's second law, encompassing moment of inertia, centre of gravity, weight, and thrust of propeller parameters. Experimental measurements are conducted to accurately determine these parameters, ensuring a realistic representation of the quadrotor system. Subsequently, a linearized model is constructed to provide a suitable plant for control system development. The LQR control design is intended to improve the trajectory tracking performance. This control strategy is validated through simulation and practical experiments, demonstrating its effectiveness in achieving high-precision trajectory following capabilites. The proposed approach demonstrates that LQR control effectively guides the quadrotor to resemble a predefined trajectory, experiencing only 3 % overshoot observed during the initial phase of flight.

Keywords: *Control, LQR, modelling, parameter estimation, quadrotor, unmanned aerial vehicles (UAVs).*

1. INTRODUCTION

Autonomous unmanned aerial vehicles (UAVs), particularly quadrotors, have garnered significant interest due to their versatility and wide-ranging applications. Quadrotors are agile, four-rotor systems with VTOL capabilities, making them suitable for tasks such as surveillance, remote inspection, disaster management [1], and defense missions. Precise control is essential for quadrotors, given their waypoint and trajectory following missions [2].

Linear Quadratic Regulator (LQR) control methods have gained prominence in quadrotor control system design. Previous research [3] focused on LQR controller design for quadrotor helicopters and performance analysis. Another study [4] used a modified LQR approach to tune a PID controller's parameters based on experimental model parameter values. This modification introduced feedback considering the tracking error between the state vector and a reference state vector.

Furthermore, LQR has been employed to minimize steady-state errors and overshoot in waypoint following for flying wing UAVs [5]. Comparisons between LQR and other control methods, such as PID, PD, model predictive control (MPC), feedback linearization (FL), and sliding mode control (SMC), have been explored in various studies [6]–[10], often focusing on position and attitude control. These comparisons have provided insights into the effectiveness of different control strategies, including fuzzy logic and model reference adaptive PID controllers (MRAC) based on the MIT rule.

This paper explores quadrotor modelling and control design for precise trajectory following, employing LQR methodology. The model is developed to exhibit quadrotor dynamics, validated using flight test data and augmented with parameter estimation to enhance the precision of quadrotor UAVs in trajectory tracking.

2. PARAMETER ESTIMATION

The experimental measurement of quadrotor components must be conducted to estimate the right parameters and govern the dynamic equations.

2.1. Quadrotor Configuration

Quadrotor configuration can be depicted from Fig. 1 and Table 1.

Table 1. Quadrotor Specifications

Parameter	Value	Unit	Parameter	Value	Unit
Height	9.5	cm	Payload Capacity	0.15	kg
Length	38	m	Arm length	0.19	m
Mass	0.5	kg	COG position	0.05	m
Blade Span	10	cm	Number of blades	2	

Fig. 1. Quadrotor UAV.

The modelling of quadrotor follows necessary assumption, i.e., the quadrotor structure is supposed to be rigid and symmetrical, centre of gravity coincides with the body-fixed frame, and there is no mechanical and electrical characteristics difference between each brushless-motor, and also the quadrotor inflow is steady and uniform.

2.2. Moment of Inertia

To derive the moment and products of inertia for a small quadrotor, two methods are available: experimental measurement and theoretical calculation. While experiments yield real quadrotor values and are more accurate, they can be complex and costly for full-scale quadrotors. As a practical alternative, theoretical calculation is preferred. This approach involves modelling the quadrotor as cuboids and applying the parallel axis theorem [11]–[13], as illustrated in Fig. 2:

$$I_{xx} = I_{yy} = 2m(1+L)^2 + \frac{1}{12}M\left(c^2+b^2\right) + M\left(\frac{c}{2}\right)^2, \tag{1}$$

$$I_{zz} = 4m(1+L)^2 + \frac{1}{12}M\left(a^2+b^2\right), \tag{2}$$

$$I_{xy} = I_{xz} = I_{yz} = 0, \tag{3}$$

where M is the total mass of battery, quadrotor frame (at length l), and payload systems. Variable m denotes summation mass of quadrotor frame (from length l to L) and individual motor system. The dimensions of masses and lengths are presented in Table 2.

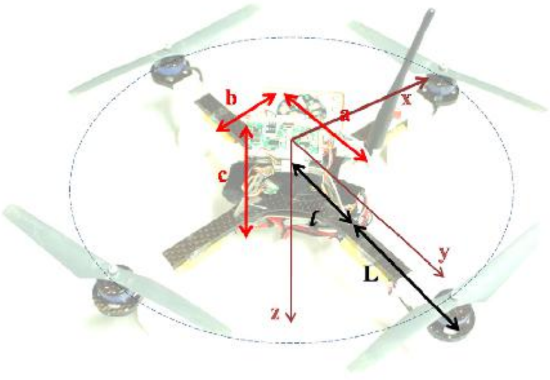

Fig. 2. Free body diagram simplified quadrotor model for inertia moment estimation.

Table 2. Masses and Lengths of Quadrotor

Parameter masses	Value	Unit	Parameter length	Value	Unit
Motor BLDC+Blade+Speed controller	4 x 0.047	kg	a	0.075	m
Battery system	0.1	kg	b	0.07	m
Payload (Sensor+Accuisition Board)	0.05	kg	c	0.07	m
Frame	1.70	kg	l	0.06	m
			L	0.019	m

By using the parallel axis theorem approach, we obtain the inertial moment values as shown in Table 3.

Table 3. Moment of Inertial Values Using Theoretical Approach

Parameter	Value	Unit
I_{xx}	4.82×10^{-3}	kg.m^2
I_{yy}	4.82×10^{-3}	kg.m^2
I_{zz}	8.77×10^{-3}	kg.m^2

2.3. Rotary Wing Motor

The quadrotor's electric propulsion system, consisting of a propeller, BLDC motor, and electronic speed controller, is essential for its control. Unlike manned aerial vehicles controlled by a joystick pilot, quadrotors receive angular propeller motion (RPM) in unmanned systems. Therefore, it is crucial to create a rotor model that accurately relates joystick inputs to motor dynamics.

To develop the motor model, experiments are conducted, collecting data from joystick command inputs and correlating them with propeller speed responses. These data enhance the accuracy of rotor simulations. Figure 3 outlines the experimental setup for the motor model development.

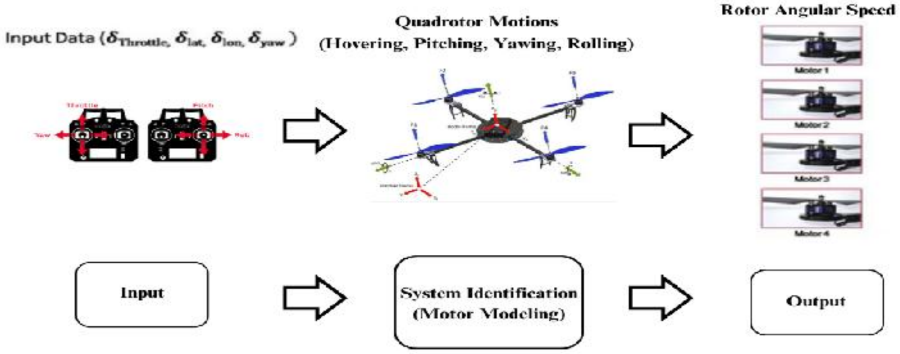

Fig. 3. Experimental process for motor identification.

Experiments are conducted to collect the data for roll and pitch dynamics; thus, rotor identification can be developed and validated consecutively. Figure 4 shows joystick input inserted to the BLDC motor for roll dynamics.

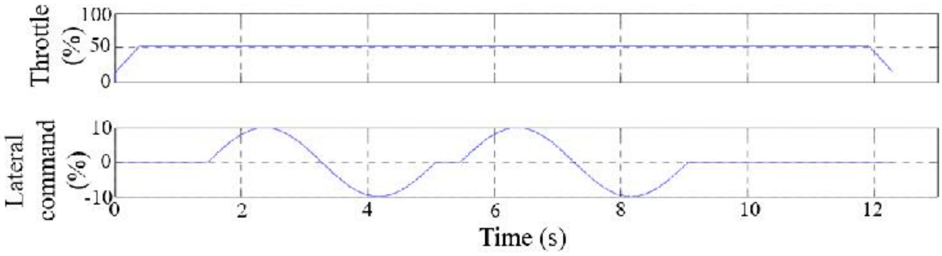

Fig. 4. Joystick inputs for roll dynamics.

The collective command $\delta_{throttle}$ to be set to a constant value and the lateral command δ_{lat} are sent to change the dynamic in rolling motion. Meanwhile, the other commands (δ_{long} and δ_{yaw}) are idle. The motor responses can then be acquired and compared to the validation results. Figures 5 and 6 depict the front side and right side of BLDC motor responses for roll dynamics.

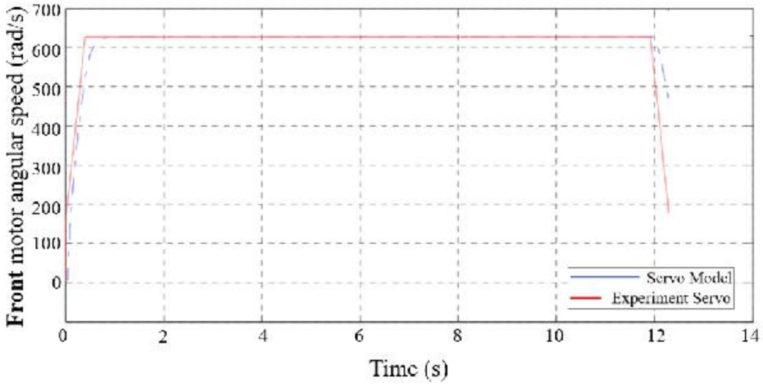

Fig. 5. Front side of the motor responses for roll dynamics.

Figures 5 and 6 show that both the front and right side of the motor responses of the quadrotor resemble the experiment data.

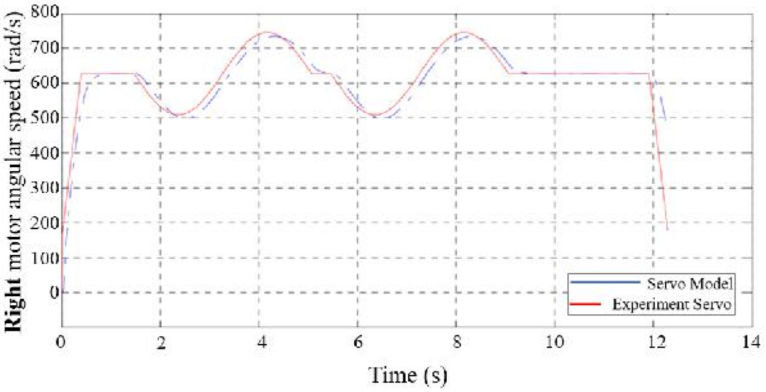

Fig. 6. Right side of the motor responses for roll dynamics.

The motor dynamics model closely approximates real motor behaviour with minimal error, accurately representing the rotor system. The left and right motors exhibit similar responses, though in opposite directions, due to the symmetrical configuration of all motors.

The same behaviour of the rotor system is obtained for pitch dynamic. Parameter identification of pitch dynamic for the rotor model requires $\delta_{throttle}$ to be set to a constant value, and the longitudinal command δ_{long} is sent to change of the motion. The other commands (δ_{lat} and δ_{yaw}) remain idle. In pitch dynamic, the right and left sides of BLDC responses are similar to front side motor in roll dynamics as shown in Fig. 5. They maintain their speeds together to produce enough thrust for pitch motion. Meanwhile, the dynamics of the front and rear sides of the motor angular speeds in pitch dynamics cause the change in pitch motion. Due to the symmetrical configuration, the front and rear motors exhibit similar responses as in Fig. 6, though in opposite directions between right and left sides. The rotor dynamic models resemble real motors in experiments with small errors. Hence, this rotor model is precise enough to represent the real rotor system in lateral and longitudinal modes.

3. QUADROTOR MODELLING

3.1. Quadrotor Dynamics

The nonlinear behaviour of quadrotor can be represented by 6DOF equation of motions. The equation of motion for a small quadrotor with respect to earth coordinate system is presented in this section.

For translational motion, the EOM is shown as Eq. (4) to Eq. (6):

$$\ddot{x}=\frac{1}{m}(\cos\psi\sin\theta\cos\varphi+\sin\psi\sin\varphi)\sum_{i=1}^{4}T_i+\frac{1}{m}\sum_{i=1}^{4}H_{x_i}\ ; \tag{4}$$

$$\ddot{y} = \frac{1}{m}(\sin\psi \sin\theta \cos\varphi + \cos\psi \sin\varphi)\sum_{i=1}^{4} T_i + \frac{1}{m}\sum_{i=1}^{4} H_{Y_i} \; ; \tag{5}$$

$$\ddot{z} = g - (\frac{1}{m}\cos\theta \cos\varphi \sum_{i=1}^{4} T_i) \; . \tag{6}$$

While rotational EoM is shown as Eq. (7) to Eq. (9):

$$\ddot{\varphi} = \dot{\theta}\frac{\dot{\psi}(I_{yy} - I_{zz})}{I_{xx}} + \frac{1}{I_{xx}}(T_4 - T_2) + (\sum_{i=1}^{4} H_{x_i})\frac{h}{I_{xx}} + \frac{R_{x_1} - R_{x_2} + R_{x_3} - R_{x_4}}{I_{xx}} \; ; \tag{7}$$

$$\ddot{\theta} = \dot{\varphi}\frac{\dot{\psi}(I_{zz} - I_{xx})}{I_{yy}} + \frac{1}{I_{yy}}(T_3 - T_1) + (\sum_{i=1}^{4} H_{y_i})\frac{h}{I_{yy}} + \frac{R_{y_1} - R_{y_2} + R_{y_3} - R_{y_4}}{I_{yy}} \; ; \tag{8}$$

$$\ddot{\psi} = \dot{\varphi}\frac{\dot{\theta}(I_{xx} - I_{yy})}{I_{zz}} + \frac{1}{I_{zz}}(\tau_1 - \tau_2 + \tau_3 - \tau_4) + (H_{x_4} - H_{x_2})\frac{1}{I_{zz}} + (H_{x_3} - H_{x_1})\frac{1}{I_{zz}} \; ; \tag{9}$$

where

$$T = C_T \rho A (\Omega R_{rad})^2 ; \tag{10}$$

$$H = C_H \rho A (\Omega R_{rad})^2 ; \tag{11}$$

$$Q = C_Q \rho A (\Omega R_{rad})^2 R_{rad} ; \tag{12}$$

$$Q = C_Q \rho A (\Omega R_{rad})^2 R_{rad} ; \tag{13}$$

$$\frac{C_T}{\sigma a} = \left(\frac{1}{4} + \frac{1}{4}\mu^2\right)\theta_0 - \left(1 + \mu^2\right)\frac{\theta_{tw}}{8} - \frac{1}{4}\lambda \; ; \tag{14}$$

$$\frac{C_H}{\sigma a} = \left(\frac{1}{4a}\mu \overline{C}_d\right) + \frac{1}{4}\lambda\mu\left(\theta_0 - \frac{\theta_{tw}}{2}\right); \tag{15}$$

$$\frac{C_Q}{\sigma a} = \frac{1}{8a}\left(1 + \mu^2\right)\overline{C}_d + \lambda\left(\frac{1}{6}\theta_0 - \frac{\theta_{tw}}{8} - \frac{1}{4}\lambda\right); \tag{16}$$

$$\frac{C_{R_m}}{\sigma a} = -\mu\left(\frac{1}{6}\theta_0 - \frac{\theta_{tw}}{8} - \frac{1}{8}\lambda\right). \tag{17}$$

Quadrotor is equipped with four fixed-rotors consisting of a brushless DC motor and propellers. This rotor system can be described using well-known equations [14]:

$$L\frac{di}{dt} = \delta - R_{mot} i - k_m \omega_m ; \tag{18}$$

$$J_m \frac{d\omega_m}{dt} = \tau_m - \tau_d \, . \tag{19}$$

Second order motor dynamics can be derived by assuming the used motor is small enough; thus. it has a very low inductance

$$J_m \frac{d\omega_m}{dt} = -\frac{k_m^2}{R_{mot}}\omega_m - \tau_d + \frac{k_m}{R_{mot}}\delta \, . \tag{20}$$

3.2. Linearized Model

Linearization is employed to obtain a linear model that approximates the quadrotor behaviour around trim condition, refers to a specific set of operating conditions. Linearization is performed using Taylor series expansion or Jacobian matrices to approximate the nonlinear equations as a set of linear equations that describe small perturbations from the chosen operating point. These linear models approximate how the quadrotor's state variables such as position, attitude, and velocity evolve in response to control inputs when the system is close to the trim condition.

A trimmed flight condition is defined as a state where the system is in balanced, steady-state with no rate of change and the resultant forces and moments are zero [15]:

$$f(x_e, u_e) = 0, \tag{21}$$

where x_e is an equilibrium value of state vector and u_e is a control vector in an equilibrium flight condition. The small perturbation is implemented to the trim condition; thus, the total state of each motion variable is equal to the sum of a steady state (equilibrium flight due to trimmed condition before) quantity and a perturbed state quantity [16]. The linearized model of a quadrotor can be written in the state space form as follows:

$$\dot{x} = Ax(t) + Bu(t), \tag{22}$$

where $x(t)$ is a state variable, $u(t)$ is control variable, A and B are system matrix and matrix input.

In terms of quadrotor dynamics, we can describe a state variable as follows:

$$x = \begin{bmatrix} u & v & w & p & q & r & \varphi & \theta & \psi \end{bmatrix}^T. \tag{23}$$

Control variable is described as follows:

$$u = \begin{bmatrix} \delta_{lat} & \delta_{long} & \delta_{yaw} & \delta_{throttle} \end{bmatrix}^T. \tag{24}$$

Matrix A and B are shown in the following form:

$$A = \begin{bmatrix} X_u & 0 & 0 & 0 & 0 & 0 & X_\varphi & X_\theta & X_\psi \\ 0 & Y_v & 0 & 0 & 0 & 0 & Y_\varphi & Y_\theta & Y_\psi \\ 0 & 0 & Z_w & 0 & 0 & 0 & Z_\varphi & Z_\theta & 0 \\ 0 & 0 & 0 & 0 & X_u & X_u & 0 & 0 & 0 \\ 0 & 0 & 0 & X_u & X_u & X_u & 0 & 0 & 0 \\ 0 & 0 & 0 & 0 & 0 & 0 & 0 & 0 & 0 \\ 0 & 0 & 0 & 1 & 0 & 0 & 0 & 0 & 0 \\ 0 & 0 & 0 & 0 & 1 & 0 & 0 & 0 & 0 \\ 0 & 0 & 0 & 0 & 0 & 1 & 0 & 0 & 0 \end{bmatrix}; \tag{25}$$

$$B=\begin{bmatrix} X_{lat} & X_{long} & X_{ped} & X_{col} \\ Y_{lat} & Y_{long} & Y_{ped} & Y_{col} \\ Z_{lat} & Z_{long} & Z_{ped} & Z_{col} \\ L_{lat} & L_{long} & L_{ped} & L_{col} \\ M_{lat} & M_{long} & M_{ped} & M_{col} \\ N_{lat} & N_{long} & N_{ped} & N_{col} \\ 0 & 0 & 0 & 0 \\ 0 & 0 & 0 & 0 \\ 0 & 0 & 0 & 0 \end{bmatrix}. \tag{26}$$

In this research, the quadrotor is linearized in two modes: hover flight and forward flight. The operating point used for linearization in hover condition is set for translation rates and angular rates close to zero, hence:

$$\begin{aligned} &u=0 \quad p=0 \quad \varphi=3.2x10^{-4}\,rad \\ &v=0 \quad q=0 \quad \theta=-1.5x10^{-5}\,rad \\ &w=0 \quad r=0 \quad \psi=1.67x10^{-8}\,rad \end{aligned}$$

While in forward flight, the operating point used is in cruise condition:

$$\begin{aligned} &u=2m/s \quad p=0 \quad \varphi=0.1rad \\ &v=0m/s \quad q=0 \quad \theta=0.1rad \\ &w=0m/s \quad r=0 \quad \psi=0.1rad \end{aligned}$$

A comparison of linear and nonlinear models is presented in Fig. 7.

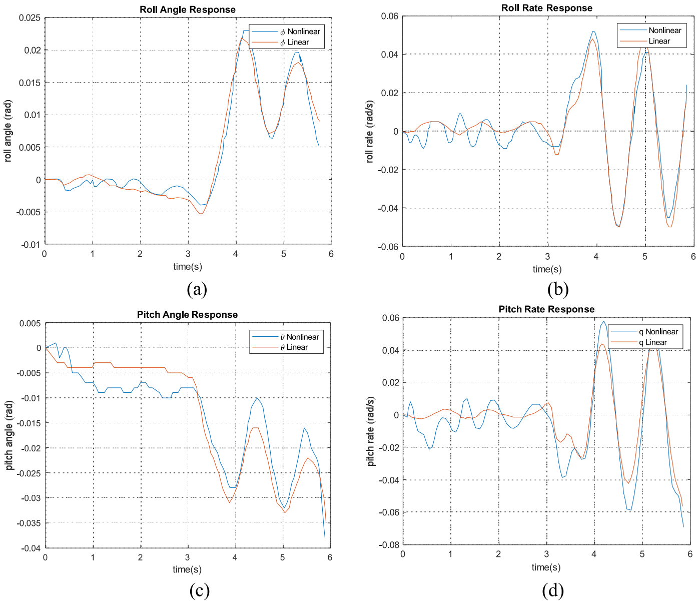

Fig. 7. Linear model validation: (a) roll angle, (b) roll rate, (c) pitch angle, (d) pitch rate.

The blue line on the graph denotes linear model responses, while the red line signifies nonlinear model responses. The linear model of the quadrotor resembles the nonlinear model; hence, the linear model can represent the nonlinear model to be utilized for optimal control system design.

3.3. Stability Augmentation System (SAS) Model

The quadrotor is inherently unstable due to nonlinear behaviour, cross-coupling in dynamics, and lightweight, so it is sensitive to external disturbances. The engineers then come up with particular controls to solve this unstable performance. They develop a control system to maintain the quadrotor vehicle having angular attitudes that tend to zero in hover condition. This control algorithm tries to keep rotational motion such as roll, pitch, and yaw in very small angles ($[\varphi \quad \theta \quad \psi]^T) \cong 0$ and its angular rate in zero rate of changes ($[\dot{\varphi} \quad \dot{\theta} \quad \dot{\psi}]^T) \cong 0$. Using this kind of control system, the quadrotor attitude will be stable, so the hovering flight can be obtained without paying excessive attention. Moreover, it is also robust for any small disturbances, such as wind inside the room and noise at the joystick command. The successful controller, which guarantees the small quadrotor can be flown in stable condition, is commonly known as Stability Augmentation System (SAS Controller).

The SAS controller used on this quadrotor vehicle follows the equation below:

$$\delta_{sas\_n}(t) = K_i * \int_0^t e_n(t) + K_p * e_n(t) + K_d * \frac{de_n(t)}{dt} + K_{pr} * e_{nr}(t)\,, \tag{27}$$

where $\delta_{sas\_n}(t)$ denotes an input for quadrotor motor (%), $e_n(t)$ is attitude errors (rad), $e_{nr}(t)$ is rate gyro errors (rad/s), K_{pr} is a proportional gain for rate attitude, K_p, K_i, and K_d are PID gain for integral, proportional, and differential, respectively.

Equation above is combined with the signal from joystick to give command input for quadrotor motions. Unless for throttle deflection, the other command inputs will be augmented by SAS as the following equation:

$$U_{(2,3,4)}(t) = \delta_{(lateral,long,heading)}(t) + \delta_{sas\_roll}(t)\,. \tag{28}$$

4. LQR DESIGN

4.1. Linear Quadratic Regulator (LQR)

Given the system dynamics equation,

$$\dot{x} = Ax + Bu\,. \tag{29}$$

The LQR method finds the optimal control decision by considering the system states and control input. The optimal controller is obtained by using the state feedback gain that minimizes a quadratic cost function.

$$J = \int_0^\infty \left(x^T Q x + u^T R u\right) dt\,. \tag{30}$$

The weighting matrix Q determines which states will be controlled more tightly than others. Weighting matrix R weights the control input movement that needs to be applied depending on how large the state deviates. Then, the optimal gain matrix K can be acquired using the following equation:

$$K = R^{-1} B^T P\,, \tag{31}$$

where P is obtained by solving algebraic Riccati equation (ARE) as:

$$A^T P + PA - PBR^{-1} - B^T P + Q = 0\,. \tag{32}$$

4.2. Trajectory Tracking Control

The LQR method can be utilised for designing trajectory following control, which is a tracking problem control. The principle of this tracking problem is to compare the output y(t) to a reference r(t) and expected to follow the given reference [17]. LQR will minimize the error between the output and the given reference.

$$y_{error}(t) = x_{error}(t) = x_{ref}(t) - x(t) \cdot \tag{33}$$

Conducting the time derivative of the equation yields

$$\dot{x}_{error}(t) = \dot{x}_{ref}(t) - \dot{x}(t)\,. \tag{34}$$

Setting the reference as a constant, the equation is simplified as:

$$\dot{x}_{error}(t) = -\dot{x}(t)\,. \tag{35}$$

Trajectory following controller design takes the following expression:

$$\dot{x}_{error}(t) = -\gamma\dot{x}(t); \gamma = 1,2,..,n\,, \tag{36}$$

where γ is an arbitrary positive constant representing the weight of the tracking performance in the cost function. The tracking error matrix $x_{error}(t)$ can be written in matrix form as:

$$x_{error}(t) = \begin{bmatrix} x_{error}(t) \\ y_{error}(t) \\ z_{error}(t) \end{bmatrix} = \begin{bmatrix} x_{ref}(t) - x(t) \\ y_{ref}(t) - y(t) \\ z_{ref}(t) - z(t) \end{bmatrix}, \tag{37}$$

where x, y, and z are the positions of the vehicle in the body axis frame. Derivation of the equation above can be written as:

$$\dot{x}_{error}(t) = \begin{bmatrix} \dot{x}_{error}(t) \\ \dot{y}_{error}(t) \\ \dot{z}_{error}(t) \end{bmatrix} = \begin{bmatrix} -\gamma\dot{x}(t) \\ -\gamma\dot{y}(t) \\ -\gamma\dot{z}(t) \end{bmatrix}. \tag{38}$$

Comparing with the state variable of state space system $\left(\begin{bmatrix}\dot{x} & \dot{y} & \dot{z}\end{bmatrix}^T\right) = \left(\begin{bmatrix}u & v & w\end{bmatrix}^T\right)$, the equation above can be formed to be

$$\dot{x}_{error}(t) = -\begin{bmatrix} \gamma u(t) \\ \gamma v(t) \\ \gamma w(t) \end{bmatrix}. \tag{39}$$

Due to error state vectors appearing, the state space system of the quadrotor model must be adjusted in order to accommodate the trajectory following mission as below:

$$\dot{x}_{adj}(t) = A_{adj}x_{adj}(t) + B_{adj}u_{adj}(t)\,, \tag{40}$$

where subscript "adj" denotes the adjusted variable that will be included in the existing state space model of the quadrotor. The adjusted matrices are defined as:

$$x_{adj} = \begin{bmatrix} x_{error} & y_{error} & z_{error} & x \end{bmatrix}^T, \tag{41}$$

$$A_{adj} = \begin{bmatrix} 0_{3x3} & -\gamma I_3 & 0_{3x(n-3)} \\ 0_{nx3} & A_{nxn} & \end{bmatrix}^T, \tag{42}$$

$$B_{adj} = \begin{bmatrix} 0_{3x4} \\ B_{nx4} \end{bmatrix}^T, \tag{43}$$

where n is the amount of state vector in the state space model. The quadratic cost function then can be written as the following expression:

$$J = \int_{t_0}^{t_f} \left(x^T{}_{adj}Qx_{adj} + u^T Ru\right)dt\,. \tag{44}$$

5. SIMULATION RESULT

This section explains model validation and control simulation results. The validation prioritizes comparisons between nonlinear models and flight test data, as well as SAS model. This validation assures that the linear model obtained from the nonlinear model is correct, allowing for precise control design.

5.1. Nonlinear Model Validation

The nonlinear model, as the full quadrotor model, is validated using experimental data generated from flight tests. The flight test has to record proper input and output data. The inputs are Joystick inputs, and the outputs are the behaviours of the quadrotor, which are measured by various sensors.

$$u_{\exp} = \left[\delta_{throttle} \quad \delta_{lat} \quad \delta_{long} \quad \delta_{heading}\right]^T, \tag{45}$$

$$Y_{\exp} = \left[\varphi \quad \dot{\varphi} \quad \theta \quad \dot{\theta} \quad \psi \quad \dot{\psi} \quad h\right]^T, \tag{46}$$

where the command inputs consist of the throttle input $\delta_{throttle}$, the lateral input δ_{lat}, the longitudinal input δ_{lon}, and the heading input $\delta_{heading}$. The variable outputs consist of angular motions $(\varphi \quad \theta \quad \psi)$ from IMU, angular rates $(\dot{\varphi} \quad \dot{\theta} \quad \dot{\psi})$ from rate-gyro, and altitude (h) from ultrasonic sensor.

Table 4. Flight Condition for Validation

Flight parameters	Trim condition	Flight parameters	Trim condition
Roll, φ (rad)	1.77E-4	X – position, *x* (m)	0
Roll rate, $\dot{\varphi}$ (rad/s)	0.004	X – velocity, *u* (m/s)	-0.015
Pitch, θ (rad)	0.001	Y – position, *y* (m)	0
Pitch rate, $\dot{\theta}$ (rad/s)	0.003	Y – velocity, *v* (m/s)	0
Yaw, ψ (rad)	3.398	Z – position, *z* (m)	0
Yaw rate, $\dot{\psi}$ (rad/s)	-0.003	Z – velocity, *w* (m/s)	0

Nonlinear model simulation and flight test simulation validation are conducted in the hover condition. Therefore, the inner-loop controller is set to keep the attitude dynamics of the quadrotor relatively stable and maintain the altitude. The flight conditions used for the quadrotor model simulation are shown in Table 4.

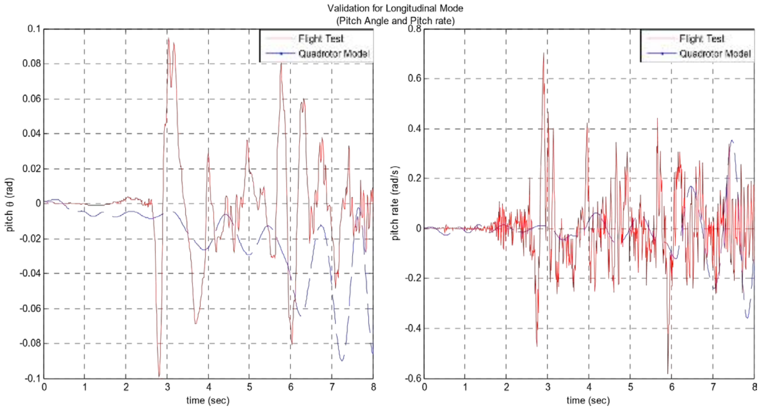

Fig. 8. Nonlinear model validation compared to flight test data for pitch dynamic.

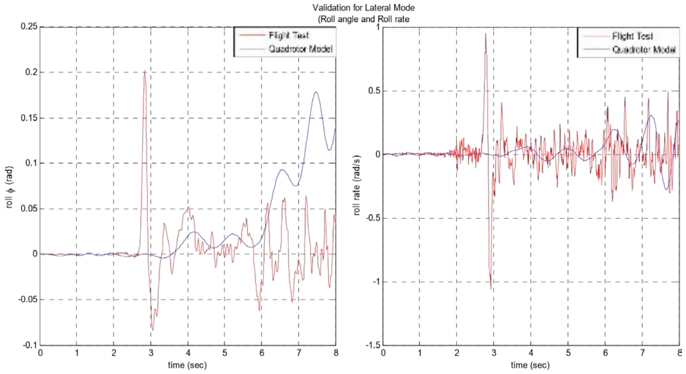

Fig. 9. Nonlinear model validation compared to flight test data for roll dynamic.

Quadrotor model validation compared to flight test responses are presented in Fig. 8 for longitudinal mode, and Fig. 9 for lateral mode.

Figures 8 to 9 depict that the responses of the quadrotor model resemble the flight test for pitch rate and roll rate. The responses of the model for pitch and roll are disparate from the flight test.

5.2. Trajectory Following Control Simulation

This control design uses LQR approach since this method is capable of reducing the quadrotor response settling time and overshoot percentage. The weighting matrices R and Q are set as uniform diagonal matrices with different values. Table 5 shows various LQR configurations.

Based on Table 5, configuration No. 3 is chosen because it is optimal for the quadrotor, considering the settling time and overshoot percentage. The result of the seventh configuration is presented in Fig. 10 for translational motion and Fig. 11 for rotational motion. Figures 10 and 11 depict that the LQR manages to converge the output states to 0. The trajectory following control is presented in Fig. 12 (a) for the circular path and Fig. 12 (b) for the spiral path.

Table 5. Various LQR Configurations

No.	Q	R	Settling time *ts* (second)		W overshoot
			Translation	Rotation	
1.	10	1	250	>1000	180 %
2.	1000	1	173	550	5 %
3.	100	0.01	150	7	2.5 %

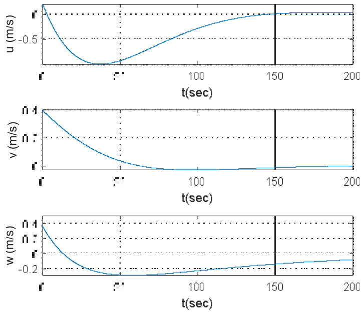

Fig. 10. Translational motion result of the seventh LQR configuration.

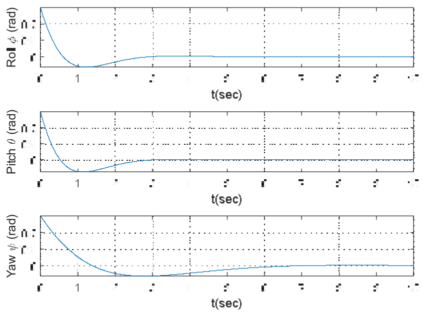

Fig. 11. Rotational motion result of the seventh LQR configuration.

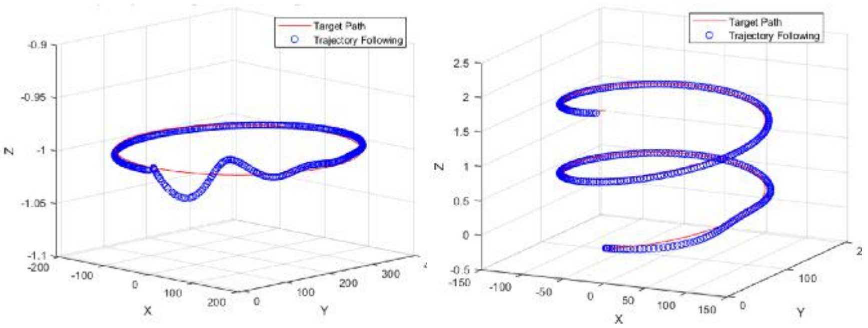

(a) (b)

Fig. 12. Trajectory following simulation of quadrotor (a) circular path and (b) spiral path.

Figure 12 shows that the model can resemble the trajectory command given. There is a deviation at the beginning of the simulation, but it is tolerable since it is only 3 %. Deviation occurs because the model has a long settling time to recover steady state. The velocity and position profiles are presented in Fig. 13 as the supporting details of whether the deviation happens.

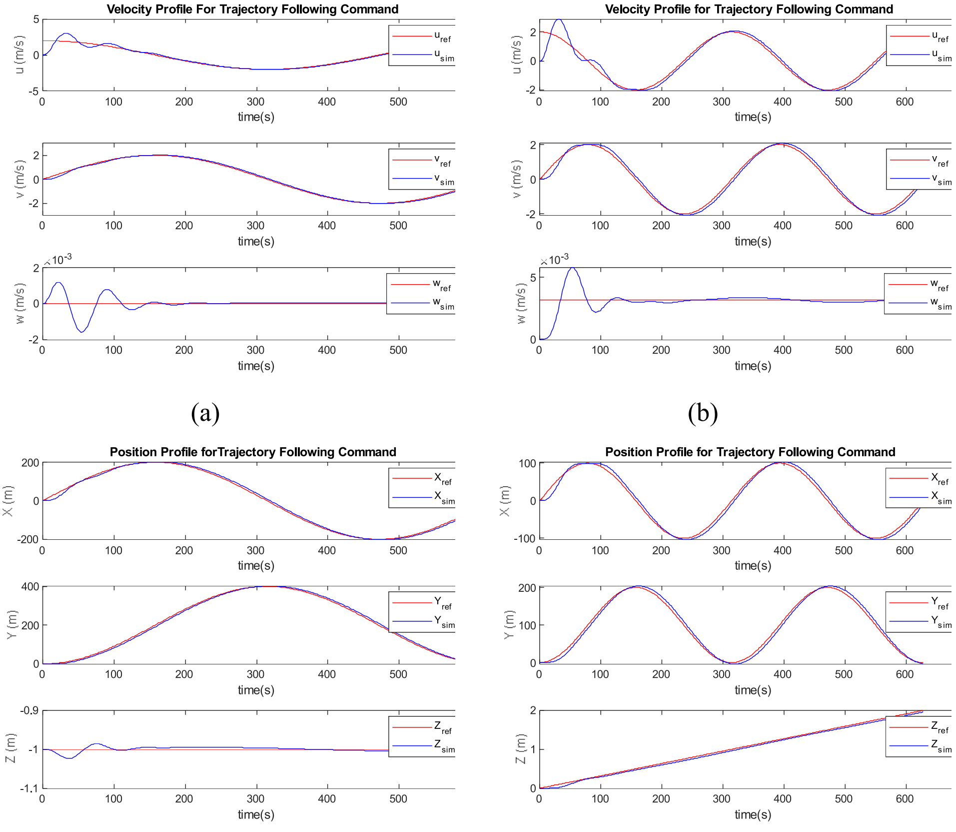

(a) (b)

(c) (d)

Fig. 13. Simulation result of trajectory following for (a) velocity profile of circular path; (b) velocity profile of spiral path; (c) position profile of circular path and (d) position profile of the spiral path.

Figure 13 depicts that deviation in simulation results occurs because the model requires time to resemble the command given. For instance, in Fig. 13 (a), the *u* and *w* responses oscillate for seconds before resembling the command given. For the spiral trajectory command in Fig. 13 (b) and (d), all of the velocity and position profiles differ from the command given at the beginning of the simulation. Control input response must be examined to ensure whether the configuration can be applied in the actual model. Figure 14 presents the control input response of the model.

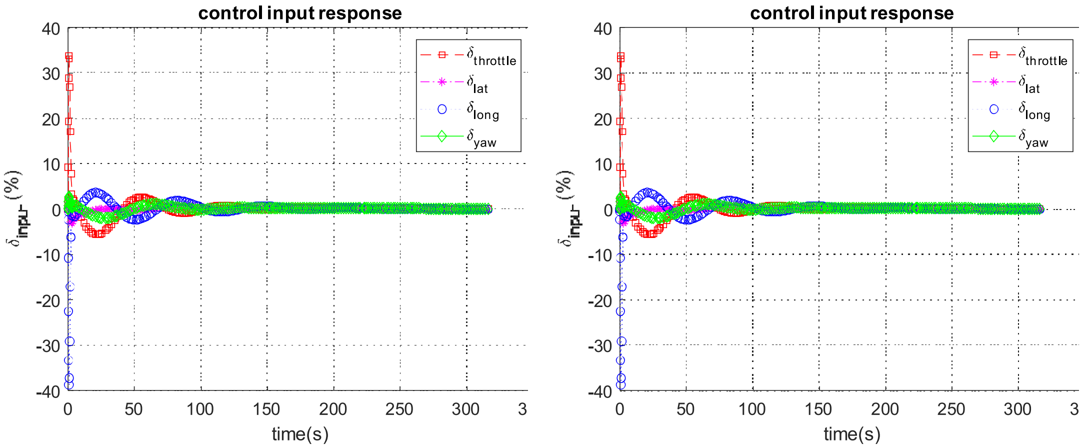

(a) (b)

Fig. 14. Control input response of (a) circular path and (b) spiral path.

Based on Fig. 14, the response of all control inputs for both circular and spiral trajectories are within the limit of input capability. Therefore, the control system can be used in the actual model.

6. CONCLUSION

The quadrotor model has been constructed and integrated with parameter estimation to improve model accuracy. The nonlinear quadrotor model has undergone validation through flight tests, demonstrating behaviour similar to that of a quadrotor. A linear quadrotor model has been derived through linearization, closely resembling the nonlinear model.

An LQR control system has been designed to complement the existing stability augmentation system for trajectory following. This LQR approach has enhanced quadrotor flight performance by closely aligning with trajectory references, with only minor deviations observed at the beginning of the simulation.

The simulation results indicate that precise trajectory following control can be achieved using reasonable command inputs. This outcome undergoes the research contribution to advancing quadrotor control and highlights its practical relevance for applications requiring precise autonomous navigation.

REFERENCES

1. Erdelj, M., Natalizio, E., Chowdhury, K. R., & Akyildiz, I. F. (2017). Help from the Sky: Leveraging UAVs for Disaster Management. *IEEE Pervasive Comput.*, *16* (1), 24–32. DOI: 10.1109/MPRV.2017.11.
2. Shaffer, R., Karpenko, M., & Gong, Q. (2016). Unscented guidance for waypoint navigation of a fixed-wing UAV. In Proc. Am. Control Conf., (pp. 473–478). July 2016. DOI: 10.1109/ACC.2016.7524959.
3. Okyere, E., Bousbaine, A., Poyi, G. T., Joseph, A. K., & Andrade, J. M. (2019). LQR Controller Design for Quad-Rotor Helicopters. *J. Eng.*, *2019* (17), 4003–4007. DOI: 10.1049/joe.2018.8126.
4. Guardeño, R., López, M. J., & Sánchez, V. M. (2019). MIMO PID Controller Tuning Method for Quadrotor Based on LQR/LQG Theory. *Robotics*, *8* (2), 15–21. DOI: 10.3390/ROBOTICS8020036.
5. Priyambodo, T. K., Dhewa, O. A., & Susanto, T. (2019). Model of Linear Quadratic Regulator (LQR) Control System in Waypoint Flight Mission of Flying Wing UAV. *J. Telecommun. Electron. Comput. Eng. (JTEC), 12* (4), 2289–8131. Available at https://jtec.utem.edu.my/jtec/article/view/5696.
6. Shehzad, M. F., Bilal, A., & Ahmad, H. (2019). Position attitude control of an aerial robot (quadrotor) with intelligent PID and state feedback LQR controller: A comparative approach. In *Proc. 2019 16th Int. Bhurban Conf. Appl. Sci. Technol. (IBCAST 2019),* (pp. 340–346). 8–12 January 2019, Islamabad, Pakistan. DOI: 10.1109/IBCAST.2019.8667170.
7. Saraf, P., Gupta, M., & Parimi, A. M. (2020). A comparative study between a classical and optimal controller for a quadrotor. In *2020 IEEE 17th India Counc. Int. Conf. (INDICON2020)*. 10–13 December 2020. New Delhi, India DOI: 10.1109/INDICON49873.2020.9342485.
8. Islam, M., & Okasha, M. (2019). A comparative study of PD, LQR and MPC on quadrotor using quaternion approach. In *2019 7th Int. Conf. Mechatronics Eng. (ICOM 2019)*, (pp. 1–6). 30–31 October 2019, Putrajaya, Malaysia. DOI: 10.1109/ICOM47790.2019.8952046.
9. Rinaldi, M., Primatesta, S., & Guglieri, G. (2023). A Comparative Study for Control of Quadrotor UAVs. *Appl. Sci.*, *13* (6). DOI: 10.3390/app13063464.
10. Shakeel, T., Arshad, J., Jaffery, M. H., Rehman, A. U., Eldin, E. T., Ghamry, N. A., & Shafiq, M. (2022). A Comparative Study of Control Methods for X3D Quadrotor Feedback Trajectory Control. *Appl. Sci.*, *12* (18), 9254. DOI: 10.3390/app12189254.
11. Abdulghany, A. R. (2017). Generalization of Parallel Axis Theorem for Rotational Inertia. *Am. J. Phys.*, *85* (10), 791–795. DOI: 10.1119/1.4994835.
12. Zhou, L., Pljonkin, A., & Singh, P. K. (2022). Modeling and PID Control of Quadrotor UAV Based on Machine Learning. *J. Intell. Syst.*, *31* (1), 1112–1122. DOI: 10.1515/jisys-2021-0213.
13. Kabir, A. M. (2019). Autonomous Control of a Quadrotor-Manipulator Application of Extended State Disturbance Observer. *arXiv*.
14. Bouabdallah, S., Murrieri, P., & Siegwart, R. (2005). Towards Autonomous Indoor Micro VTOL. *Auton. Robots*, *18* (2), 171–183. DOI: 10.1007/s10514-005-0724-z.
15. Padfield, G. D. (2007). *Helicopter Flight Dynamics: The Theory and Application of Flying Qualities and Simulation Modelling* (2nd ed.). Oxford: Blackwell Publishing Ltd.
16. Roskam, J. (2018). *Airplane Flight Dynamics and Automatic Flight Controls: Part I* (8th ed.). DARcorporation.
17. Budiyono, A., & Wibowo, S. S. (2007). Optimal Tracking Controller Design for a Small Scale Helicopter. *J. Bionic Eng.*, *4* (4), 271–280. DOI: 10.1016/S1672-6529(07)60041-9.